

# University of St Andrews



Full metadata for this thesis is available in  
St Andrews Research Repository  
at:

<http://research-repository.st-andrews.ac.uk/>

This thesis is protected by original copyright



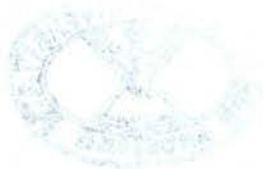
# Hydrothermal Synthesis of New Metal Fluorides

A thesis submitted for the degree of  
Doctor of Philosophy  
in the Faculty of Science of the University of St. Andrews  
by Nicholas Francis Stephens (BSc Hons)

May 2006

Supervisor : Dr Philip Lightfoot





Th F401

## Declaration

I, Nicholas F. Stephens, hereby certify that this thesis, which is approximately 30,000 words in length, has been written by me, that it is a record of work carried out by me and that it has not been submitted in any previous application for a higher degree.

Date 30/08/06 Signature of candidate

I was admitted as a research student in September 2002 and as a candidate for the degree of PhD in August 2003; the higher study for which this is a record was carried out in the University of St. Andrews between 2002 and 2006.

Date 30/08/06 Signature of candidate

I hereby certify that the candidate has fulfilled the conditions of the Resolution and Regulations appropriate for the degree of PhD in the University of St. Andrews and that the candidate is qualified to submit this thesis for the application for that degree.

Date 30/08/06 Signature of Supervisor

In submitting this thesis to the University of St. Andrews, I understand that I am giving permission for it to be made available for use in the accordance with the regulations of the University Library for the time being in force, subject to any copyright vested in the work not being affected thereby. I also understand that the title and abstract will be published, and that a copy of the work may be supplied to any *bona fide* library or research worker.

Date 30/08/06 Signature of candidate

## Acknowledgements

I would like to thank Dr. Philip Lightfoot for taking me into his research group. He has provided insight and advice, for which I am grateful. I would also like to thank Alan Snedden for his advice and patience. I would especially like to thank Alex Slawin for obtaining the single crystal X-ray data for which most of the results would not be possible without.

I would also like to thank John Groves for an entertaining time here at the University of St. Andrews, for lively discussions and especially for coffee and biscuits. Also, thanks go to Dave Aldous for whom this work is dedicated to, and has provided him something to do for the next three years. Thanks must also go to Richard Goff for proof-reading and darts practice.

And finally, I would like to thank my family and friends for their friendship, beer, food, lodgings and support. Oh, and anyone else I have forgotten.

Blimey, I sound like a proper author.

## Abstract

New organically templated fluorides have been produced by hydrothermal synthesis. The scandium fluoride materials, labelled Sc-*n*, fall into four structure types. Sc-1,  $[\text{H}_3\text{O}][\text{C}_6\text{N}_2\text{H}_{16}][\text{ScF}_6]\cdot\text{H}_2\text{O}$ , consists of isolated  $\text{ScF}_6$  octahedra with oxonium cations, water molecules and  $[\text{C}_2\text{N}_2\text{H}_{16}]^{2+}$  cations. Sc-2,  $[\text{C}_2\text{N}_2\text{H}_{10}][\text{ScF}_5]$  consists of eclipsed and staggered  $[\text{ScF}_5]^{2-}$  infinite chains and staggered stacks of  $[\text{C}_2\text{N}_2\text{H}_{10}]^{2+}$  cations along the same direction. This is related to Sc-4,  $[\text{C}_2\text{N}_2\text{H}_{10}]_{0.5}[\text{ScF}_4]$  only by the use of the same template. This is a hexagonal tungsten bronze related layer structure, and subtle changes in reaction conditions have produced two very different structures with the same structure directing agent. Sc-3,  $\text{NH}_4\text{ScF}_4$  is another layer structure, which resembles the Dion-Jacobson phases. Sc-5,  $(\text{NH}_4)_2\text{Sc}_3\text{F}_{11}$  is isostructural to  $\text{Rb}_2\text{In}_3\text{F}_{11}$ , both are related to  $\text{KSc}_2\text{F}_7$  by the addition of  $\text{ScF}_6$  octahedra. This is a 3-dimensional structure, which has  $\text{NH}_4^+$  cations located in “butterfly” channels.

The vanadium oxyfluoride materials labelled VOXF-*n* fall into five types. VOXF-1,  $[\text{C}_2\text{N}_2\text{H}_{10}][\text{VOF}_4(\text{H}_2\text{O})]$  and VOXF-2,  $[\text{C}_6\text{N}_2\text{H}_{16}][\text{VOF}_4(\text{H}_2\text{O})]$  are isolated octahedra types, which differ in the ordering of  $\text{VOF}_4(\text{H}_2\text{O})$  octahedra. The former is polar and shows a second harmonic generating (SHG) response. There are two chain types, VOXF-3,  $(\text{NH}_4)_2\text{VF}_5$  and VOXF-4,  $[\text{C}_2\text{N}_2\text{H}_{10}][\text{VF}_5]$ . The former is related to the other  $\text{A}_2\text{MF}_5$  types, while the latter is isostructural to Sc-2. VOXF-5,  $[\text{C}_6\text{N}_4\text{H}_{21}][\text{V}_2\text{O}_2\text{F}_7]\cdot 1.5\text{H}_2\text{O}$  and VOXF-6,  $[\text{C}_6\text{N}_2\text{H}_{14}][\text{V}_2\text{O}_2\text{F}_6(\text{H}_2\text{O})_2]$  consist of tetrameric and dimeric

units respectively. VOXF-7,  $[\text{C}_3\text{N}_2\text{H}_{12}][\text{V}_4\text{O}_{10}]$  consists of  $\text{VO}_4$  tetrahedra and  $\text{VO}_5$  trigonal bipyramids, which link to form sheets. It is closely related to the polymorph found by Riou and Férey, except the alignment of the  $\text{VO}_4$  tetrahedra is altered.

Some other materials, labelled misc-*n* do not fall into the above categories. Misc-1,  $[\text{C}_2\text{N}_2\text{H}_{10}]_{1.5}[\text{TiF}_6]\text{F}$  consists of isolated  $\text{TiF}_6$  octahedra with free  $\text{F}^-$  anions. Misc-2,  $[\text{C}_2\text{N}_2\text{H}_{10}]_2[\text{Nb}_2\text{O}_3\text{F}_8]$  consists of dimeric octahedral units. Misc-3,  $[\text{C}_2\text{N}_2\text{H}_{10}]_{0.5}[\text{Y}_2\text{F}_7]$  consists of  $\text{YF}_8$  square antiprisms and  $\text{Y}_9$  mono-capped square antiprisms, which link up to form a complex 3-dimensional structure. Misc-4,  $[\text{C}_3\text{N}_2\text{H}_{12}]_{0.5}[\text{Y}_3\text{F}_{10}]$  is an organically templated version of the  $\text{AM}_3\text{F}_{10}$  types, consisting of the "Super-Diamond" structure.

# Contents

<b>1</b>	<b>Introduction</b>	<b>1</b>
1.1	Overview . . . . .	1
1.2	Structural Properties . . . . .	2
1.2.1	Building units . . . . .	2
1.2.2	Out-of-Centre Distortion . . . . .	5
1.2.3	Non-centrosymmetry Classes . . . . .	6
1.2.4	Perovskite types . . . . .	11
1.2.5	Pyrochlores . . . . .	12
1.2.6	Hexagonal Tungsten Bronzes (HTB) . . . . .	13
1.2.7	Tetragonal Tungsten Bronzes (TTB) . . . . .	14
1.2.8	Isolated polyhedra . . . . .	15
1.2.9	Dimers . . . . .	20
1.2.10	Trimers . . . . .	23
1.2.11	Tetramers . . . . .	25
1.2.12	Chain types . . . . .	28
1.2.13	Sheets . . . . .	33

1.2.14	3-Dimensional Structures . . . . .	36
1.3	Physical Properties . . . . .	42
1.3.1	Properties of Fluorides . . . . .	42
1.3.2	Second Harmonic Generation (SHG) . . . . .	42
1.3.3	Piezo, Pyro and Ferroelectricity . . . . .	45
1.3.4	Magnetism . . . . .	46
1.3.5	Superexchange . . . . .	48
1.3.6	d <sup>1</sup> cations . . . . .	49
1.3.7	Magnetic Frustration . . . . .	50
1.4	Aims . . . . .	51
<b>2</b>	<b>Techniques</b> . . . . .	<b>59</b>
2.1	The Hydrothermal Method . . . . .	59
2.2	X-ray Diffraction . . . . .	60
2.2.1	The Single Crystal Method . . . . .	63
2.2.2	Direct Methods . . . . .	64
2.2.3	Patterson Method . . . . .	65
2.2.4	Refinement . . . . .	66
2.2.5	The Powder Method . . . . .	68
2.2.6	Rietveld Refinement . . . . .	68
2.3	Bond Valence Sum Calculation . . . . .	69
2.4	Thermogravimetric Analysis (TGA) . . . . .	70
2.5	CHN Microanalysis . . . . .	71
2.6	Optical Microscopy . . . . .	71
2.7	Electron Microscopy . . . . .	73

2.8	MAS NMR Spectroscopy . . . . .	74
2.9	SHG Measurements . . . . .	75
<b>3</b>	<b>Experimental</b>	<b>78</b>
3.1	Synthesis . . . . .	78
<b>4</b>	<b>Scandium Fluorides</b>	<b>80</b>
4.1	Introduction . . . . .	80
4.2	$[\text{H}_3\text{O}][\text{C}_6\text{N}_2\text{H}_{16}][\text{ScF}_6]\cdot\text{H}_2\text{O}$ (Sc-1) . . . . .	84
4.2.1	Experimental . . . . .	84
4.2.2	Discussion . . . . .	85
4.3	$[\text{C}_2\text{N}_2\text{H}_{10}][\text{ScF}_5]$ (Sc-2) . . . . .	91
4.3.1	Experimental . . . . .	91
4.3.2	Discussion . . . . .	92
4.4	$\text{NH}_4\text{ScF}_4$ (Sc-3) . . . . .	99
4.4.1	Experimental . . . . .	99
4.4.2	Discussion . . . . .	100
4.5	$[\text{C}_2\text{N}_2\text{H}_{10}]_{0.5}[\text{ScF}_4]$ (Sc-4) . . . . .	105
4.5.1	Experimental . . . . .	105
4.5.2	Discussion . . . . .	106
4.6	$(\text{NH}_4)_2\text{Sc}_3\text{F}_{11}$ (Sc-5) . . . . .	115
4.6.1	Experimental . . . . .	115
4.6.2	Discussion . . . . .	116
4.7	Concluding Remarks . . . . .	122
<b>5</b>	<b>Vanadium Oxyfluorides</b>	<b>127</b>

5.1	Introduction . . . . .	127
5.2	$[\text{C}_2\text{N}_2\text{H}_{10}][\text{VOF}_4(\text{H}_2\text{O})]$ (VOXF-1) . . . . .	130
5.2.1	Experimental . . . . .	130
5.2.2	Characterisation . . . . .	130
5.2.3	Discussion . . . . .	131
5.2.4	Thermogravimetric Analysis . . . . .	134
5.3	$[\text{C}_6\text{N}_2\text{H}_{16}][\text{VOF}_4(\text{H}_2\text{O})]$ (VOXF-2) . . . . .	136
5.3.1	Experimental . . . . .	136
5.3.2	Discussion . . . . .	137
5.4	$(\text{NH}_4)_2\text{VF}_5$ (VOXF-3) . . . . .	141
5.4.1	Experimental . . . . .	141
5.4.2	Discussion . . . . .	142
5.5	$[\text{C}_2\text{N}_2\text{H}_{10}][\text{VF}_5]$ (VOXF-4) . . . . .	146
5.5.1	Experimental . . . . .	146
5.5.2	Characterisation . . . . .	146
5.5.3	Discussion . . . . .	147
5.6	$[\text{C}_6\text{N}_4\text{H}_{21}]_2[\text{V}_4\text{O}_4\text{F}_{14}]\cdot 3\text{H}_2\text{O}$ (VOXF-5) . . . . .	152
5.6.1	Experimental . . . . .	152
5.6.2	Discussion . . . . .	153
5.7	$[\text{C}_6\text{N}_2\text{H}_{14}][\text{V}_2\text{O}_2\text{F}_6(\text{H}_2\text{O})_2]$ (VOXF-6) . . . . .	158
5.7.1	Experimental . . . . .	158
5.7.2	Discussion . . . . .	159
5.8	$[\text{C}_3\text{N}_2\text{H}_{12}][\text{V}_4\text{O}_{10}]$ (VOXF-7) . . . . .	164
5.8.1	Experimental . . . . .	164
5.8.2	Discussion . . . . .	165

5.9	Concluding Remarks . . . . .	169
<b>6</b>	<b>Miscellaneous</b>	<b>173</b>
6.1	$[\text{C}_2\text{N}_2\text{H}_{10}]_{1.5}[\text{TiF}_6]\text{F}$ (misc-1) . . . . .	175
6.1.1	Experimental . . . . .	175
6.1.2	Synthesis . . . . .	175
6.1.3	Discussion . . . . .	176
6.2	$[\text{C}_2\text{N}_2\text{H}_{10}]_2[\text{Nb}_2\text{O}_3\text{F}_8]$ (misc-2) . . . . .	184
6.2.1	Experimental . . . . .	184
6.2.2	Discussion . . . . .	185
6.3	$[\text{C}_2\text{N}_2\text{H}_{10}]_{0.5}[\text{Y}_2\text{F}_7]$ (misc-3) . . . . .	194
6.3.1	Experimental . . . . .	194
6.3.2	Discussion . . . . .	195
6.4	$[\text{C}_3\text{N}_2\text{H}_{12}]_{0.5}[\text{Y}_3\text{F}_{10}]$ (misc-4) . . . . .	202
6.4.1	Experimental . . . . .	202
6.4.2	Discussion . . . . .	204
6.5	Concluding Remarks . . . . .	209
	<b>Appendices</b>	<b>214</b>
	<b>A Publications</b>	<b>214</b>
	<b>B Bond Distances and Angles</b>	<b>216</b>

# Chapter 1

## Introduction

### 1.1 Overview

The work described in this thesis is concerned with transition metal fluorides, their synthesis, characterisation and discussion of their structures and any other properties, which ascribes them original and interesting features. What follows is a discussion of the concept of pre-nucleation units and secondary building units, known structure types and the interrelation between symmetry and physical properties.

## 1.2 Structural Properties

### 1.2.1 Building units

The building unit is defined as the minimum assembly of atoms, ions, or molecules, which by condensation of the group with others (identical or different), gives rise to the final solid, whatever the symmetry and/or dimensionality - Gerard Férey[1].

The concept of the building unit can be applied in two ways; the material can be examined after the synthesis to achieve a greater understanding of the structure, so that new structures may be postulated; or the formation of the building units in solution during synthesis can be studied. This can be achieved by controlling the experimental conditions that lead up to precipitation by use of the appropriate template and pH. The building unit can be as simple as a single primary building unit (e.g. an  $\text{SiO}_4$  tetrahedron), right up to different units connected by their corners, edges or faces to form a secondary building unit (SBU), which condense to form complex structures.

Two examples of SBUs that are synthesised to produce new materials are the double 4-ring [2] and the double 6-ring [3]. These are made up of two rings of corner sharing  $\text{MO}_4$  tetrahedra, shown in Figure 1.1.

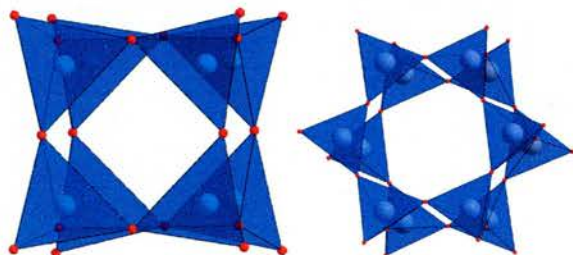


*Figure 1.1: The  $D_4R$  and  $D_6R$  SBU.*

Wang, Liu and Jacobson [4] mention several vanadium silicates. Some have SBUs in the shape of the letter “Y”. Figure 1.2 shows the unit, which consist of corner-sharing  $\text{SiO}_4$  tetrahedra.

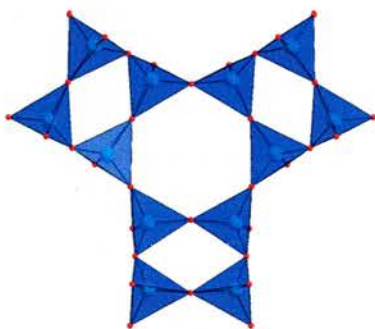


*Figure 1.2: The Y unit.*

Other units can be visualised, depending upon the complexity and topology of the structure. Experimental conditions and the choice of charge balancing cations (metals, ammonia,  $\text{OH}^-$ , amines or complexes) can affect this. It is

known for free  $F^-$  anions to take part in the templating of certain structures. The double-rings mentioned, for example and the effect  $F^-$  anions have on the ordering of template molecules[5].

The concept of building units and pre nucleation units can lead to a more rational method of producing novel structures. Isolated polyhedra, dimeric units, chains, sheets or open frameworks are some of the structure types that can be visualised.

Even experimental conditions such as pH can direct subtle changes in the reaction, leading up to precipitation. Aquo, hydrogenfluoride and hydrogenphosphate complexes of  $Ti^{4+}$  cations [6] are deprotonated when the pH is increased. The complexes are more liable to condense, and condensation may occur *via* the OH or F ligands to produce Ti-O-Ti, or Ti-F-Ti linkages. These two processes compete with each other. It is important to perform the chemical reactions in a systematic manner. This is discussed further in Chapter 2.

### 1.2.2 Out-of-Centre Distortion

Compounds of the early transition metals in the  $d^0$  electronic configuration possess distorted  $MX_6$  octahedra [7]. This is known as the second order Jahn-Teller effect. Figure 1.3 shows an example of this distortion in  $BaTiO_3$ .

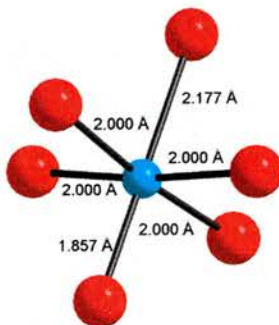


Figure 1.3: The  $TiO_6$  octahedron in  $BaTiO_3$ .

This manifestation of the second order Jahn-Teller effect is at its greatest with a small and highly charged metal cation. The disparity in M-X bond lengths is a result of this distortion, and can cause a dipole moment to develop. The hydrogen bonding network can re-enforce distortion from the electronic effects [8]. The M-X bond can be lengthened by the hydrogen bonding interaction between the ligand and the donor (N-H or O-H). For the metal atom to maintain its proper valence, the other M-X bonds shorten to compensate. Izumi and co-workers [9] have varied the degree of distortion of the  $NbOF_5^{2-}$  anion using copper and cadmium complexes. Interactions between the complex and the ligands can increase the length of the Nb=O bond, and the Nb-F bond, resulting in a reduction in distortion of the bonding around the  $NbOF_5$  octahedron.

### 1.2.3 Non-centrosymmetry Classes

The relationship between crystal class and related physical properties is shown in Figure 1.4. The crystal class in question has to be, by definition, non-centrosymmetric. The physical properties highlighted cannot occur in centrosymmetric solids. The non-centrosymmetric compounds can be separated into two main classes, polar and non-polar [10]. This distinction can be divided into sub-classes, A to G.

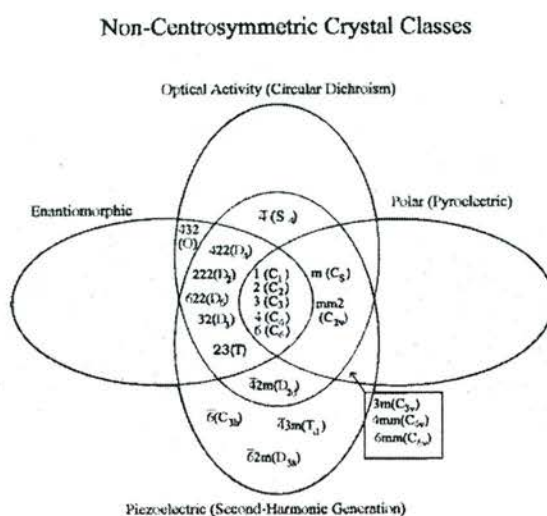


Figure 1.4: The non-centrosymmetric crystal classes.

Classes A to C refer to the polar compounds. Non-polar compounds in classes D to G exhibit all properties to one extent or another, except for pyroelectricity. In a polar structure, the motifs at each end of the polar axis are not related to each other by a symmetry operation. It is not possible for a non-polar compound to be pyroelectric, because of this symmetry condition. This is discussed further in this chapter.

Table 1.1 shows how the crystal classes are grouped into classes, depending upon their properties.

*Table 1.1: The interrelation between class, crystal class and properties.*

Class	Crystal classes	Enantiomorphic	Optically active	Piezoelectric	Pyroelectric
A	1, 2, 3, 4, 6	✓	✓	✓	✓
B	m, mm2	✗	✓	✓	✓
C	3m, 4m, 6mm	✗	✗	✓	✓
D	422, 222, 622, 32, 23	✓	✓	✓	✗
E	$\bar{4}2m, \bar{4}$	✗	✓	✓	✗
F	$\bar{6}, \bar{4}3m, \bar{6}2m$	✗	✗	✓	✗
G	432	✓	✓	✗	✗

It is interesting to note that certain properties depend on others. For example, enantiomorphic materials have to be optically active. Similarly, pyroelectric materials have to be piezoelectric. However, an optically active material does not have to be enantiomorphic and a piezoelectric material does not have to be pyroelectric.

An example of a pyroelectric is  $\text{KTiOPO}_4$  (KTP) [11]. KTP crystallises in the polar space group  $\text{Pna}2_1$ . It consists  $\text{TiO}_6$  octahedra, which link into polar chains along the b-axis. Potassium cations occupy the spaces created by 6-membered rings. The symmetry condition for pyroelectric materials is polarity.

An analogue [12]  $\text{AScFAsO}_4$  ( $A = \text{Rb}^+, \text{Cs}^+$ ) showed a reduced second harmonic generating (SHG) response. This was partly due to the negligible distortion of the  $\text{ScO}_4\text{F}_2$  octahedron and a larger energy gap between the

HOMO and the LUMO. This results in very little second order Jahn-Teller distortion effect and a Pnan pseudo-symmetry. KTP is shown in Figure 1.5.

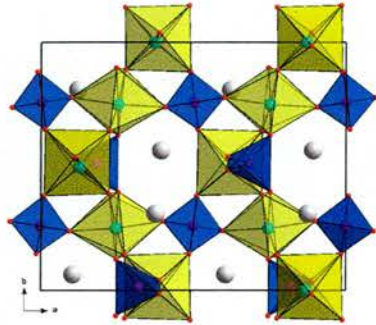


Figure 1.5:  $\text{KTiOPO}_4$  along the  $c$ -axis.

An example of a piezoelectric material is  $\text{BaTiSi}_3\text{O}_9$  [13]. This is a class F material and is shown in Figure 1.6, and consists of a hexagonal array of  $\text{SiO}_4$  tetrahedra and  $\text{TiO}_6$  octahedra. Rings of three  $\text{SiO}_4$  tetrahedra are connected to three  $\text{TiO}_6$  octahedra *via* Si-O-Ti links. This material crystallises in the space group  $\text{P}\bar{6}\text{c}2$ .

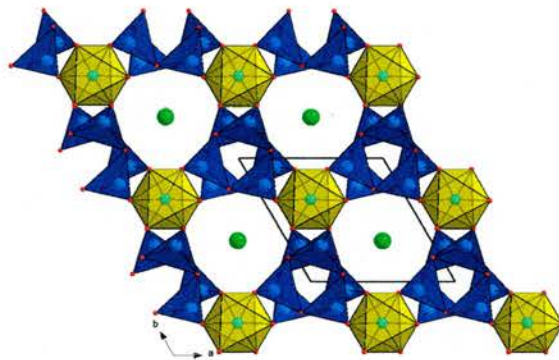


Figure 1.6:  $\text{BaTiSi}_3\text{O}_9$  along the  $c$ -axis.

One of the examples of class G material is  $\text{Li}_{0.75}\text{Fe}_{4.75}\text{Zn}_{0.5}\text{O}_8$  [14], shown in Figure 1.7. This crystallises in the space group P432, and is a condensed phase of corner- and edge-sharing  $\text{FeO}_4$  tetrahedra. The  $\text{FeO}_6$  octahedra, and the Fe, Zn and Li sites are all disordered.

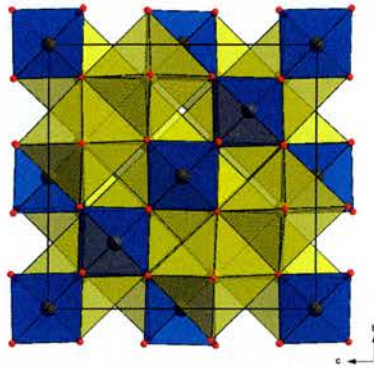


Figure 1.7:  $\text{Li}_{0.75}\text{Fe}_{4.75}\text{Zn}_{0.5}\text{O}_8$  along the  $a$ -axis.

A class A material such as  $\text{As}_2\text{V}_4\text{O}_{13}$  [15] can show all of the properties relating to non-centrosymmetry. This is shown in Figure 1.8 and crystallises in the space group P1. It consists of a network of corner- and edge-sharing  $\text{VO}_6$  octahedra and  $\text{AsO}_4$  tetrahedra.

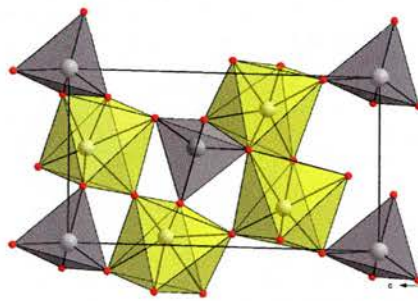
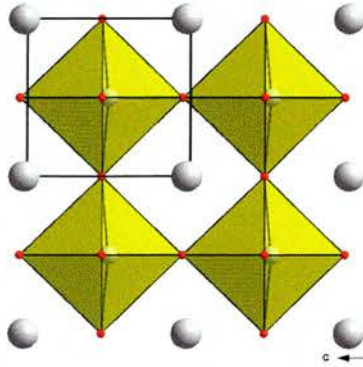


Figure 1.8:  $\text{As}_2\text{V}_4\text{O}_{13}$  along the  $a$ -axis, with  $\text{VO}_6$  octahedra in yellow and  $\text{AsO}_4$  tetrahedra in grey.

A class C material can be pyroelectric and piezoelectric only.  $\text{KNbO}_3$  [16] in Figure 1.9 crystallises in  $P4mm$ . The cubic perovskite parent structure is reduced in symmetry to the tetragonal perovskite by the displacement of the Nb atoms from the centre of the  $\text{NbO}_6$  octahedra.



*Figure 1.9:  $\text{KNbO}_3$  along the  $a$ -axis.*

This is a good example of how a subtle change in structure can take the symmetry away from centric.

### 1.2.4 Perovskite types

The perovskite [17] structure shown in Figure 1.10 consists of  $BX_6$  octahedra corner-sharing with six others in a cubic arrangement, for example  $CaTiO_3$ . The A cations lie in the 12 co-ordinate holes.

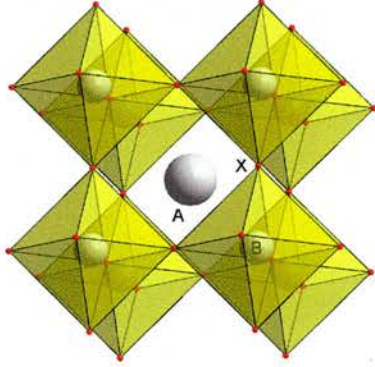


*Figure 1.10: The perovskite structure.*

The perovskite structure is well studied, and the  $BX_6$  octahedra can tilt away or towards the A cation, depending upon its size [18]. The tilting of the  $BX_6$  octahedra can cause the structure to adopt a lower symmetry, producing the hexagonal  $BaTi_{0.5}Mn_{0.5}O_3$  [19], rhombohedral  $LiNbO_3$  [20], tetragonal  $PbZr_xTi_{1-x}O_3$  (where  $x < 0.52$ ) and the monoclinic  $PbZr_{0.52}Ti_{0.48}O_3$  [21] and the orthorhombic  $LaMnO_3$  [22].

When the A cation is removed, the structure is the cubic  $ReO_3$  structure type, which many inorganic fluorides possess.  $ScF_3$  and  $NbF_3$  are the more common examples.

## 1.2.5 Pyrochlores

The pyrochlores, of which  $\text{NaCaNb}_2\text{O}_6\text{F}$  is an example, crystallise in the space group  $\text{Fd}\bar{3}\text{m}$  and conform to the general formula  $\text{M}_2\text{X}_6$ . A recent example,  $[\text{V}_2\text{F}_6]\cdot\text{H}_2\text{O}$  [23] is shown in Figure 1.11. It consists of corner sharing  $\text{MX}_6$  octahedra, which produce 3- and 6-membered ring cavities. The water molecules in this specific example depart the structure from 50 to 250 °C, and it oxidises to  $\text{V}_2\text{O}_5$  up to 400 °C. It is antiferromagnetic below 5 K.

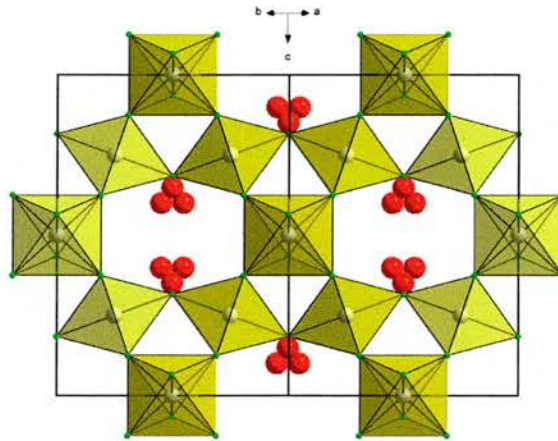


Figure 1.11: The pyrochlore structure of  $[\text{V}_2\text{F}_6]\cdot\text{H}_2\text{O}$

### 1.2.6 Hexagonal Tungsten Bronzes (HTB)

The HTBs are so called because  $\text{WO}_3$  exhibits a metallic sheen, much like bronze. They consist of  $\text{MX}_6$  octahedra, which corner-share with each other to produce 3- and 6-membered ring channels, which run along the  $c$ -axis.

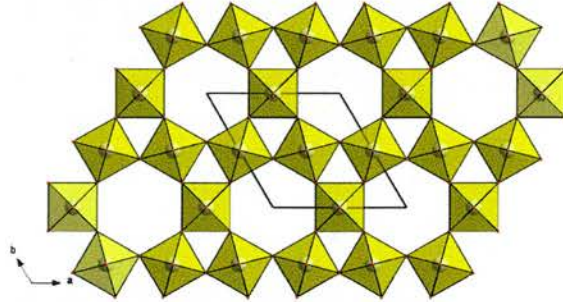


Figure 1.12: The HTB structure of  $\text{WO}_3$  shown along the  $c$ -axis.

Many HTBs have been studied by Francke *et al* [24]. Formation by the competitive condensation of  $\text{M-OH}$  and  $\text{M-F}$  bonds depends upon the size of the cation, the nature of the metal precursor and the method of synthesis. FTIR showed that water molecules were trapped inside the 6-membered ring channels. HTBs with narrow channels are often more thermally stable than their wide channel counterparts, because of the tight bonding of the water molecules to the F atoms. This bonding serves to stabilise the structure. With wider channels, the water molecules will be more loosely bound to the channels and so the structure will be less thermally stable.

### 1.2.7 Tetragonal Tungsten Bronzes (TTB)

In the TTBs, each  $\text{MX}_6$  octahedron is co-ordinated by six others *via* their corners to produce 3-, 4- and 5-membered ring channels. A distorted modification [25] of the a typical  $\text{AMX}_3$  TTB is shown in Figure 1.13.

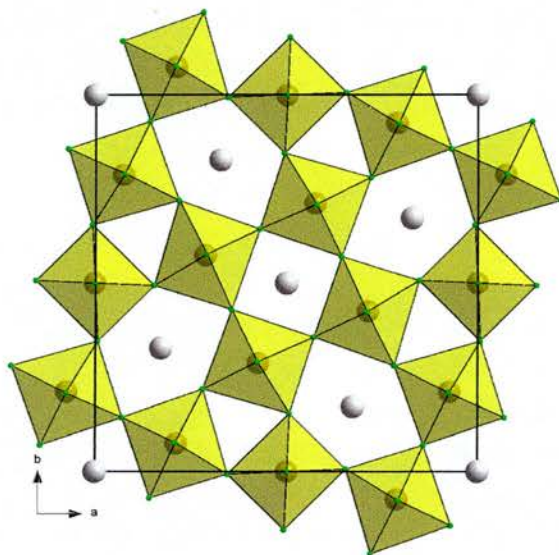


Figure 1.13: The TTB  $\text{K}_{5.25}\text{Fe}_{10}\text{F}_{30}$ .

The TTB's are related to the  $\text{ReO}_3$  structure type by the rotation of a central block of four  $\text{MX}_6$  octahedra about  $90^\circ$ . A more typical example of a TTB will have regular 3-, 4- and 5-membered ring channels.

## 1.2.8 Isolated polyhedra

Single isolated  $[\text{VOF}_4(\text{H}_2\text{O})]^{2-}$  units have been prepared by Mattes and Foerster [26]. This type of unit is shown in Figure 1.14.

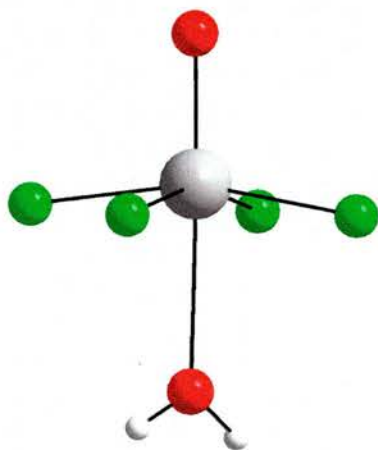


Figure 1.14: The  $\text{VOF}_4(\text{H}_2\text{O})$  unit.

The caesium salt of these anions have two structurally similar versions where the crystals of one are green and the crystals of the other are blue. The change of colour may be due to the V-OH<sub>2</sub> bond distance. The green variety has a V-OH<sub>2</sub> bond distance of 2.3 Å, while the blue variety has a shorter V-OH<sub>2</sub> bond distance of 2.27 Å. The  $[\text{VOF}_4(\text{H}_2\text{O})]^{2-}$  units hydrogen bond *via* the terminal O ligand and the water molecule of the next unit to form infinite chains along the b-axis. The terminal F atoms also hydrogen bond to the water molecule with a longer bond distance in the blue version than in the green version. The chains align anti-parallel to each other in a centrosymmetric cell. With the chains aligned parallel to each other in a non-centrosymmetric cell, it could exhibit non-linear properties due to the intrinsic polarity of the unit.

Another type of isolated polyhedron in the form of  $[\text{C}_5\text{H}_5\text{NH}][\text{CrO}_3\text{F}]$  [27], consists of a single  $\text{CrO}_3\text{F}$  tetrahedron alongside a pyridinium cation. This is shown in Figure 1.15. There was no appreciable hydrogen bonding between the two so the template molecule was disordered in all six positions. It crystallised in the polar space group  $\text{Cmc}2_1$ . The pyridinium cations and  $\text{CrO}_3\text{F}$  anions alternate along the  $b$ -axis. The F atom of the  $\text{CrO}_3\text{F}$  motif point towards each pyridinium cation in one direction along the  $c$ -axis. Because of the polarity of the structure, it is expected to show non-linear properties (e.g. second harmonic generation and pyroelectricity). However, Chaudhuri and co-workers did not measure this property.

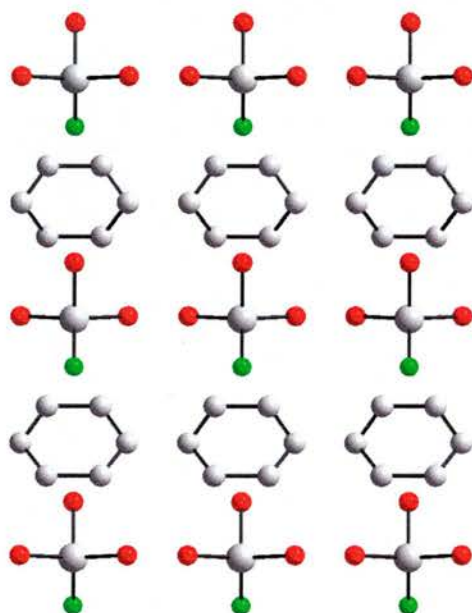


Figure 1.15:  $[\text{C}_5\text{H}_5\text{NH}][\text{CrO}_3\text{F}]$  along the  $b$ -axis.

Brink and co-workers [28] prepared  $\text{Na}_3\text{MoO}_3\text{F}_3$ , which is shown in Figure 1.16.

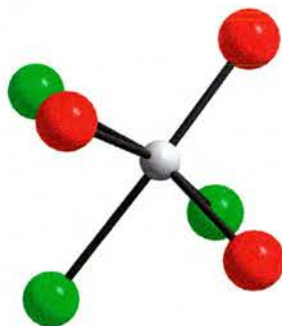


Figure 1.16: The  $[\text{MoO}_3\text{F}_3]^{6-}$  octahedron.

Neutron and electron diffraction showed the atoms to be perfectly ordered. This is related to a larger family of compounds, the cubic elapsolites. However, the diffraction study showed that the structure had a lower symmetry. This was because the Mo atom was displaced away from the centre of the  $\text{Mo}_3\text{F}_3$  octahedron and towards the oxygen atoms.

Isolated units can bind together electrostatically to form parallel chains, in the form of  $(\text{Ag}_3\text{MoO}_3\text{F}_3)(\text{Ag}_3\text{MoO}_4)\text{Cl}$  [29]. It consists of two chains made up of  $\text{MoO}_4$  tetrahedra and  $\text{MoO}_3\text{F}_3$  octahedra, which are bound by  $\text{Ag}^+$  cations.

Each  $\text{MoO}_3\text{F}_3$  octahedron has a *fac* configuration with three O atoms on one face, and three F atoms on the other face. The Mo atom is displaced from the centre of the octahedron towards all three O atoms. It was noted that the ideal point group for the *fac* configuration was  $3m$ , which assisted in the determination of the space group.

The chains align parallel to each other and the dipole moments align in the polar direction. The structure is shown in Figure 1.17. SHG measurements indicated an efficiency ten times that of  $\alpha$ -quartz, but because there may have been a racemic mixture, the response was much lower than that of an enantiomerically pure sample.

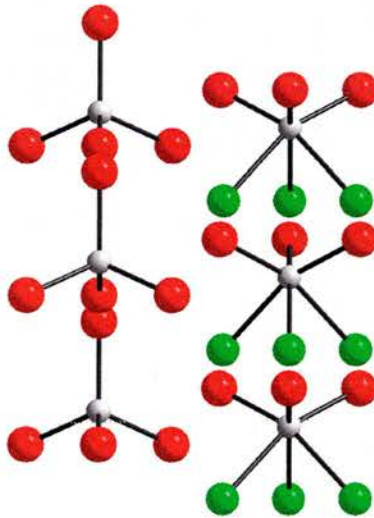


Figure 1.17: The two chains present in  $(\text{Ag}_3\text{MoO}_3\text{F}_3)(\text{Ag}_3\text{MoO}_4)\text{Cl}$  [29].

$\text{Ba}_5\text{Nb}_3\text{O}_3\text{F}_{18}(\text{HF}_2)[30]$  consists of  $\text{NbOF}_6$  pentagonal bipyramids and is shown in Figure 1.18. The location of the O atom is disordered. The red atoms in the diagram show the sites which could either be an O or a F atom.

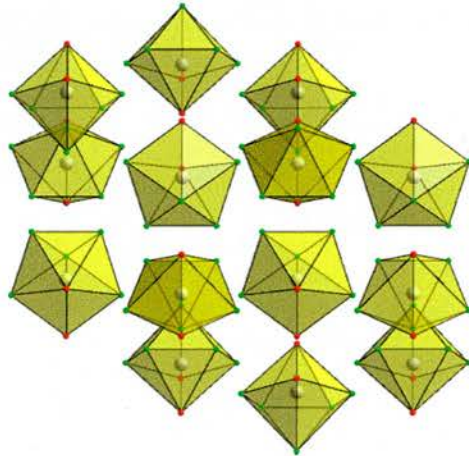


Figure 1.18:  $\text{Ba}_5\text{Nb}_3\text{O}_3\text{F}_{18}(\text{HF}_2)$ .

$(\text{NH}_4)_3\text{VO}_2\text{F}_4[31]$  is shown in Figure 1.19. It consists of  $\text{VO}_2\text{F}_4$  octahedra and disordered  $\text{V}(\text{O},\text{F})_6$  octahedra. Again, with most of the structures discussed, there is a displacement of the vanadium atom from the centre of the octahedra towards the O atoms.

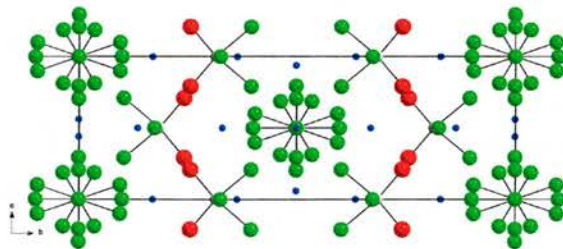


Figure 1.19:  $(\text{NH}_4)_3\text{VO}_2\text{F}_4$  showing the disorder of  $\text{V}(\text{O},\text{F})_6$  octahedra.

### 1.2.9 Dimers

Three oxofluorovanadium anions have been synthesised by Mattes *et al* [32]. The  $[\text{V}_2\text{O}_4\text{F}_5]^{3-}$ ,  $[\text{V}_2\text{O}_2\text{F}_7]^{3-}$  and  $[\text{V}_2\text{F}_9]^{3-}$  anions have V atoms in the +5, +4 and +3 oxidation states respectively. These consist of face sharing double octahedra with some F atoms forming the face and some O atoms on terminal positions. The  $[\text{V}_2\text{O}_4\text{F}_5]^{3-}$  dimer can be seen in Figure 1.20 and the other two dimers conform to the same structural layout, except for the assignment of F and O atoms.

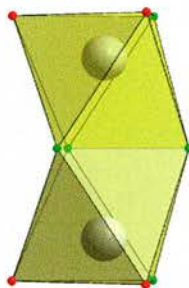


Figure 1.20: A view of the  $[\text{V}_2\text{O}_4\text{F}_5]^{3-}$  dimer.

The tetramethylammonium salt of the  $[\text{V}_2\text{O}_4\text{F}_5]^{3-}$  anion shows equal  $\text{V}=\text{O}$  and terminal  $\text{V}-\text{F}$  bond lengths. The terminal  $\text{V}-\text{O}$  and  $\text{V}-\text{F}$  bond lengths are shorter than usual. This may be due to the partial occupancy of the O atoms. What was also noticed was the bridging  $\text{V}-\text{F}$  bond distances were approximately 2 Å long, because of the *trans* effect with the O atoms. The other dimers showed bond distances of 1.6 Å for the  $\text{V}=\text{O}$  double bond, 1.9 Å for the terminal  $\text{V}-\text{F}$  bonds and 2 Å for the bridging  $\text{V}-\text{F}$  bonds. The *trans* effect causes the elongation of one  $\text{M}-\text{X}$  bond located *trans* to a much shorter

M=O bond.

Vibrational spectroscopy showed an absence of bands in the 560-880  $\text{cm}^{-1}$  region. This proves that there are no V-O-V linkages in any of the dimers. The O atoms were found to be exclusively bonded in terminal positions. The structure consists of the dimers interspersed by  $\text{NMe}_4^+$  cations.  $\text{Cs}_3\text{Fe}_2\text{F}_9$  [33], consists of dimers of  $\text{FeF}_6$  octahedra sharing a face with another, and is related to the  $[\text{V}_2\text{O}_4\text{F}_5]^{3-}$  dimer. It was not expected that the terminal O ligands would be protonated as no evidence for this was found in the vibrational spectroscopy.

$[\text{C}_8\text{H}_{20}\text{N}]_2[\text{Ta}_2\text{OF}_{10}]$  [34] consists of  $[\text{Ta}_2\text{OF}_{10}]^{2-}$  dimeric units, which are formed by two  $\text{TaOF}_5$  octahedra linked together by the O atom. This is shown in Figure 1.21.

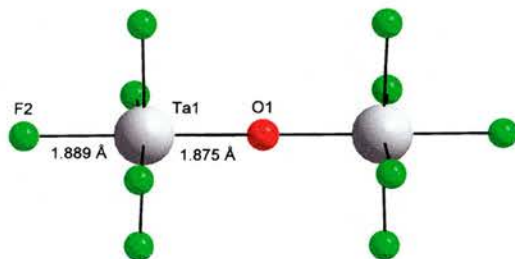


Figure 1.21: The dimeric unit in  $[\text{C}_8\text{H}_{20}\text{N}]_2[\text{Ta}_2\text{OF}_{10}]$ .

Each Ta atom is slightly displaced from the centre of each TaOF<sub>5</sub> octahedron towards the linking O atom. The displacement here is much less than V and Nb types.

[C<sub>4</sub>H<sub>12</sub>N<sub>2</sub>]<sub>2</sub>[Ti<sub>2</sub>OF<sub>10</sub>].2H<sub>2</sub>O [35] consists of TiOF<sub>5</sub> octahedra, which link together *via* the O atom to form dimeric units. The Ti atoms are displaced from the centre of their TiOF<sub>5</sub> octahedra towards the linking O atom, and this is shown in Figure 1.22.

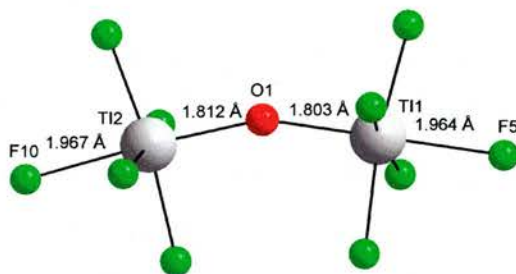


Figure 1.22: The dimeric unit in [C<sub>4</sub>H<sub>12</sub>N<sub>2</sub>]<sub>2</sub>[Ti<sub>2</sub>OF<sub>10</sub>].2H<sub>2</sub>O.

This is very similar to the [Ta<sub>2</sub>OF<sub>10</sub>]<sup>2-</sup> anion, except that the M-O-M linkage is bent.



Figure 1.24 shows another structure with  $\text{VOF}_5$  octahedra.

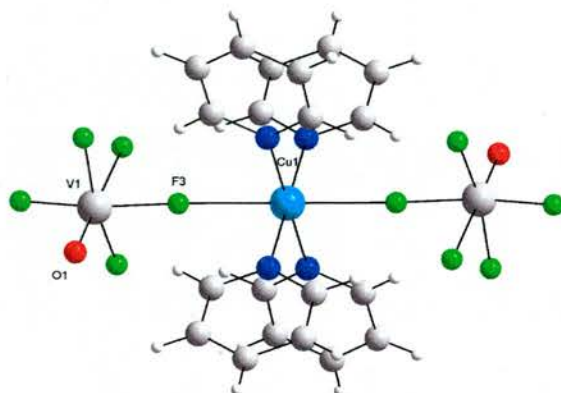


Figure 1.24: The trimeric unit in  $[\text{C}_5\text{NH}_6]_2\text{Cu}(\text{C}_5\text{NH}_5)_4(\text{VOF}_5)_2$ .

The  $(\text{C}_5\text{NH}_6)_4\text{CuF}_2$  octahedron was Jahn-Teller distorted in a similar fashion to the previous examples, but the V atom was displaced from the centre of the  $\text{VOF}_5$  octahedron towards the O atom perpendicular to the Cu-F-V bond. All of these units show the second order Jahn-Teller effects, required for polarity within the octahedra, but these compounds are centrosymmetric and cannot show any non-linear optical effects.

### 1.2.11 Tetramers

Another tetrameric structure is  $\text{Ba}_4\text{Nb}_2\text{O}_3\text{F}_{12}$ [38]. It consists of isolated  $\text{NbOF}_6$  pentagonal bipyramids and tetrameric units.  $\text{NbO}_2\text{F}_4$  octahedra and  $\text{NbO}_3\text{F}_3$  octahedra are connected together *via* O atoms to form the tetrameric units. This is shown in Figure 1.25.

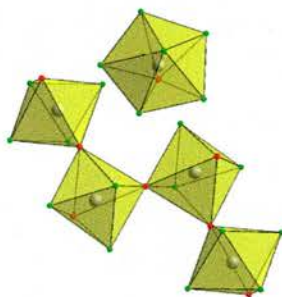


Figure 1.25: The tetrameric unit and isolated pentagonal bipyramid in  $\text{Ba}_4\text{Nb}_2\text{O}_3\text{F}_{12}$ .

Tetrameric groups of  $[\text{V}_4\text{O}_8\text{F}_{16}]^{12-}$  have been synthesised by Crosnier-Lopez, Duroy and Fourquet [39]. This is shown in Figure 1.26.

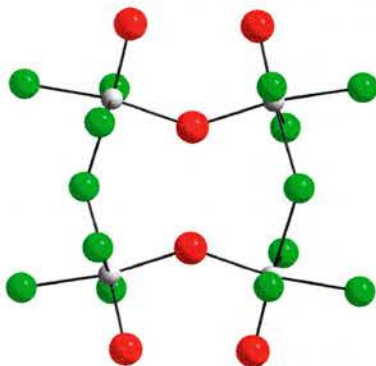


Figure 1.26: The tetrameric unit in  $\text{Ba}_3\text{V}_2\text{O}_4\text{F}_8$ .

$\text{Ba}_3\text{V}_2\text{O}_4\text{F}_8$  is also related to  $\text{Ba}_3\text{Al}_2\text{F}_{12}$  and some other  $\text{A}_3\text{M}_2\text{X}_{12}$  types discussed. It consists of four corner shared  $\text{V}(\text{O},\text{F})_6$  octahedra, forming a four-membered ring cluster. Each octahedron is connected to the next by F or O bridges. It exhibits typical bond distances for the bonds  $\text{V}=\text{O}$  of 1.684 Å, and V-F bonds of 2.079 Å in length due to the *trans* effect. Two unconnected corners of each octahedron are occupied by an F and an O atom. It is unclear however, which occupies the third unconnected corner.

G. Decap and co-workers produced  $\text{Pb}_3\text{Fe}_2\text{F}_{12}$ , which consists of  $[\text{Fe}_4\text{F}_{20}]^{8-}$  tetramers and lead cations, with isolated  $\text{F}^-$  anions. Each tetramer is composed of four  $\text{FeF}_6$  octahedra, connected together *via* corners, producing a 4-membered ring [40], shown in Figure 1.27. Out of centre distortions are present, which aligns the  $\text{Fe}^{3+}$  cations away from the centre of the 4-membered ring.

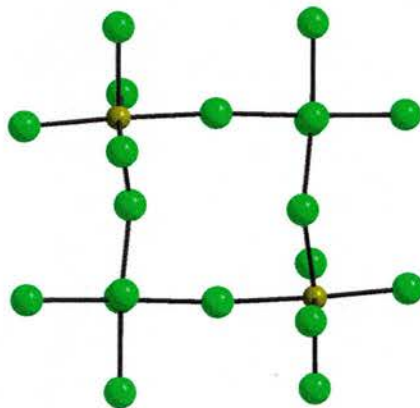


Figure 1.27: The tetramer found in  $\text{Pb}_3\text{Fe}_2\text{F}_{12}$ .

Figure 1.28 shows  $[C_4H_{40}N_{16}][Zr_4O_4F_{24}][41]$ , which is made up of  $ZrF_7$  and  $ZrF_8$  polyhedra. Each are joined together to form the tetrameric unit *via* two bridging F atoms. The Zr atoms are displaced away from the bridging F atoms towards the terminal F atoms.

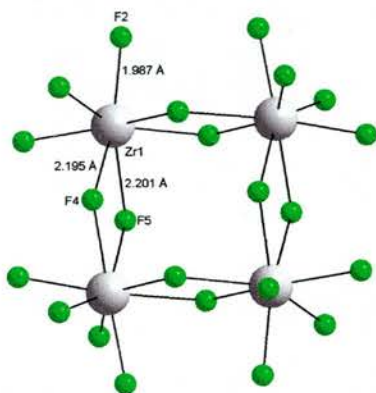


Figure 1.28: The tetrameric unit in  $[C_4H_{40}N_{16}][Zr_4O_4F_{24}]$ .

$[C_{10}H_{10}Cl_2W]_2[W_4F_{18}][42]$  consists of  $WF_6$  octahedra, which share their corners to form the tetrameric unit shown in Figure 1.29.

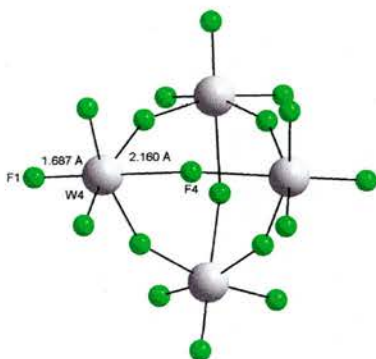


Figure 1.29: The tetrameric unit in  $[C_{10}H_{10}Cl_2W]_2[W_4F_{18}]$ .

Each W atom is displaced from the centre of each  $\text{WF}_6$  octahedron towards the terminal F atoms.

### 1.2.12 Chain types

Individual polyhedra can join together in to a single chain by either sharing corners, edges or faces.  $\beta\text{-(NH}_4)_2\text{FeF}_5$  [43] is one example of corner sharing  $\text{FeF}_6$  octahedra, which forms infinite chains along the b-axis. This is shown in Figure 1.30. This was produced by dehydration of  $\beta\text{-(NH}_4)_2\text{FeF}_5\cdot\text{H}_2\text{O}$ . The  $\text{FeF}_6$  octahedra connect via a F-Fe-F bond angle of  $148^\circ$ , with octahedra sharing *trans* corners. The same structure type can also be seen in  $(\text{NH}_4)_2\text{TiF}_5$  [44].

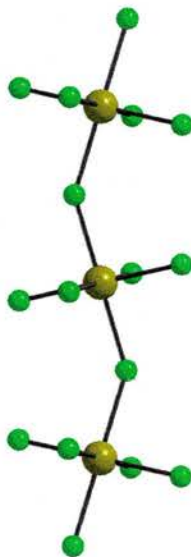


Figure 1.30: A view of the chain found in  $(\text{NH}_4)_2\text{FeF}_5$

Another example of corner-sharing is  $(\text{NH}_4)_2\text{VOF}_4$  [45]. The chains shown in Figure 1.31 lie along the *c*-axis, with a V-F-V bond angle of  $172^\circ$ . The V-O bond distance is consistent with a double bond of  $1.6 \text{ \AA}$ . V-F bond distances vary from  $1.9 \text{ \AA}$  to  $2.2 \text{ \AA}$ , with the longest between the bridging F atoms, due to the *trans* effect from the O atom. The ammonium cations bind the chains together by the F and O atoms by a N-X distance of  $2.8 \text{ \AA}$  to  $3 \text{ \AA}$ . It crystallises in the space group  $\text{Pna}2_1$ , which is polar and capable of optical activity and SHG.

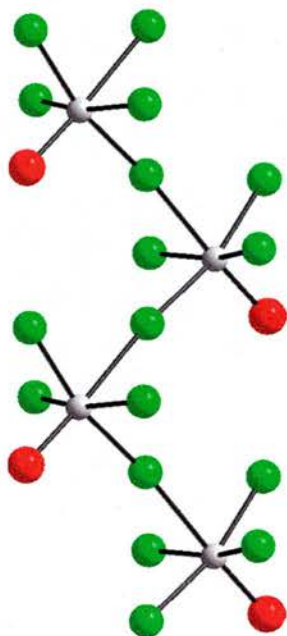


Figure 1.31: The *cis*-connected chain in  $(\text{NH}_4)_2[\text{VOF}_4]$ .

Another example of *cis*-connected chains is  $K_2VO_2F_3$  [46]. These chains are very similar to the ones shown in the previous structure, except for an additional O atom. This lies *cis* to the original O atom and causes the structure to gain symmetry and become centrosymmetric. These chains are shown in Figure 1.32. Each V atom is now shifted further away from the centre of each  $VO_2F_4$  octahedron towards the two O atoms.

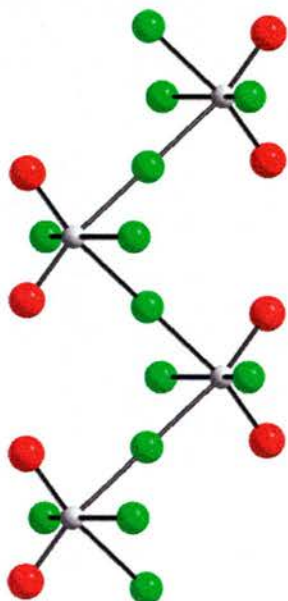


Figure 1.32: The *cis*-connected chain in  $K_2VO_2F_3$ .

$\text{CsVOF}_4$  shows chains of cis-connected  $\text{VOF}_5$  octahedra *via* F atoms [47]. Figure 1.33 shows two chains that align in an antiparallel fashion. As expected, the V atom is displaced from the centre of each octahedron towards the O atom. The V-F bond distance *trans* to the V=O bond is 2.3 Å, and the V-F bridging bond distance is only slightly longer than the terminal V-F bond distances of 1.93 Å. The caesium atoms co-ordinate to 16 F atoms by a bond distance of around 3-3.5 Å.

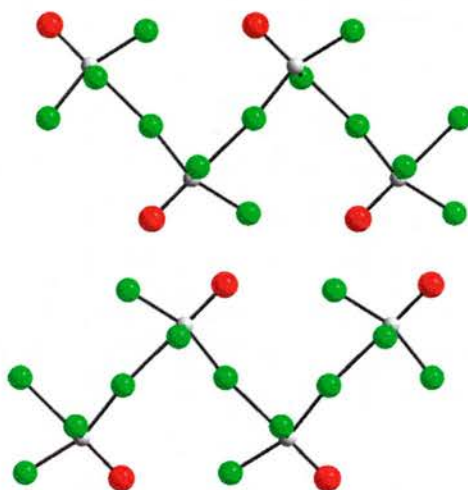


Figure 1.33: The antiparallel *trans*-connected chains in  $\text{CsVOF}_4$ .

$[\text{C}_4\text{H}_{12}\text{N}_2][\text{LiBe}_2\text{F}_7]$  was synthesised hydrothermally, followed by slow evaporation[48]. It consists of distorted  $\text{BeF}_4$  and  $\text{LiF}_4$  tetrahedra. Each  $\text{LiF}_4$  tetrahedron is connected to two  $\text{BeF}_4$  tetrahedra *via* the corners so a three-membered ring is formed along the edges. This three-ring unit is connected to another in a herring bone fashion to form the chains and 4-membered rings. This 3- and 4-ring arrangement is also known in  $\text{Be}_2\text{AsO}_4\text{OH}\cdot 4\text{H}_2\text{O}$  [49], and the synthetic mineral moräsite.

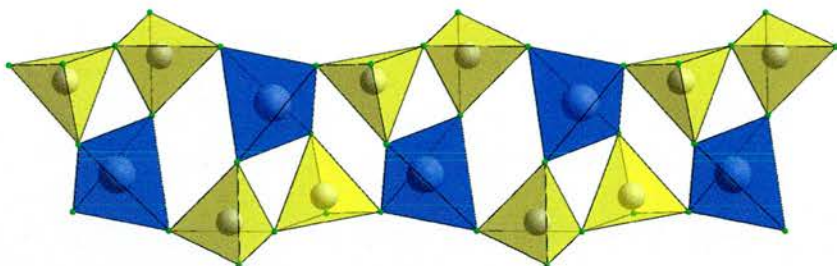


Figure 1.34: The  $[LiBeF_7]^{2-}$  chain in  $[C_4H_{12}N_2][LiBe_2F_7]$  with  $LiF_4$  tetrahedra in blue and  $BeF_4$  tetrahedra in yellow.

The structure of  $Ba_2TiOF_6$ , produced by Crosnier and Fourquet [50], is composed of *trans* connected chains of  $TiO_2F_4$  octahedra, which run along the *c*-axis. This is shown in Figure 1.35. The Ti-O-Ti bond angle is  $143.5^\circ$ , and the chains are separated by barium cations and fluoride anions. The Ti atoms are displaced from the center of the octahedron by  $0.19 \text{ \AA}$  along the direction of the chains. It crystallises in the polar space group *Cc*, so it exhibits SHG behaviour.

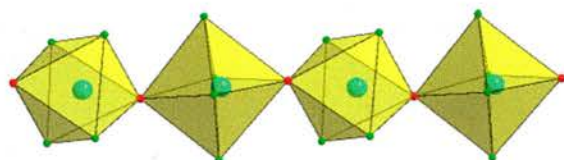


Figure 1.35: The *trans*-connected chain in  $Ba_2TiOF_6$

The same two authors, along with Duroy [51] corrected the formula Fischer *et al* thought for the structure of  $CuNb(OH, F)_7 \cdot 3H_2O$  [52]. It is built up of alternating  $Cu(H_2O, F, OH)_6$  and  $Nb(F, OH)_6$  octahedra linked together via a corner sharing F atom to form chains. The bridging F atoms bond to the Cu atom by a distance of  $2.3 \text{ \AA}$ , and the shorter equatorial Cu-

(H<sub>2</sub>O, OH, F) bond distances are much closer to 1.96 Å. This is due to the Jahn-Teller effect. The chains are connected together *via* hydrogen bonding. There was disorder between the water molecules, OH and F ligands.

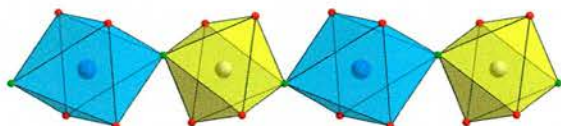


Figure 1.36: The chain in  $\text{CuNb}(\text{OH}, \text{F})_7 \cdot 3\text{H}_2\text{O}$ .  $\text{Cu}(\text{H}_2\text{O}, \text{F}, \text{OH})_6$  octahedra are in blue and the  $\text{Nb}(\text{F}, \text{OH})_6$  octahedra are in yellow.

### 1.2.13 Sheets

The  $\text{AMF}_4$  compounds such as  $\text{AAlF}_4$ , where  $\text{A} = \text{K}, \text{Rb}, \text{NH}_4$  and  $\text{Tl}$ , comprise of sheets of corner sharing  $\text{AlF}_6$  octahedra. There are several variations of  $\text{AAlF}_6$  by Brosset[53] and Fourquet *et al*[54] and are described in Figure 1.37.

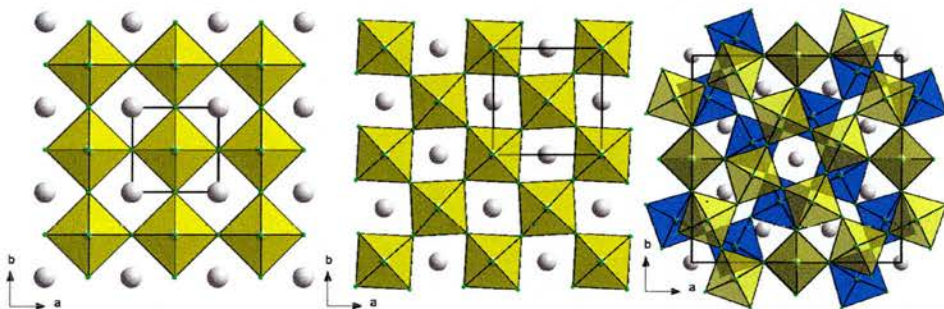
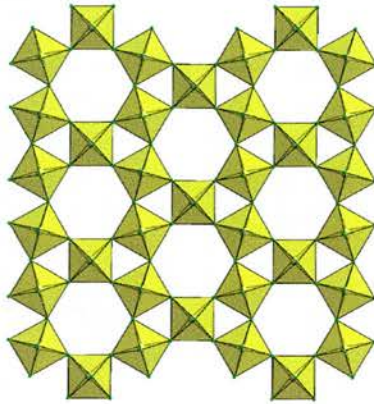


Figure 1.37: Three versions of  $\text{AAlF}_4$ , Brosset (left) and Fourquet (centre and right).

Brosset describes a simple arrangement of  $\text{AlF}_6$  octahedra corner sharing along the  $a$ - $b$  plane, and  $\text{Rb}^+$  cations placed in between the layers. Fourquet has shown a similar layout, except that the  $\text{AlF}_6$  octahedra are rotated.

Another structure is also shown, except sheets resembling the TTBs are rotated. These materials are the Dion-Jacobson types.

Courbion, Jacobini and De Pape [55] synthesised  $\text{Cs}_2\text{NaAl}_3\text{F}_{12}$ , which consists of corner sharing  $\text{AlF}_6$  octahedra. This forms three-membered rings and six-membered rings in the similar fashion to the hexagonal tungsten bronzes. The unit cell in this case is rhombohedral. The octahedra connect together to form  $[\text{AlF}_4]^-$  sheets, which are separated by the  $\text{Cs}^+$  and  $\text{Na}^+$  cations. The sheets also eclipse each other. The  $[\text{AlF}_4]^-$  sheets resemble the perovskites.



*Figure 1.38: The  $[\text{AlF}_4]^-$  sheet in  $\text{Cs}_2\text{NaAl}_3\text{F}_{12}$ .*

So far, the structures mentioned concern transition metals. Recently, the actinides have proved a fruitful source of novel materials with  $[\text{C}_2\text{H}_{10}\text{N}_2][\text{U}_2\text{F}_{10}]$  by Almond and co-workers [56]. It is composed of  $\text{UF}_9$  tricapped trigonal prisms, which share two edges and three corners with other polyhedra. The layer is shown in Figure 1.39. These layers are separated by ethylenediammonium cations. One unique F atom points into the space between the layers and hydrogen bonds to the nitrogen atoms of the organic cations. One unique F atom points into the space between the layers and hydrogen bonds to the nitrogen atoms of the organic cations.

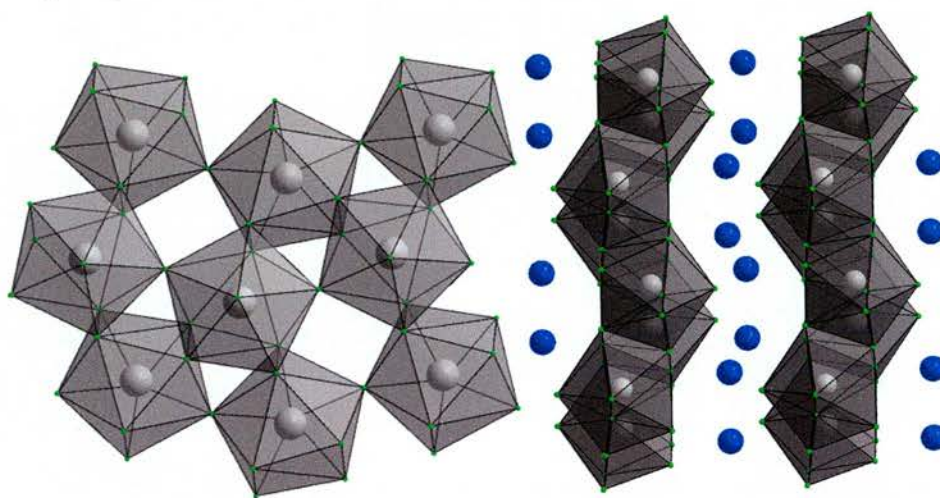


Figure 1.39: The  $[\text{U}_2\text{F}_{10}]^{2-}$  layer found in  $[\text{C}_2\text{H}_{10}\text{N}_2][\text{U}_2\text{F}_{10}]$  (left) and the sheet structure of  $\text{NH}_4\text{UF}_5$  (right).

$\text{NH}_4\text{UF}_5$  [57] exhibits layers separated by ammonium cations. These are also shown in Figure 1.39. It consists of  $\text{UF}_9$  mono-capped square antiprisms, which share corners and edges, and has a similar layer topology of  $[\text{C}_2\text{H}_{10}\text{N}_2][\text{U}_2\text{F}_{10}]$ .

### 1.2.14 3-Dimensional Structures

$\text{CrOF}_3$  [58] adopts an interesting 3-D structure. It consists of  $\text{CrOF}_5$  octahedra, where the Cr atoms are displaced from the centre towards the O atom. These connect together along the 4-fold screw axis to form helical chains shown in Figure 1.40, bridged by F atoms to adjacent chains. Each octahedron has one terminal F atom, one terminal O atom and the other four F atoms take part in the bridging. There was an uncertainty of which of the enantiomorphic space groups,  $P4_1$  or  $P4_3$  was correct. Both structure solutions have similar weighted R-factors.

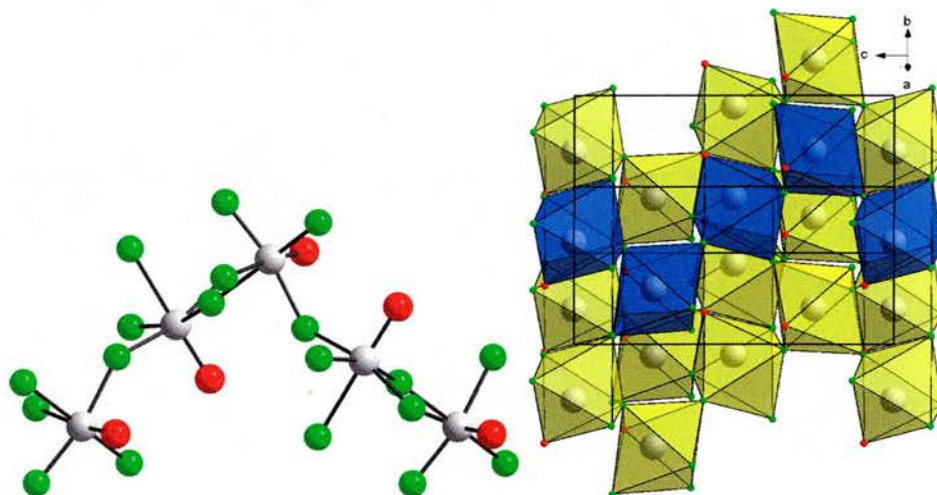


Figure 1.40: Part of the  $\text{CrOF}_3$  helical chain (left) and the stacking of the helical chains along the  $c$ -axis (right).

$\text{NH}_4\text{Y}_3\text{F}_{10}$  [59] is part of a larger family of compounds including this cubic form and the hexagonal form  $\text{NH}_4\text{Er}_3\text{F}_{10}$  [60], amongst others. It consists of  $\text{YF}_8$  square antiprisms, which connect together *via* their corners to form a larger  $[\text{Y}_6\text{F}_{36}]^{18-}$  cubo-octahedron.

The cubo-octahedron, which resembles the shape of a Maltese cross is shown in Figure 1.41.

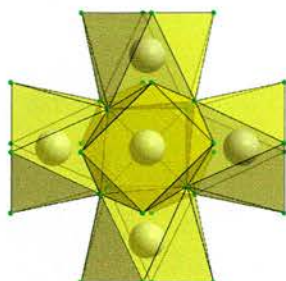


Figure 1.41: The  $[M_6F_{36}]^{18-}$  cage in  $NH_4Er_3F_{10}$ .

This unit is connected together in a similar way that C atoms do in the diamond structure. This is shown in Figure 1.42. The  $AM_3F_{10}$  types are therefore a modification of the diamond structure. Because of the similarity in ionic size between  $NH_4^+$  and  $K^+$ ,  $KY_3F_{10}$  [61] is isostructural.

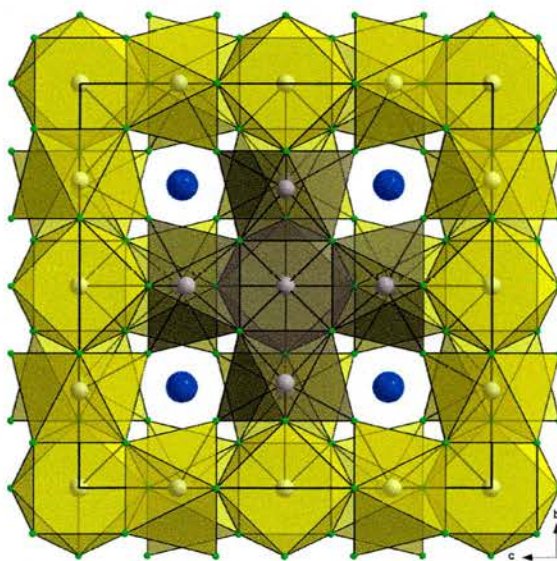


Figure 1.42:  $NH_4Y_3F_{10}$  with the  $[Y_6F_{36}]^{18-}$  cage highlighted in grey.

$BaY_2F_8$  consists of  $YF_8$  square antiprisms, which link together *via* edges to form a structure with distorted hexagonal ring channels [62]. Figure 1.43 shows the structure as well as the disordering of some F atoms, believed to be caused by tilting of the polyhedra. The ring channels are formed by the eclipsing of 6-membered rings of  $YF_8$  square antiprisms. In this respect, it bears a resemblance to the HTBs.

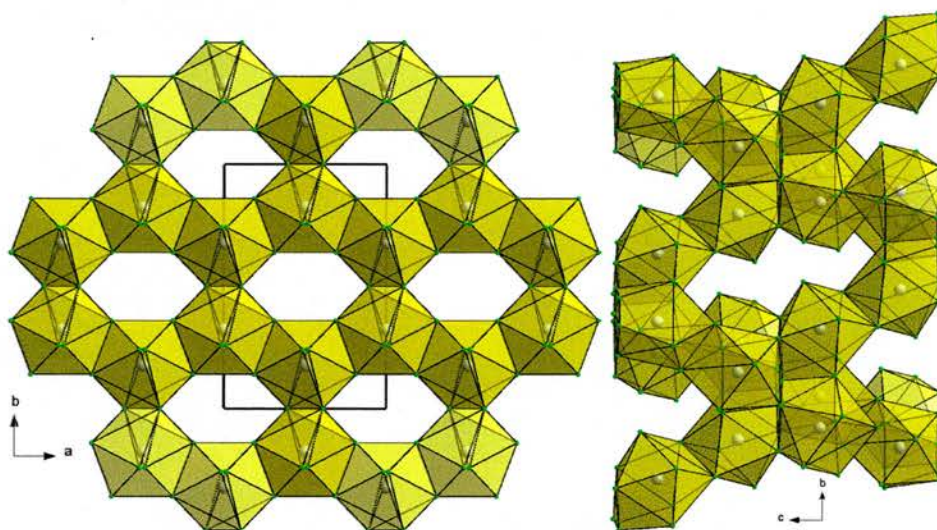


Figure 1.43:  $BaY_2F_8$  (left) and  $Ba_4Y_3F_{17}$  (right).

$Ba_4Y_3F_{17}$  [63] consists of the same cubo-octahedron in  $NH_4Y_3F_{10}$  and is also shown in Figure 1.43. These cages are prominent in yttrium fluoride chemistry, and also seen in uranium fluoride chemistry. In  $Ba_4Y_3F_{17}$ , they link together by four edges to form a more complex structure than  $NH_4Y_3F_{10}$ , consisting of eight-membered rings, which create larger open cages.

A complex uranium fluoride prepared by Bean *et al* [64], shown in Figure 1.44, has tricapped trigonal prismatic  $\text{UF}_8(\text{H}_2\text{O})$  polyhedra. The long U-O bond length of 2.5 Å, suggested a water molecule was bonded to the polyhedra. They edge and corner share to  $\text{NiO}_2\text{F}_4$  octahedra. The  $\text{UF}_8(\text{H}_2\text{O})$  tricapped trigonal prisms edge share with one another to form 1-dimensional chains. These are linked together *via trans*-connected  $[\text{Ni}(\text{H}_2\text{O})_2\text{O}_2\text{F}_4]$  octahedra. The water molecules protrude into channels running along the *c*-axis.

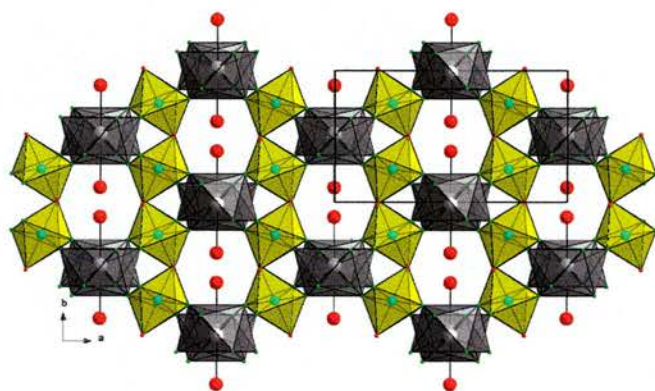


Figure 1.44:  $\text{Ni}(\text{H}_2\text{O})_2\text{UF}_6(\text{H}_2\text{O})$  along the *c*-axis.

$(\text{NH}_4)_7\text{U}_6\text{F}_{31}$  by Almond *et al* [65] was known to be isostructural with  $\text{Na}_7\text{Zr}_6\text{F}_{31}$ . It is composed of  $\text{UF}_8$  square antiprisms, which edge- and corner-share to form a 3-dimensional framework composed of  $\text{U}_6\text{F}_{36}$  cubooctahedra, already seen in yttrium fluoride chemistry, shown in Figure 1.45. The connections of the cubooctahedra form ring channels, where the  $\text{NH}_4^+$  cations lie.

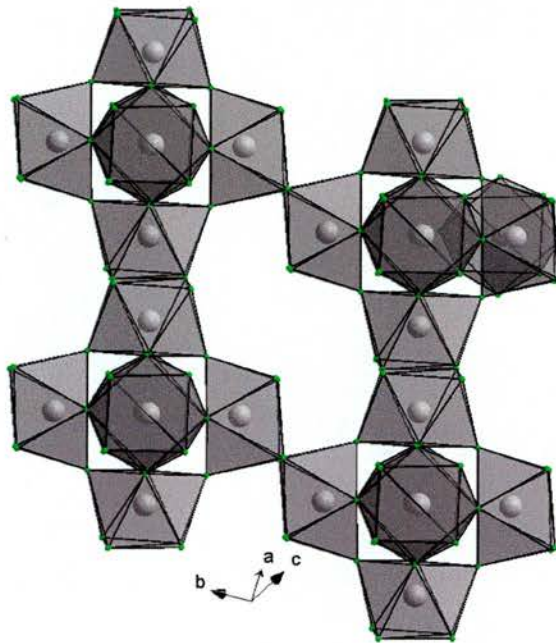


Figure 1.45: The connection of the cubooctahedra in  $(\text{NH}_4)_7\text{U}_6\text{F}_{31}$ .

$\text{UO}_2\text{F}_4$  [66] consists of  $\text{UO}_2\text{F}_4$  pentagonal bipyramids, which corner share to form a hexagonal array of 6-membered ring channels. The  $\text{U}=\text{O}$  bond length pointing towards the centre of the channels is 1.85 Å long. This is much shorter than the  $\text{U}-\text{F}$  bond distances of 2.25 Å, but the  $\text{U}-\text{F}$  bond distance *trans* to the  $\text{U}=\text{O}$  bond is only 1.87 Å. This is counter-intuitive considering

the examples of vanadium and niobium chemistry, where the *trans* M-F bond is much longer than the M=O bond. Notwithstanding, there is no appreciable out of centre distortion of the uranium atom towards any other atoms within the  $\text{UOF}_4$  pentagonal bipyramids.

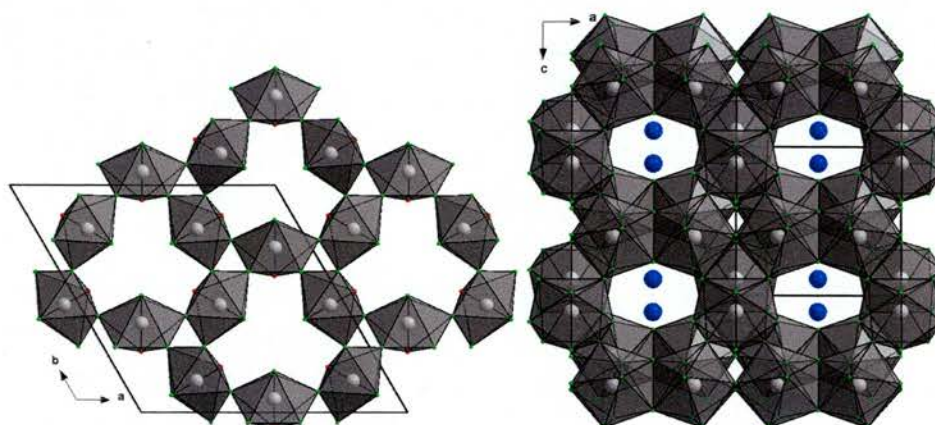


Figure 1.46: The hexagonal channels of  $\text{UOF}_4$  along the *c*-axis (left) and the complex channel structure of  $\text{NH}_4\text{U}_3\text{F}_{13}$  (right).

$\text{NH}_4\text{U}_3\text{F}_{13}$  [67] consists of  $\text{UF}_9$  mono-capped square antiprisms, which share corners and edges with one another. Rings of six eclipse each other to form hexagonal channels. This is also shown in Figure 1.46.

## 1.3 Physical Properties

### 1.3.1 Properties of Fluorides

Elemental fluorine is highly electronegative, and has a dissociation energy much lower than that of the other halides. This results in a relatively high reactivity with other elements [68]. It is also the smallest anion of its row in the periodic table because of a high nuclear charge. The M=O bonds in oxyfluorides are often stronger than the corresponding M-F bonds, because of  $\pi$ -bonding. The applications of fluorides are numerous, with Teflon the most famous example. Teflon is inert to HF so it is used as the linings of autoclaves in the experiments discussed in further chapters.

Fluorides are good electronic insulators because of large band gaps (6 eV or more) and empty conduction bands; a consequence of the element's high electronegativity. This can also contribute to the transparency of inorganic fluorides showing excellent optical properties. Of these are a small refractive index, due to the weak polarisability of the fluoride anion, and transparency to UV light. Most importantly are the non-linear properties (NLO) of certain non-centrosymmetric solids, which are useful in laser physics, infrared detectors and displays. These effects are discussed in more detail.

### 1.3.2 Second Harmonic Generation (SHG)

Light has an electric field  $\mathbf{E}$  associated with it [69]. When a photon interacts with electron density about a nucleus of an atom, it is displaced. This results in a charge separation with an induced dipole  $\mu$ . The charge

distribution is polarised. For small fields, the displacement of charge is proportional to the strength of the electric field. The polarisation is given by

$$\mu(\omega) = \alpha_{ij}(\omega)\mathbf{E}(\omega) \quad (1.1)$$

where  $\alpha_{ij}$  is the linear polarisability tensor at frequency  $\omega$ . If the field oscillates, then the induced polarisation will match every aspect of the field (phase and frequency) in a linear manner. In the classical model, the electrons are bound to the nucleus by a harmonic potential. This means the force required to restore the position of the electron density to equilibrium is proportional to its displacement. There is a symmetrical electron density distribution about the nucleus with equal charge displacement in both directions of the displacement. The linear polarisation in bulk materials is given by

$$\mathbf{P}(\omega) = \chi_{ij}(\omega)\mathbf{E}(\omega) \quad (1.2)$$

where  $\chi_{ij}(\omega)$  is the linear susceptibility. The two common parameters, which relate to the bulk material are the refractive index  $n(\omega)$ , and dielectric constant  $\epsilon(\omega)$ . A classical linear optical effect is refraction, often seen in the difference in  $n(\omega)$  between glass and water.

In the presence of larger fields however, the polarisability itself can change so the induced polarisation becomes a nonlinear function of the field strength. The force to maintain equilibrium of the charge density is also nonlinear, since it is no longer proportionate to the displacement. The effects of nonlinear

polarisation are much more subtle than the effects of linear polarisation. The polarisation wave has a diminished maximum in one direction, and an accentuated maximum in the opposite direction. A Fourier analysis of this polarisation wave will produce a DC component, the fundamental and the second harmonic. This is shown in Figure 1.47.

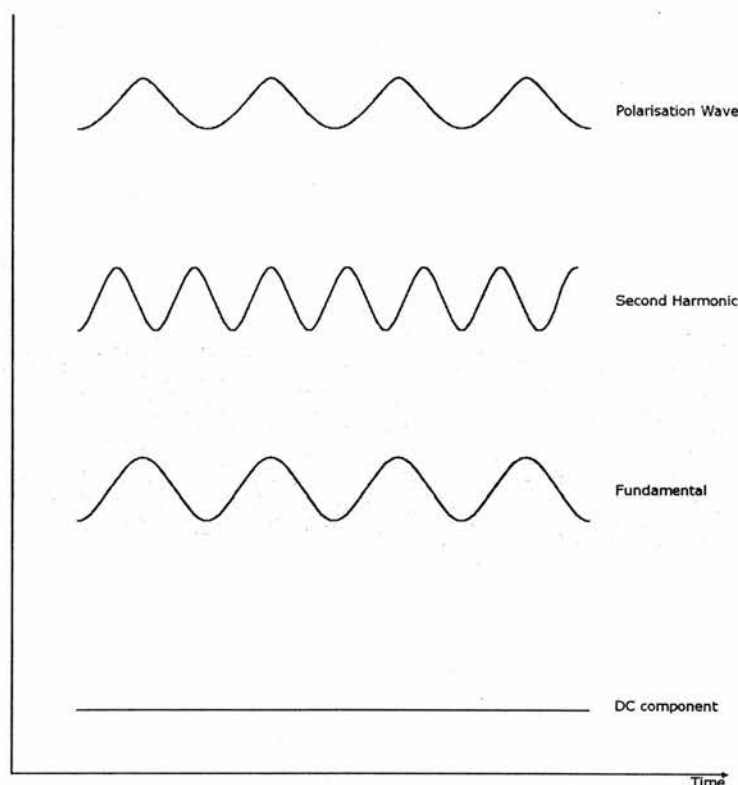


*Figure 1.47: The Fourier analysis of a polarisation wave.*

Only molecules and materials lacking a centre of symmetry are capable of non-linear optical properties. The effect of this is frequency doubling, but the observed light will be a summation of the fundamental and the second harmonic. A static electric field is also produced, known as optical rectification. The Pockels effect is where the refractive index of a material

is changed according to a static electric field. Light can be modulated to an applied AC voltage, important in optical switches, modulators and wavelength filters.

As well as the inorganic crystal structures, there has been a lot of work carried out on organic crystal structures, polymers and thin films [70]. These rely on non-centrosymmetry, with an asymmetric charge distribution along the conjugated  $\pi$  system of the organic molecules. This charge distribution provides for a large dipole moment, and a large non-linear optical susceptibility ( $\chi^{(2)}$  for second harmonic and  $\chi^{(3)}$  for third harmonic). Highly polar molecules have a tendency to align anti-parallel *via* hydrogen bonding or electrostatic interactions. This introduces centrosymmetry into the structure and results in zero  $\chi$ . The SHG materials are mostly utilised in the fields of communications and optical signal processing. Within the former, modulators, multiplexers and repeaters are required, a task fulfilled by  $\text{LiNbO}_3$  and  $\text{KH}_2\text{PO}_4$ . It is thought that polymers would be able to inhabit the latter category. Because of the intrinsic chirality of proteins and amino acids, they are expected to have similar properties to inorganic materials.

### 1.3.3 Piezo, Pyro and Ferroelectricity

Piezoelectric crystals can exhibit an electric polarity when a stress is imparted upon them [71]. This is the direct piezoelectric effect. Alternatively, an electric field can be applied to a crystal and it will change shape, the converse piezoelectric effect. The crystals must be non-centrosymmetric. A

centre of symmetry will cause polarisations to be inverted and therefore, the net change in polarisation will be zero. Piezoelectric crystals show a linear relationship between the force exerted and the polarisation, *via* the piezoelectric co-efficient.

If there is a unique polar axis, and the crystal is an electrical insulator, then a change in polarisation will arise from a change in temperature, which is pyroelectricity. When thermal expansion is restricted, the effect observed is primary pyroelectricity. When the crystal is allowed to expand freely, there is said to be a secondary pyroelectric effect.

If the polarisation can be reversed by an electric field in a hysteresis loop, then the material is said to be ferroelectric. All ferroelectric materials are piezoelectric, but since reversible polarisation is necessary for ferroelectricity, the reverse is not the case. They find use in ferroelectric RAM, and in capacitors because of their large dielectric constants [72]. The dielectric constant of a ferroelectric obeys the Curie-Weiss law

$$D = D_{\infty} + \frac{C}{T - T_c} \quad (1.3)$$

where  $D_{\infty}$  is the dielectric constant,  $T_c$  is the Curie temperature and  $C$  is the Curie constant.

### 1.3.4 Magnetism

The compounds of transition metals with unpaired electrons give rise to magnetic behaviour[73]. A random distribution of magnetic spins in

solution produces paramagnetic behaviour at a high temperature because of thermal disordering. If the magnetic spins are ordered in a crystal lattice, the unpaired electrons can interact with each other, resulting in particular alignments. Ferrimagnetic behaviour arises when magnetic moments of differing size align antiparallel, resulting in a net moment. The unpaired electrons can also align in particular directions and interact with each other from atom to atom. In the antiferromagnetic case, the alignments are antiparallel and the same size, while in ferromagnetic materials, the alignments are parallel and the same size.

These magnetic interactions can be overcome by thermal energy. The temperature dependence of the magnetic susceptibility is shown in Figure 1.48.

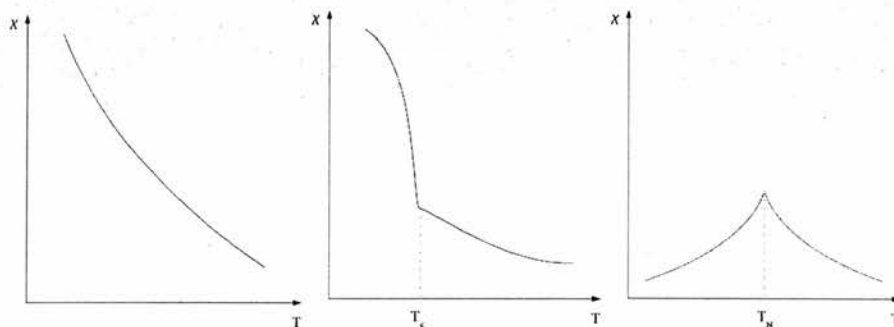


Figure 1.48: The temperature dependence of  $\chi$  in a paramagnetic (left), ferromagnetic (centre) and antiferromagnetic (right) material.

The magnetic susceptibility,  $\chi$  is a measure of the magnetisation of a material when placed in a magnetic field. A paramagnetic material placed in a magnetic field will allow the individual moments to align, and  $\chi$  increases

with decreasing temperature as the thermal disordering is overcome.  $\chi$  is related to temperature in the paramagnetic case in Equation 1.4.

$$\chi = \frac{C}{T - \theta} \quad (1.4)$$

$C$  and  $\theta$  are the Curie and Weiss constants and  $T$  is temperature. When the temperature is decreased to the Curie temperature in a ferromagnetic material, the magnetic susceptibility increases rapidly, because all of the spins align in the same direction. When the temperature is decreased in an antiferromagnetic material, the magnetic susceptibility decreases rapidly at the Néel temperature, because the magnetic moments align antiparallel and cancel each other out.

### 1.3.5 Superexchange

The mechanism of superexchange can cause magnetic ordering in inorganic materials, especially where metal cations are separated by an anion, such as O or F. Pairs of antiparallel spins are formed by the interaction between unpaired electrons of the metal cations and the ligand anions throughout the structure. These interactions may take place along infinite chains or within isolated units. This can also occur in ferromagnetic and antiferromagnetic materials. The interactions can break down due to thermal disordering. The Néel temperature increases when the orbital overlap increases. The ferrite spinels have interesting magnetic properties, which has led to their use in transformer cores and magnetic recording media.

In  $\text{Fe}_3\text{O}_4$ , above 122 K, the mixed valence  $\text{Fe}^{2+}$  and  $\text{Fe}^{3+}$  octahedral

sites are ferromagnetic, due to double exchange. This is where the magnetic moments of the  $\text{Fe}^{3+}$  and  $\text{Fe}^{2+}$  cations are aligned parallel to each other, so the  $t_{2g}$  electron of the  $\text{Fe}^{2+}$  cation jumps to the  $\text{Fe}^{3+}$  cation. This net moment is much larger than the antiferromagnetic coupling between the  $\text{Fe}^{3+}$  cations in the tetrahedral sites, which occurs *via* superexchange.

### 1.3.6 $d^1$ cations

Compounds of the transition metals in the  $d^1$  electronic configuration exhibit interesting magnetic properties.  $(\text{VO})_2\text{P}_2\text{O}_7$  [74] has been shown recently to exhibit the spin 1/2 alternating antiferromagnetic chain model. It was previously thought that it follows the spin-ladder arrangement [75], where a pair of  $S = 1/2$  Heisenberg antiferromagnetic chains connect antiferromagnetically to form a ladder structure. It is proposed that the spin-ladder possess an unusual singlet ground state. The magnetic structure of  $(\text{VO})_2\text{P}_2\text{O}_7$  has superexchange interactions through V-O-V linkages within each dimer and super-superexchange interactions through V-O...O-V linkages between each dimer and is shown in Figure 1.49.

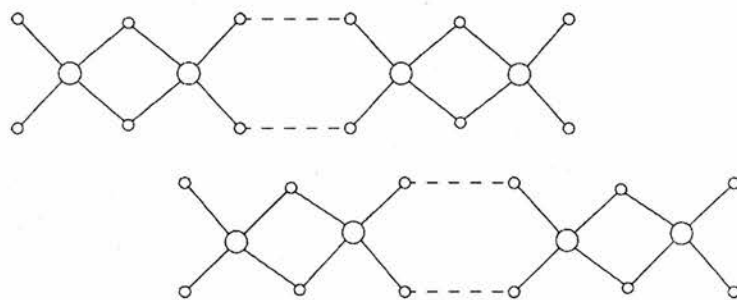


Figure 1.49: The arrangement of V atoms (large circles) and O atoms (small circles) in the ribbon chains in  $(\text{VO})_2\text{P}_2\text{O}_7$ .

Because the strength of the two types of interactions are different, a spin gap develops. In this particular example, there are two spin gaps because each chain is different in so far as the displacement of the V atoms from the centre of the  $\text{VO}_5$  square pyramids.

### 1.3.7 Magnetic Frustration

Conceived by G. Toulouse [76], frustration is the restriction of the satisfaction of all magnetic interactions in a lattice. In a square lattice, all of the magnetic moments on each corner of the square can either point in one direction, or in alternating directions. There is no magnetic frustration here, because all magnetic moments are satisfied in their orientation. In a triangular lattice, there are now only three magnetic moments, one on each corner. If a first magnetic moment points upwards, the second neighboring one points downwards, then no matter which orientation the third adopts, there will always be an antagonistic interaction. Thus, there will always be a frustrated bond in this system. This is shown in Figure 1.50.

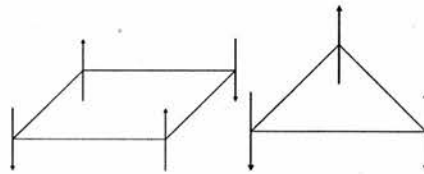


Figure 1.50: A square and triangular platelet.

## 1.4 Aims

There is a wide range of options for creating novel transition metal fluorides with interesting physical properties. This work concerns two areas.

(i). Trivalent cations such as Sc, Y, and La can be used to create novel structure types, which takes advantage of high co-ordination. Trivalent metal fluorides possess very good luminescence potential, if doped with some lanthanides. (ii) Early transition metal fluorides can also provide for interesting optical properties related to non-centrosymmetry, such as second harmonic generation (SHG).  $\text{KTiOPO}_4$  (KTP) for example, is widely used in the frequency doubling of Nd lasers.

The experimental techniques used in this work are outlined in Chapter 2. Subsequent chapters discuss the synthesis and characterisation of some new transition metal fluorides. These techniques include X-ray crystallography, scanning electron microscopy (SEM), SHG measurements and thermogravimetric analysis.

## References

- [1] G. Férey, *J. Solid State Chem.*, 2000, **152**, 37.
- [2] L. A. Villaescusa, P. Lightfoot, and R. E. Morris, *Chem. Comm.*, 2002, 2220.
- [3] L. A. Villaescusa, I. Bull, P. S. Wheatley, P. Lightfoot, and R. E. Morris, *J. Mater. Chem.*, 2003, **13**, 1978.
- [4] X. Wang, L. Liu, and A. Jacobson, *J. Am. Chem. Soc.*, 2002, **124**, 7812.
- [5] I. Bull, L. A. Villaescusa, S. J. Teat, M. A. Cambor, P. A. Wright, P. Lightfoot, and R. E. Morris, *J. Am. Chem. Soc.*, 2000, **122**, 7128.
- [6] C. Serre, F. Taulelle, and G. Férey, *Chem. Comm.*, 2003, 2755.
- [7] N. S. P. Bhuvanesh and J. Gopalakrishnan, *J. Mater. Chem.*, 1997, **7**, 2297.
- [8] M. E. Welk, A. J. Norquist, F. P. Arnold, C. L. Stern, and K. P. Poeppelmeier, *Inorg. Chem.*, 2002, **41**, 5119.

- [9] H. K. Izumi, J. E. Kirsch, C. L. Stern, and K. R. Poeppelmeier, *Inorg. Chem.*, 2005, **44**, 884.
- [10] P. S. Halasyamani and K. R. Poeppelmeier, *Chem. Mater.*, 1998, **10**, 2753.
- [11] I. Voloshina, R. Gerr, M. Antipin, V. Tsirel'son, N. Pavlova, Y. Struchkov, R. Ozerov, and I. Rez, *Kristallografiya*, 1985, **30**, 668.
- [12] W. T. A. Harrison and M. L. F. Phillips, *Chem. Mater.*, 1999, **11**, 3555.
- [13] K. Fischer, *Z. Krist.*, 1969, **129**, 222.
- [14] H. Vincent and S. Nicopoulos, *J. Solid State Chem.*, 1992, **98**, 386.
- [15] R. Enjalbert, P. Lecante, and J. Galy, *Acta Cryst. C*, 1986, **42**, 1465.
- [16] A. W. Hewat, *J. Phys. C*, 1973, **6**, 2559.
- [17] F. A. Cotton, G. Wilkinson, and P. L. Gaus, *Basic Inorganic Chemistry*, John Wiley and Sons, 2nd ed., 1987.
- [18] W. Massa and D. Babel, *Chem. Rev.*, 1988, **88**, 275.
- [19] G. M. Keith, C. A. Kirk, K. Sarma, N. M. Alford, E. J. Cussen, M. J. Rosseinsky, and D. C. Sinclair, *Chem. Mater.*, 2004, **16**, 2007.
- [20] H. Boysen and F. Altorfer, *Acta Cryst.*, 1994, **B50**, 405.
- [21] B. Noheda et al, *Phys. Rev.*, 2000, **B61**, 8687.
- [22] P. Norby et al, *Solid State Chem*, 1995, **119**, 191.

- [23] K. Barthelet, J. Marriot, D. Riou, and G. Férey, *J. Solid State Chem.*, 2001, **162**, 266.
- [24] L. Francke, E. Durand, A. Demourgues, A. Vimont, M. Daturi, and A. Tressaud, *J. Mater. Chem.*, 2003, **13**, 2330.
- [25] S. Fabbri, E. Montanari, L. Righi, G. Calestani, and A. Migliori, *Chem. Mater.*, 1989, **16**, 3007.
- [26] R. Mattes and H. Foester, *J. Solid State Chem.*, 1982, **45**, 154.
- [27] M. K. Chaudhuri, S. K. Chettri, D. Dey, G. C. Mandal, P. C. Paul, and W. Kharmawphlang, *J. Fluorine Chem.*, 1997, **81**, 211.
- [28] F. J. Brink, L. Noren, D. J. Goosens, R. L. Withers, L. Yun, and X. Chao-Nan, *J. Solid State Chem.*, 2003, **174**, 450.
- [29] P. A. Maggard, T. S. Nault, C. L. Stern, and K. R. Poeppelmeier, *J. Solid State Chem.*, 2003, **175**, 27.
- [30] M. P. Crosnier-Lopez, H. Duroy, and J. L. Fourquet, *J. Solid State Chem.*, 1993, **107**, 211.
- [31] M. Leimkühler and R. Mattes, *J. Solid State Chem.*, 1986, **65**, 260.
- [32] N. Buchholz, M. Leimkühler, L. Kirazis, and R. Mattes, *Inorg. Chem.*, 1988, **27**, 2035.
- [33] J. M. Dance, J. Mur, J. Darriet, P. Hagenmuller, W. Massa, S. Kummer, and D. Babel, *J. Solid State Chem.*, 1986, **63**, 446.

- [34] J. C. Deqan, A. J. Edwards, J. Y. Calves, and J. E. Guerschais, *J. Chem. Soc., Dalton. Trans.*, 1977, p. 978.
- [35] M. Dadachov, L.-Q. Tang, and X.-D. Zou, *Z. Krist., New Cryst. Struct.*, 2001, **216**, 141.
- [36] K. R. Heier, A. J. Norquist, C. W. Wilson, C. L. Stern, and K. R. Poeppelmeier, *Inorg. Chem.*, 1998, **37**, 76.
- [37] M. E. Welk, A. J. Norquist, C. L. Stern, and K. R. Poeppelmeier, *Inorg. Chem.*, 2000, **39**, 3946.
- [38] M. P. Crosnier-Lopez and J. L. Fourquet, *J. Solid State Chem.*, 1993, **103**, 131.
- [39] M. P. Crosnier-Lopez, H. Duroy, and J. L. Fourquet, *Z. Anorg. Allg. Chem.*, 1993, **619**, 1597.
- [40] G. Decap, R. Retoux, and Y. Calage, *Z. Anorg. Allg. Chem.*, 1993, **619**, 1850.
- [41] C. Ross II, B. Paulsen, R. Nielson, and S. Abrahams, *Acta Cryst. B*, 1998, **54**, 417.
- [42] T. Cameron, T. Klapotke, A. Schulz, and J. Valkonen, *J. Chem. Soc., Dalton Trans.*, 1993, p. 659.
- [43] L. Croguennec, P. Deinard, R. Brec, M. Couzi, C. Sourisseau, J. L. Fourquet, and Y. Calage, *J. Solid State Chem.*, 1997, **131**, 189.
- [44] M. Dadachov and L. Eriksson, *Acta Cryst. C*, 1999, **55**, 1739.

- [45] P. Bukovec and L. Golič, *Acta Cryst. B*, 1980, **36**, 1925.
- [46] R. R. Ryan, S. H. Mastin, and M. J. Reisfeld, *Acta Cryst. B*, 1971, **27**, 1270.
- [47] G. W. Bushnell and K. C. Moss, *Can. J. Chem.*, 1972, **50**, 3700.
- [48] L. A. Gerrard and M. T. Weller, *Chem. Comm.*, 2003, 716.
- [49] W. T. A. Harrison, T. M. Nenoff, T. E. Gier, and G. D. Stucky, *Inorg. Chem.*, 1993, **32**, 2437.
- [50] M. P. Crosnier and J. L. Fourquet, *J. Solid State Chem.*, 1992, **99**, 355.
- [51] M. P. Crosnier-Lopez, H. Duroy, and J. L. Fourquet, *J. Solid State Chem.*, 1994, **108**, 398.
- [52] J. Fischer, A. De Cain, and R. Weiss, *Bull. Soc. Chim.*, 1966, **8**, 2646.
- [53] C. Brosset, *Z. Anorg. Allg. Chem.*, 1938, **239**, 301.
- [54] J. L. Fourquet, F. Plet, and R. De Pape, *Acta Cryst. B*, 1980, **36**, 1997.
- [55] G. Courbion, C. Jacoboni, and R. De Pape, *Acta Cryst. B*, 1976, **32**, 3190.
- [56] P. M. Almond, L. Deakin, M. J. Porter, A. Mar, and T. E. Albrecht-Schmitt, *Chem. Mater.*, 2000, **12**, 3208.
- [57] R. A. Penneman and R. R. Ryan, *Acta Cryst. B*, 1974, **30**, 1966.
- [58] M. McHughes, R. D. Willet, H. B. Davis, and G. L. Gard, *Inorg. Chem.*, 1986, **25**, 426.

- [59] Z. J. Kang, Y. X. Wang, F. T. You, and J. H. Lin, *J. Solid State Chem.*, 2001, **158**, 358.
- [60] N. V. Podberezskaya, I. A. Baidina, S. V. Borisov, and N. Belov, *Zhurnal Strukturnoi Khimii*, 1976, **17**, 147.
- [61] A. Grzechnik, J. Nuss, K. Friese, J. Gesland, and M. Jansen, *Z. Krist.*, 2002, **217**, 460.
- [62] L. H. Guilbert, J. Y. Gesland, A. Bulou, and R. Retoux, *Mater. Res. Bull.*, 1993, **28**, 923.
- [63] B. Maksimov, H. Solans, A. Dudka, E. Genkina, M. Badria-Font, I. Buchinskaya, A. Loshmanov, A. Golubev, V. Simonov, and M. Font-Altaba, *Kristallografiya*, 1996, **41**, 51.
- [64] A. C. Bean, T. A. Sullens, W. Runde, and T. E. Albrecht-Schmitt, *Inorg. Chem.*, 2003, **42**, 2628.
- [65] P. M. Almond, L. Deakin, A. Mar, and T. E. Albrecht-Schmitt, *J. Solid State Chem.*, 2001, **158**, 87.
- [66] J. H. Levy, J. C. Taylor, and P. W. Wilson, *J. Inorg. Nuclear Chem.*, 1977, **39**, 1989.
- [67] H. Abzil, A. Cousson, and M. Pages, *Acta Cryst. B*, 1980, **36**, 2765.
- [68] P. Hagemuller, *Inorganic Solid Fluorides*, Academic Press, INC., 1985.
- [69] D. W. Bruce and D. O'Hare, *Inorganic Materials*, John Wiley and Sons, 1st ed., 1992.

- [70] P. N. Prasad and D. R. Ulrich, *Nonlinear Optical and Electroactive Polymers*, Plenum Press, New York, 1st ed., 1988.
- [71] A. K. Cheetham and P. Day, *Solid State Chemistry Comounds*, Clarendon Press, Oxford, 1st ed., 1992.
- [72] J. F. Nye, *Physical Properties of Crystals - Their Representation by Tensors and Matrices*, Oxford University Press, 9th ed., 1985.
- [73] M. T. Weller, *Inorganic Materials Chemistry*, Oxford Science Publications, first ed., 1994.
- [74] P. D. VerNooy, C. C. Torardi, and W. J. Marshall, *Inorg. Chem.*, 2002, **41**, 4664.
- [75] D. C. Johnston, J. W. Johnson, D. P. Goshorn, and A. J. Jacobson, *Phys. Rev. B*, 1987, **35**, 219.
- [76] G. Toulouse, *Commun. Phys.*, 1977, **2**, 115.

# Chapter 2

## Techniques

### 2.1 The Hydrothermal Method

The hydrothermal method [1] involves heating aqueous media above 100 °C, and above 1 bar of autogenous pressure in a closed container. Reactants, otherwise insoluble, can be dissolved in the hydrothermal fluid itself or mineralisers can participate in the reaction to increase solubility of the reactants. The method was introduced in the 1950's in order to mimic the processes which take place in nature to produce quartz and other naturally occurring solids. Pure samples of quartz can be produced in this way to mass produce oscillator crystals and other materials important in the production of semiconductors.

Hydrothermal synthesis provides many advantages over other synthetic techniques. Oxidation states that are difficult to attain otherwise can be achieved. Phases with low melting points can be produced, since hydrothermal reactions are usually performed at temperatures rarely exceeding 300 °C.

Metastable compounds that occur at specific temperature ranges can be produced. Unfortunately, there are more reaction variables to consider. These include temperature, volume, pH and pressure. These will need to be considered carefully.

Because of the high pressures involved, autoclaves are required to prevent the reaction vessel from bursting. Although polypropylene bottles can be used, these are limited to a maximum temperature of 100 °C, because the autogeneous pressure at elevated temperatures is sufficient to cause the bottle to burst. The autoclave is made of steel, which can withstand the pressures involved. The choice of material for the reaction vessel is important because of the corrosive nature of hydrothermal fluids. Iron, vanadium and even titanium are attacked by these conditions. Glass is resistant to neutral and acidic solutions but not solutions of hydrofluoric acid. The advantage of glass is that the progress of the reaction can be directly observed and monitored with FTIR. Teflon is ideal for the container because it is resistant to alkaline and hydrofluoric acid solutions. Teflon can only be used in a limited temperature and pressure range because it is slightly porous and could leak hydrothermal fluids into the outer metal jacket. This can cause it to corrode.

## 2.2 X-ray Diffraction

X-rays are produced by bombarding a metal with high energy electrons [2]. When these high energy electrons (or any accelerated charged particles)

collide with a metal target by decelerating over a very short distance, Bremsstrahlung radiation is generated. This continuous spectrum has a characteristic profile and energy cutoff. A few sharp peaks of high intensity appear on the continuum, which is shown in Figure 2.1. These are caused by collisions between the incident electrons and the inner electron shells of the metal atoms. The inner shell electron is expelled, and to fill the vacancy produced, an electron of higher energy occupies it. By doing so, radiation in the X-ray region of the electromagnetic spectrum is produced.

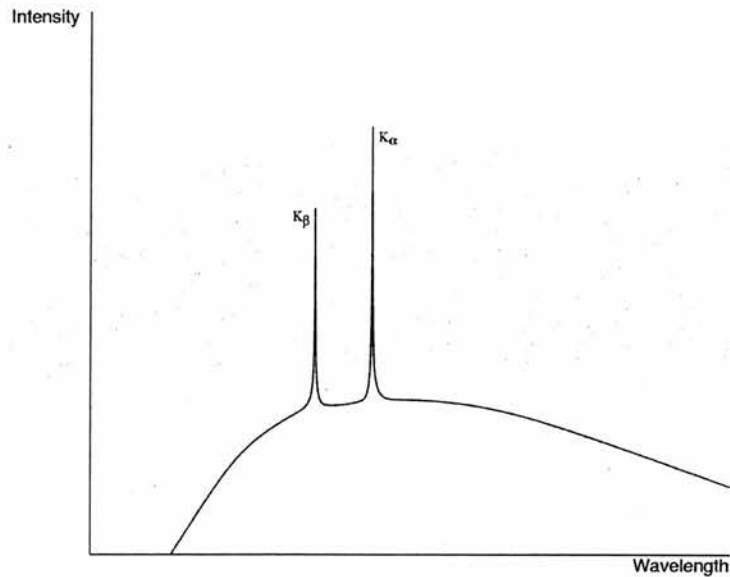


Figure 2.1: A graph of the X-ray emission from a metal.

The vacancies can be filled by electrons of varying energy levels. These mostly correspond to transitions from the  $n=2$  shell or the  $n=3$  shell. These produce X-rays at different wavelengths,  $K_{\alpha}$  and  $K_{\beta}$  respectively. These wavelengths are split into  $K_{\alpha 1}$ ,  $K_{\alpha 2}$ ,  $K_{\beta 1}$  and  $K_{\beta 2}$  wavelengths. For the

X-rays to be used in an experiment, they will need to be filtered by the monochromator to produce X-rays of one wavelength (either  $K_\alpha$  or  $K_\beta$ ).

In practice, the electrons are produced by thermionic emission from a heated cathode in an evacuated glass or metal envelope. They advance to a cooled positively charged anode of a specific metal to produce X-rays of a specific group of wavelengths. These include  $CuK_\alpha$  and  $MoK_\alpha$ .

X-rays can be diffracted by a crystal because the wavelength of the radiation is similar to the separation distance ( $d$ ) between lattice planes ( $hkl$ ). This is shown in Figure 2.2. This property was discovered by Max von Laue. The “reflections” appear on a detector as a series of spots. These are caused when X-rays constructively interfere with each other.

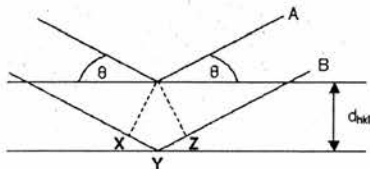


Figure 2.2: A diagram to represent the Bragg Law.

The incident and diffracted rays makes an angle ( $\theta$ ). For diffraction to occur, the path difference ( $n\lambda$ ) must be an integral number. This is expressed in Bragg's Law. X-ray B has a longer path length than X-ray A, which forms the angle X-Y-Z.

$$n\lambda = 2d_{hkl} \sin \theta \quad (2.1)$$

The lattice spacing can be calculated from the diffraction angle and the wavelength of the X-rays used. From this, the unit cell parameters can be determined. Reflections can be predicted by substituting values for  $h, k,$  and  $l$  along with their corresponding  $2\theta$  value. In a cubic system, for example, the lattice parameter,  $a$  is given by the following equation.

$$\sin \theta = (h^2 + k^2 + l^2)^{\frac{1}{2}} \frac{\lambda}{2a} \quad (2.2)$$

Lower symmetry structures have more complex equations for their respective lattice parameters. The interaction between X-ray photons and electrons can be thought of as perfectly elastic, where no energy is imparted from the X-ray photon to the electron, but it only changes direction [3]. When observed from zero degrees, the atomic scattering factor ( $f_0$ ) obtained gives the number of electrons directly. However, this is impractical because the beam-stop is at this angle. The purpose of the beam-stop is to prevent overloading of the detector by the unscattered beam and safety. Atomic scattering factors are given in the International Tables for Crystallography, Vol. C [4].

### 2.2.1 The Single Crystal Method

Single crystal X-ray data were collected on either a Bruker SMART diffractometer equipped with a CCD detector or a Rigaku Mercury CCD diffractometer. Both have area detectors which reduce the time required to collect data, as many data points can be collected at once. This is a major advantage over the traditional 4-circle diffractometer, where the

detector is allowed to move around three axes ( $\phi$ ,  $\chi$  and  $\omega$ ) and collects each individual  $hkl$  reflection in turn around  $\theta$ . Both use a molybdenum anode which produces  $K\alpha$  X-rays at  $0.7107 \text{ \AA}$ .

### 2.2.2 Direct Methods

Direct methods are a statistical approach for calculating the probability that the phases of the structure factors have a particular sign [5]. It assumes that all of the atoms within the unit cell have equal scattering factors and they are distributed randomly. All of the structure factors are placed on an absolute scale, normalised to the atoms scattering factors. The Sayre probability relationship is used to predict the sign of the phases, where the structure is centrosymmetric and  $\approx$  means 'probably equal to'. With non-centrosymmetric structures, the technique is more difficult, although this has been successful in this work.

$$S(hkl) \approx S(h'k'l') \cdot S(h - h', k - k', l - l') \quad (2.3)$$

For example, if  $hkl$  is the 442 reflection,  $h'k'l'$  is the 110 reflection, then the difference between the two is the 332 reflection. If  $E_{442}$  and  $E_{110}$  are both negative phases, it is probable that  $E_{332}$  is a positive phase.

$$P = \frac{1}{2} + \frac{1}{2} \tanh \left\{ \frac{1}{N} |E_{hkl} \cdot E_{h'k'l'} \cdot E_{h-h', k-k', l-l'}| \right\} \quad (2.4)$$

The purpose of  $E_{hkl}$  is to normalise  $F_{hkl}$  for the variation in scattering factor ( $f$ ) with angle of incidence of the x-rays and the element, where  $n$  is

for all atoms in the unit cell and  $\epsilon$  is normally unity.

$$|E_{hkl}|^2 = \frac{|F_{hkl}|^2}{\epsilon \sum_n f_n^2} \quad (2.5)$$

The probability ( $P$ ) depends upon  $|E_{hkl}|$  and is inversely proportional to the number of atoms in the unit cell. This means that the predictions become less precise if the number of atoms are too high. A small set of reliable phases is selected. The most phase combinations are used to generate the structure factors. These can be used to Fourier synthesise an electron density map ( $\rho(r)$ ).

$$\rho(r) = \frac{1}{V} \sum_{hkl} F_{hkl} e^{2\pi i(hx+ky+lz)} \quad (2.6)$$

### 2.2.3 Patterson Method

The Patterson method can be used instead, especially if there are some heavy atoms in the unit cell. A Patterson map is generated from  $|F_{hkl}|^2$  rather than  $|F_{hkl}|$ . This is an alternative approach to avoid the phase problem, because it is impossible to find the original phase of  $n^2$  by taking the square root of that number.

$$P(uvw) = \frac{1}{V} \sum_{hkl} |F_{hkl}|^2 \cos 2\pi(hx + ky + lz) \quad (2.7)$$

The resulting map will look like an electron density map but the peaks correspond to vectors between the atoms. The Patterson method is good for locating heavy atoms because the height of the peaks are proportional to the

atomic number. The contribution of the heavy atoms in the structure factor summation will be much greater than those of the lighter atoms.

### 2.2.4 Refinement

The approximate positions of the atoms found by either of the two previous methods can be optimised by least-squares refinement. The positions are adjusted so the following function is minimised.

$$D = \sum_{hkl} w_{hkl} (|F_{hkl}(obs)| - F_{hkl}(calc)|)^2 \quad (2.8)$$

$w_{hkl}$  is the weight given to the observation  $|F_{hkl}|$ . The thermal motion of the atoms have to be taken into account also.

$$|F_{hkl}(calc)| = \sum_n f_n \cos 2\pi(hx + ky + lz) e^{-B_n \sin^2 \theta / \lambda^2} \quad (2.9)$$

The isotropic temperature factor  $B_n$  is equal to  $8\pi^2 u_n^2$ , where  $u_n^2$  is the mean square amplitude of the vibration of atom n. Ultimately, the final refinement is anisotropic, represented by an ellipsoid with three parameters each for shape and direction. The  $R$  factor describes how well the refinement fits the data.

$$R = \frac{\sum_{hkl} |F_{hkl}(obs) - F_{hkl}(calc)|}{\sum_{hkl} |F_{hkl}(obs)|} \times 100\% \quad (2.10)$$

The reliability factor can also be weighted.  $wR$  is based on  $F_{hkl}^2$  for the structures described later.

$$wR = \frac{\sum_{hkl} w_{hkl} |F_{hkl}(obs) - F_{hkl}(calc)|}{\sum_{hkl} w_{hkl} |F_{hkl}(obs)|} \times 100\% \quad (2.11)$$

The  $R$  value after locating heavy atoms with the Patterson method, or locating approximate positions of atoms with direct methods would be around 20-30 %. Least-squares refinement would bring the factor down further to around 5 % for a good refinement. In order to detect any errors with the final model, the difference Fourier map is calculated.

$$\Delta(xyz) = \frac{1}{V} \sum_{hkl} (F_{hkl}(obs) - F_{hkl}(calc)) \cos 2\pi(hx + ky + lz) \quad (2.12)$$

The refinement is now complete, with an accurate representation of the contents of the unit cell. Chemical intuition will be required for this step, especially discerning the difference between, for example, N and C atoms. It can be used with visualisation software such as Diamond [6] or PLATON [7] to calculate bond lengths, angles, hydrogen bonding and the overall form of the structure. Thanks to the WinGX [8] and ShelX [9] software, this process is routine.

## 2.2.5 The Powder Method

Powder data were collected on a Stoe STADI-P powder diffractometer. The X-ray tube has a copper anode and the X-rays are monochromated from Germanium. The resultant X-rays are the  $\text{CuK}\alpha_1$  wavelengths at 1.5406 Å. The sample is held on a rotating disc and prevented from tumbling by the application of Vaseline, and the reflections are collected by a moving detector in the range of 5 to 80 °.

## 2.2.6 Rietveld Refinement

Rietveld refinement is the method of choice where single crystals are not available for conventional structure solution and refinement[10]. Least squares calculations are carried out until the best fit is obtained between the whole of the observed powder pattern and a calculated powder pattern based upon a structural model, which can be altered according to what is expected. The collected powder data is split into many steps ( $i$ ), and the intensity of the profile at each step is given as  $y_i$ . The best fit is the least-squares fit to all  $y_i$ 's simultaneously. The key is to minimise as much as possible the residual  $S_y$  summed over all data points

$$S_y = \sum_i w_i (y_i - y_{ci})^2 \quad (2.13)$$

where  $w_i = \frac{1}{y_i}$ ,  $y_i$  is the observed intensity at the  $i$ th step and  $y_{ci}$  is the calculated intensity at the  $i$ th step. The residual alone is not sufficient in providing a best fit. There is the danger of achieving a "false minimum", where by the refinement conditions may meet *statistical* criteria, but may

not make chemical sense. For this, modifications of the R factors from single crystal refinement can be used in a similar fashion (R-pattern and R-weighted pattern), as well as a  $\chi^2$  test.

$$R_p = \frac{\sum |y_i(obs) - y_i(calc)|}{\sum y_i(obs)} \quad (2.14)$$

$$R_{wp} = \left\{ \frac{\sum w_i (y_i(obs) - y_i(calc))^2}{\sum w_i (y_i(obs))^2} \right\}^{1/2} \quad (2.15)$$

The parameters commonly refined are the background, atom co-ordinates, isotropic displacement parameters, preferred orientation, the detector zero point (specifically for X-ray data) and peak shape. The shape of the peaks in a profile can vary with the type of diffractometer used, the sample crystallinity and the type of radiation used. To fit the peak shapes, many functions can be used, but the most widely utilised ones are Gaussian, Lorentzian and Pseudo-Voigt, which is a convolution of Gaussian and Lorentzian distributions. Gaussian is a symmetric distribution and Lorentzian is similar, except for a sharper triangular distribution. One of the most widely used software packages is the General Structure Analysis System (GSAS) [11].

## 2.3 Bond Valence Sum Calculation

It is sometimes necessary to calculate the valence of metal atoms if there is any ambiguity of the oxidation state. This can arise from different coordination species or changing of oxidation state of the metal centre during

the reaction. The following equation describes the bond valence sum ( $s$ ), where  $r'_0$  and  $B$  are constants tabulated by Brown and Altermatt [12] and  $r_{ij}$  is the bond length between two atoms  $i$  and  $j$ .

$$s = \sum_j \exp\left(\frac{r'_0 - r_{ij}}{B}\right) \quad (2.16)$$

$B$  is usually taken as being 0.37. The bond valence sums were calculated using the VaList [13] software.

## 2.4 Thermogravimetric Analysis (TGA)

Thermogravimetric analysis measures the change in weight of a sample as a function of its temperature [14]. The majority of TGA equipment are computer controlled. A typical chart shows a continuous line representing the weight of the sample with one or more steps which describes the weight loss at that particular temperature. These steps in weight loss can be a sharp sudden drop, or a gradual decay over a range of temperatures. A heating rate is typically between 1 and 20 °C min<sup>-1</sup>. The sample has a constant weight ( $W_i$ ) until the temperature ( $T_i$ ) reaches such a point that the sample starts to decompose over a range of temperatures ( $T_i$  to  $T_f$ ). A plateau is reached at  $T_f$ , corresponding to the weight ( $W_f$ ) of the residue left behind.

$$\Delta W = W_f - W_i \quad (2.17)$$

This is a fundamental property of the sample and can be used to calculate the products of compositional changes. Typically, this technique is combined

with powder XRD to determine the nature of the residue. One can work backwards, so to speak, and calculate some, if not all of the compositional changes.

TGA was performed on a TA Instruments SDT2960 simultaneous TGA/DTA furnace under an atmosphere of N<sub>2</sub>, mainly at a heating rate of 5 °C min<sup>-1</sup>. Samples of approximately 7-20 mg were heated up to anything between 500 and 750 °C, with a sample of calcined alumina of comparable weight as a standard. Weight loss was plotted as a function of temperature.

## 2.5 CHN Microanalysis

CHN Microanalysis was carried out on a Carlo Erba CHNS analyser. This is to detect quantities of carbon, hydrogen and nitrogen, to assess the condition of the template (remained intact or decomposed), and also to indicate the level of purity. For an impure sample, the percentage values would be dramatically different from those calculated from the crystal structure. This can serve as a guide to structural solution.

## 2.6 Optical Microscopy

Using a simple optical microscope, important information about a sample can be ascertained when viewed under magnification. It is necessary for the size of the crystals or powder to be larger than that of the wavelength of light (0.4 - 0.7 μm). Typically, the equipment can work in transmission

or reflection mode. Reflection is mostly used when observing biological organisms. The light is reflected off the sample and into the objective lens. Transmission is mainly used for the purposes outlined in this work, where light passes through the sample.

A light bulb is the usual source of light, which needs to be polarised. The plane polarised light passes through apertures to condition the intensity of the light. The light passes through focusing lenses and through the sample, and collected by the objective lens. An analyser may be placed before the objective lens to rotate the plane of the polarised light.

Samples are initially examined with the analyser out to observe the morphology and size of the crystals. With the analyser in, the isotropic or anisotropic nature of the crystals can be examined. Isotropic crystals allow the light to pass without the polarisation being modified. Under the analyser, they appear black. Although this can be a good indicator of cubic symmetry, glasses and powders exhibit this effect also. Anisotropic crystals modify the polarisation, so they appear coloured. This would indicate the non-cubic crystal systems. This technique can be used to assess the suitability of the crystals for single crystal X-ray diffraction. Rotation of the analyser can reveal the extinction directions. Extinction usually occurs at every  $90^\circ$  rotation. At every  $45^\circ$ , the sample exhibits maximum birefringence. Good quality crystals should show sharp extinctions. Crystal aggregates may show a more irregular extinction. If the extinction divides up into strips, there is a good chance that the crystal is twinned.

The purity of the sample can be examined if any impurity shows optical properties much different from the product in question. A good example is a collection of crystals amongst powder. Although optical microscopy is not utilised as much as it used to be, it is still a valuable tool for the crystallographer.

## 2.7 Electron Microscopy

The natural progression from optical microscopy is electron microscopy. This technique not only examines the morphology of the sample, but also the elemental composition of the sample. Instead of light being used, a beam of electrons is utilised resulting in vastly increased resolving power.

Transmission Electron Microscopy (TEM) involves inelastic and elastic scattering of electrons from a sample. The image arises from the amplitude contrast and the phase contrast of the scattered electrons. In amplitude contrast, the phases of the transmitted and diffracted beams do not combine while in phase contrast, they combine preserving their phases and amplitudes. The diffraction contrast is caused by Bragg scattering from crystalline samples. The image obtained is affected by the thickness of the sample and the angular range of the diffracted beams. The upshot of this is that TEM produces an image of the sample where all parts are in focus at the same time, making the interpretation of surface features difficult.

In Scanning Electron Microscopy (SEM) a fine beam of electrons rasters the sample. The intensities of scattered electrons are measured and displayed

on a monitor. The resolution is limited by the penetration of the electrons underneath the surface as well as the cleanliness of the surface. Topographic images are readily obtained and interpreted. A combination of both techniques leads to scanning transmission electron microscopy (STEM).

Compositional information can be readily obtained from the whole sample or localised spots. X-rays, which are produced from the bulk material in a similar fashion to how they are produced in X-ray crystallography, and back scattered electrons are all used in the microanalysis, because they provide element specific information.

## 2.8 MAS NMR Spectroscopy

Magic angle spinning (MAS) is used in solid state NMR to relieve the problem of signal broadening [15]. The magnetic field produced by a nucleus, its magnetic moment ( $\mu$ ) and the distance from the second nucleus ( $r$ ) in the  $B_0$  direction is related by the following equation.

$$H_b = \left(\frac{K\mu}{r^3}\right)(3\cos^2\theta - 1) \quad (2.18)$$

$K$  is a constant and  $\theta$  is the angle between the magnetic field  $B_0$  and the bond connecting the two nuclei. When this angle is at the "magic angle" of  $54.44^\circ$ ,  $H_b$  becomes zero, and the dipole-dipole interactions and the chemical shift anisotropy are averaged. In solution NMR, where molecules are tumbling randomly, only the average value of the chemical shift is important. In the solid state however, the chemical shifts are not averaged because the

nuclei are static and molecules in different orientations have different chemical shifts.

The sample is mounted in a cylinder at the magic angle and rotated at a frequency greater than the width of the spectrum. Due to practical limitations, this is limited to 25 kHz especially with gas driven sample spinners, but the techniques are advancing.

## 2.9 SHG Measurements

Second harmonic generation is a property in some non-centrosymmetric crystals, which changes the frequency of Laser light it interacts with. The origin of this effect has already been discussed in Chapter 1, and finds a practical use in telecommunications with fibre optics, piezoelectric transducers and general work with Lasers. SHG measurements were carried out using the 1064 nm radiation of a Nd-Vanadate laser. A polycrystalline thin-film is prepared and studied relative to a  $\text{LiNbO}_3$  standard. This method is only semi-quantitative, but reasonable measurements of SHG intensity and damage threshold can be measured.

## References

- [1] A. Rabenau, *Angew. Chem. Int. Ed. Engl.*, 1985, **24**, 1026.
- [2] P. W. Atkins, *Physical Chemistry*, Oxford University Press, 6th ed., 1998.
- [3] R. Jenkins and R. L. Snyder, *Introduction to X-Ray Powder Diffractometry*, John Wiley and Sons, 1996.
- [4] A. J. C. Wilson, ed. *International Tables for Crystallography, Vol. C: Mathematical, Physical and Chemical Tables.*, Kluwer Academic Publishers, Dordrecht, The Netherlands, 1992.
- [5] A. K. Cheetham and P. Day, *Solid State Chemistry Techniques*, Clarendon Press, Oxford, 1st ed., 1987.
- [6] K. Brandenburg, Diamond, Version 2.1, Crystal Impact GbR, Bonn, Germany, 2001.
- [7] A. L. Spek, *J. Appl. Cryst.*, 2003, **36**, 7.
- [8] L. J. Farrugia, *J. Appl. Cryst.*, 1999, **32**, 837.

- [9] G. M. Sheldrick , ShelXS97 and ShelXL97, Release 97-2. University of Göttingen, Germany, 1997.
- [10] R. A. Young, *The Rietveld Method*, IUCr, Oxford Science Publications, 1st ed., 1993.
- [11] A. C. Larson and R. B. Von Dreele , GSAS, Los Alamos National Laboratory, 1985-1994.
- [12] I. D. Brown and D. Altermatt, *Acta Cryst. B*, 1985, **41**, 244.
- [13] A. S. Wills and I. D. Brown , VaList, CEA, France, 1999.
- [14] A. R. West, *Solid State Chemistry and its Applications*, John Wiley and Sons, 1989.
- [15] J. W. Akitt, *NMR and Chemistry*, Chapman and Hall LTD, 2nd ed., 1983.

# Chapter 3

## Experimental

### 3.1 Synthesis

Around four hundred hydrothermal reactions were carried out in this work, and some interesting products are described in later chapters. Reactions were carried out in either a Teflon lined steel autoclave or a polypropylene bottle and heated in an oven for several days. After cooling, all products were washed in water or acetone if the products were water soluble, filtered and allowed to dry over night at room temperature. Most of the mixtures contained a metal source (1 mmol), a 48 % solution of HF in water, water and ethylene glycol in a 1:1 mixture and a structure directing amine. Sometimes,  $\text{NH}_4\text{F}\cdot\text{HF}$  was used when the 48 % solution of HF in water was unavailable. Reactants were ordered from Aldrich and used as received. Reactions took place at a wide range of pH values between 1 and 11, controlled by varying the amounts of HF and amine in the reactions. It was noted that at different pH values, other products were formed with the same structure directing

agent. These are shown in the "reactions" folder. Reactions in autoclaves were carried out up to 190 °C, and only 100 °C in polypropylene bottles.

Early work within this project was centred around the synthesis of novel germanium oxide microporous materials. This area of work was unsuccessful. It was not until the introduction of HF and  $\text{Sc}_2\text{O}_3$  into the reactions containing  $\text{GeO}_2$ , when several new scandium fluoride phases were synthesised. Attention was turned solely to the transition metal fluorides. Oxides, chlorides, nitrates and acetates were used as the sources of metals with varying degrees of success. For example,  $\text{Y}_2\text{O}_3$  was used as a source of yttrium. This was not successful, since it did not dissolve very well, even under fluoric hydrothermal conditions.  $\text{Y}(\text{NO}_3)_3 \cdot 6\text{H}_2\text{O}$  was chosen instead. This dissolves readily in water and upon addition of HF, a precipitate of  $\text{YF}_3$  was formed. Under hydrothermal conditions, this was more successful, producing two new organically templated yttrium fluorides. However,  $\text{TiO}_2$  and  $\text{Nb}_2\text{O}_5$  dissolved into the hydrothermal solution readily. A whole series of vanadium oxyfluorides has been produced with just  $\text{V}_2\text{O}_5$  as the source of vanadium. It was dissolved into HF and water to produce a bright yellow solution. To this, ethylene glycol was added and the colour of the solution changed to orange. To this solution, the organic amine template was added and the solution turned colourless. Over the period of the reaction, the colour of the solution changed once more to blue or green. Vanadium has a wide range of oxidation states and different colours associated with them. These colour changes shows that in most cases, the vanadium atom was reduced from  $\text{V}^{5+}$  to  $\text{V}^{4+}$ .

# Chapter 4

## Scandium Fluorides

### 4.1 Introduction

Several scandium fluorides are described in this chapter, denoted Sc-*n*. They range from isolated  $[\text{ScF}_6]^{3-}$  octahedral units,  $[\text{ScF}_5]^{2-}$  linear chains and  $[\text{ScF}_4]^-$  sheets to one three-dimensional structure.

Hydrothermal synthesis, X-ray crystallography, thermogravimetric analysis and CHN microanalysis experimental procedures were used throughout the work. X-ray data are shown in Table 4.1. All hydrogen atoms were refined riding upon their carrier atoms, except where stated. An original aim of this work was to prepare some scandium germanate frameworks. Sc-4 was the product of one of these reactions, which prompted further exploration of fluoride based systems. An SEM micrograph of Sc-4 was taken, whereas a MAS-NMR spectrum of Sc-2 was taken. SEM was used to detect quantities of germanium, which may have been included in the structure. Table 4.2 shows some of the reactions concerning the use of

GeO<sub>2</sub>, where en-GeO<sub>2</sub> refers to [Ge<sub>18</sub>O<sub>38</sub>(OH)<sub>4</sub>][C<sub>2</sub>N<sub>2</sub>H<sub>10</sub>]<sub>4</sub>·2H<sub>2</sub>O [1]. These reactions showed that Sc-2 formed in high pH conditions, and Sc-4 formed in low pH conditions. However, some of the experiments show that this relationship may be more complex. Originally, these reactions were part of the work concerning germanium oxide frameworks. Atomic co-ordinates and temperature factors are tabulated in Appendix A in the file "Appendices.pdf" on the CD-ROM. Bond lengths and angles are tabulated in Appendix B.

Table 4.1: Crystallographic parameters of scandium fluorides.

	Sc-1	Sc-2	Sc-3	Sc-4	Sc-5
Formula	$[\text{H}_3\text{O}][\text{C}_6\text{N}_2\text{H}_{16}][\text{ScF}_6]\cdot\text{H}_2\text{O}$	$[\text{C}_2\text{N}_2\text{H}_{10}][\text{ScF}_5]$	$\text{NH}_4\text{ScF}_4$	$[\text{C}_2\text{N}_2\text{H}_{10}]_{0.5}[\text{ScF}_4]$	$(\text{NH}_4)_2\text{Sc}_3\text{F}_{11}$
Formula weight	312.2	202.08	139	152.02	379.96
Crystal system	Monoclinic	Tetragonal	Orthorhombic	Triclinic	Orthorhombic
Space group	$P2_1/n$	$P4/ncc$	$Pm\bar{c}n$	$P\bar{1}$	$Cmmm$
$a(\text{Å})$	9.543(2)	13.035(2)	7.862(2)	8.889(1)	18.501(12)
$b(\text{Å})$	6.704(1)		8.088(2)	10.324(2)	6.613(5)
$c(\text{Å})$	9.873(2)	8.142(2)	13.503(4)	14.178(2)	4.025(3)
$\alpha(^{\circ})$	90.35(1)			83.299(3)	
$\beta(^{\circ})$				88.383(3)	
$\gamma(^{\circ})$				67.516(2)	
Volume( $\text{Å}^3$ )	631.6(2)	1383.4(5)	858.6(4)	1193.8(3)	492.5(6)
Crystal size (mm)	$0.03 \times 0.04 \times 0.1$	$0.2 \times 0.03 \times 0.02$	$0.1 \times 0.03 \times 0.02$	$0.1 \times 0.1 \times 0.1$	$0.19 \times 0.03 \times 0.0$
Z	2	8	8	10	2
$\mu(\text{mm}^{-1})$	0.651	1.091	1.666	1.508	2.149
Total reflections	1347	639	847	7112	1595
Observed reflections ( $I > 2\sigma(I)$ )	759	435	587	4301	291
$R, wR_2$ ( $I > 2\sigma(I)$ )	0.06, 0.14	0.05, 0.13	0.03, 0.09	0.04, 0.11	0.08, 0.19
$R, wR_2$ (all data)	0.09, 0.24	0.07, 0.15	0.04, 0.10	0.04, 0.12	0.08, 0.19

Table 4.2: Some reactions carried out with scandium fluorides.

GeO <sub>2</sub> (g)	Sc <sub>2</sub> O <sub>3</sub> (g)	H <sub>2</sub> O (ml)	48 % HF (ml)	HO(CH <sub>2</sub> ) <sub>2</sub> OH (ml)	C <sub>2</sub> N <sub>2</sub> H <sub>8</sub> (ml)	Piperazine (g)	pH	Product
0.1046	0.1379	2	1		1		1	ScF <sub>3</sub>
0.1046	0.1379	5	0.5	5	0.5	0.258	12	Sc-4 and ScF <sub>3</sub>
	0.1379	5	0.5	5	0.5	0.258	10	Sc-4
	0.1379	5	0.5	5	0.5		10	Sc-4
	0.1379	5	0.5		0.5		10	No product
0.2092	0.1379	5	0.5	5	0.5	0.258	10	Sc-4
0.2092	0.1379	5	0.5	5	0.5		10	Sc-2
0.2092	0.1379	5	0.5		0.5		10	en-GeO <sub>2</sub>
	0.1379	5	0.5	5	0.065		1	Sc-4
	0.1379	5	0.5	5	0.1		2	Sc-4
	0.1379	5	0.5	5	0.2		3	Sc-2
	0.1379	5	0.5	5	0.4		9	Sc-2
	0.1379	5	1	5	0.1		1	Sc-4
	0.1379	5	1	5	0.2		2	Sc-2 and Sc-4
	0.1379	5	1	5	0.4		3	Sc-2
	0.1379	5	1	5	0.75		9	Sc-2
	0.1379	5	0.25	5	0.1		9	ScF <sub>3</sub>
	0.1379	5	0.25	5	0.2		10	ScF <sub>3</sub>
	0.1379	5	0.25	5	0.4		12	ScF <sub>3</sub>

## 4.2 [H<sub>3</sub>O][C<sub>6</sub>N<sub>2</sub>H<sub>16</sub>][ScF<sub>6</sub>].H<sub>2</sub>O (Sc-1)

### 4.2.1 Experimental

#### Synthesis

0.1379 g (1 mmol) of Sc<sub>2</sub>O<sub>3</sub>, 5 ml of water and 1.5 ml of a 40 % solution of HF was heated in a polypropylene bottle for one hour at 100 °C. The contents of the bottle were transferred to a Teflon lined steel autoclave with 5 ml of ethylene glycol. The addition of 0.57 g (5 mmol) of *trans*-1,4-diaminocyclohexane gave a solution of pH 3. Heating for five days at 190 °C, the pH remained the same. The colourless prismatic crystals were washed in water and allowed to dry in air at room temperature overnight (Found: C, 21.17 %; H, 6.62 %; N, 8.22 %. [C<sub>6</sub>N<sub>2</sub>H<sub>16</sub>][H<sub>3</sub>O][ScF<sub>6</sub>].H<sub>2</sub>O requires C, 23.08 %; H, 6.78 %; N, 8.97 %).

#### Characterisation

During the refinement, it was thought that an extra NH<sub>4</sub><sup>+</sup> cation was present, because [ScF<sub>6</sub>]<sup>3-</sup> and [C<sub>6</sub>N<sub>2</sub>H<sub>16</sub>]<sup>2+</sup> alone could not charge balance. However, attempts to refine the water site as a half occupied nitrogen atom failed. The half occupancy is required, since the multiplicity is two. It is supposed that the water site shares an H<sub>2</sub>O molecule and an H<sub>3</sub>O<sup>+</sup> cation. Hydrogen atoms for the water molecule were located from the difference Fourier map, and a third hydrogen for the hydronium cation was also located and refined with half occupancy. These three hydrogen atoms had their bond lengths and angles fixed manually and their isotropic displacements were

fixed to be the same as their carriers.

Thermogravimetric analysis (TGA) was carried out from room temperature to 600 °C at a rate of 5 °C min<sup>-1</sup> under nitrogen gas.

## 4.2.2 Discussion

### Structure

Sc-1 consists of isolated ScF<sub>6</sub> octahedra, water molecules, H<sub>3</sub>O<sup>+</sup> cations and [C<sub>6</sub>N<sub>2</sub>H<sub>16</sub>]<sup>2+</sup> cations.

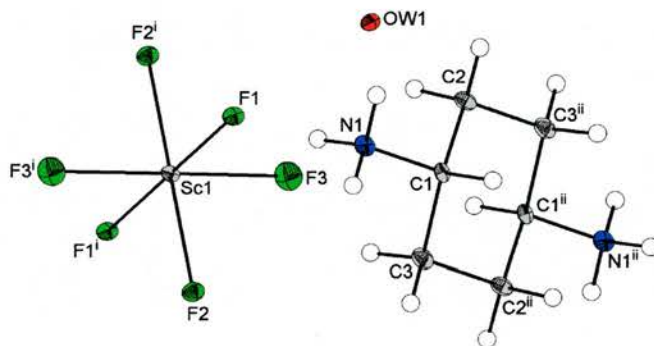


Figure 4.1: An ORTEP diagram of Sc-1 with thermal ellipsoids at 50 % probability (arbitrary spheres for the H atoms) (i) 1-x, -y, 1-z (ii) 1-x, -y, -z.

A hydrogen bonding scheme is shown in Figure 4.2. F1 is hydrogen bonded to two 1,4-diammoniumcyclohexane cations while F2 is hydrogen bonded to one organic cation and a water site, which is shared between a water molecule and a hydronium cation. F3 is only hydrogen bonded to this type of water site. A table of hydrogen bonds is shown in Table 4.3.

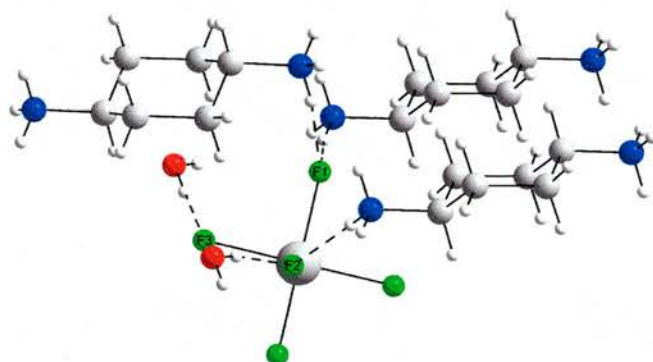


Figure 4.2: The hydrogen bonding scheme of Sc-1 showing water molecules only.

Table 4.3: Hydrogen bonds in Sc-1 (i)  $-x+3/2, y+1/2, -z+1/2$ , (ii)  $-x+3/2, y-1/2, -z+1/2$ , (iii)  $x, y+1, z$ , (iv)  $-x+1/2, y+1/2, -z+1/2$ .

D	H	A	D-H (Å)	H-A (Å)	D-A (Å)	$\angle$ DHA (°)
N1	H1	F2 <sup>i</sup>	0.91	1.92	2.82(1)	167
N1	H2	F1 <sup>ii</sup>	0.91	1.84	2.73(1)	164
N1	H3	F1	0.91	1.86	2.77(1)	170
O1	H9	F2 <sup>iii</sup>	0.84(2)	1.88(2)	2.72(1)	175(5)
O1	H10	F3	0.84(2)	1.86(2)	2.68(1)	169(6)
O1	H11	F3 <sup>iv</sup>	0.85(2)	1.82(3)	2.67(1)	173(9)

Table 4.4 shows the bond valence sums of the three fluorine atoms discussed and the Sc atom. F3 is the most underbonded ligand atom and this is due to the the hydrogen bonding between F3 and the site containing H<sub>2</sub>O and H<sub>3</sub>O<sup>+</sup>. All of the F atoms however, require H-bonds to bring their bond valence sums close to one.

*Table 4.4: Selected bond distances and bond valence sums of Sc-1.*

Bond	Distance (Å)	Atom	$\Sigma s_{ij}$
Sc-F1	2.02(1)	Sc1	2.876
Sc-F2	2.01(1)	F1	0.498
Sc-F3	2.07(1)	F2	0.509
		F3	0.431

Figures 4.3, 4.4 and 4.5 shows the structure of Sc-1 showing only water in the half occupied sites. Other scandium containing structures have are known to have oxonium cations occupying channels, for example in Sc<sub>4</sub>(HPO<sub>4</sub>)<sub>8</sub>.4H<sub>3</sub>O[2] and a range of vanadium phosphonates[3].

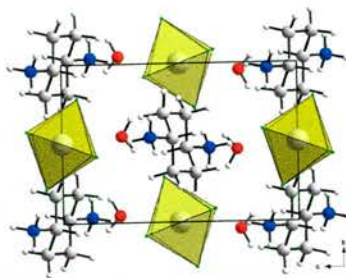


Figure 4.3: Sc-1 along the a-axis.

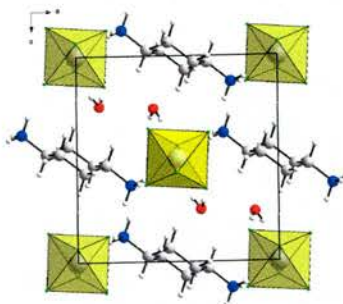


Figure 4.4: Sc-1 along the b-axis.

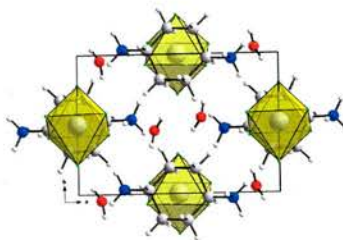


Figure 4.5: Sc-1 along the c-axis.

Other types of structures with isolated  $\text{ScF}_6$  octahedra exist with the  $\text{A}_3\text{ScF}_6$  compounds [4][5][6], where  $\text{A} = \text{NH}_4^+$ ,  $\text{Na}^+$  and  $\text{K}^+$ . These are shown in Figure 4.6. From left to right, the symmetry decreases from  $\text{Fm}\bar{3}\text{m}$  to  $\text{P4/mnc}$  and  $\text{P2}_1/\text{n}$ .

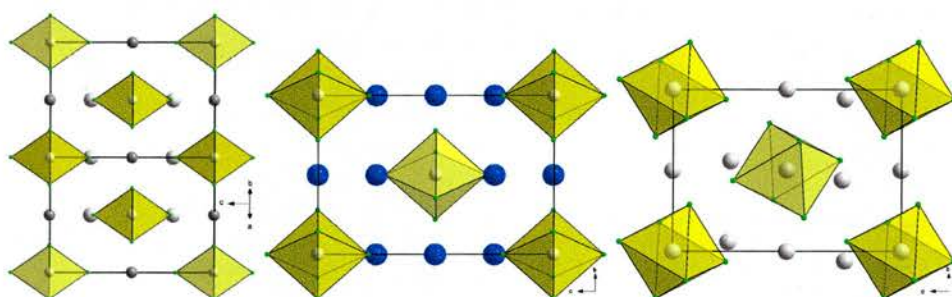


Figure 4.6:  $\text{A}_3\text{ScF}_6$  types from Reber, Bode and Carlson (left to right).

Figure 4.7 shows other isolated types,  $[\text{NH}_3\text{OH}]_2[\text{TiF}_6] \cdot \text{H}_2\text{O}$  [7] and  $[\text{C}_5\text{NH}_{12}\text{O}_2]_2[\text{TaF}_6]$  [8]. These do not have any oxonium cations.

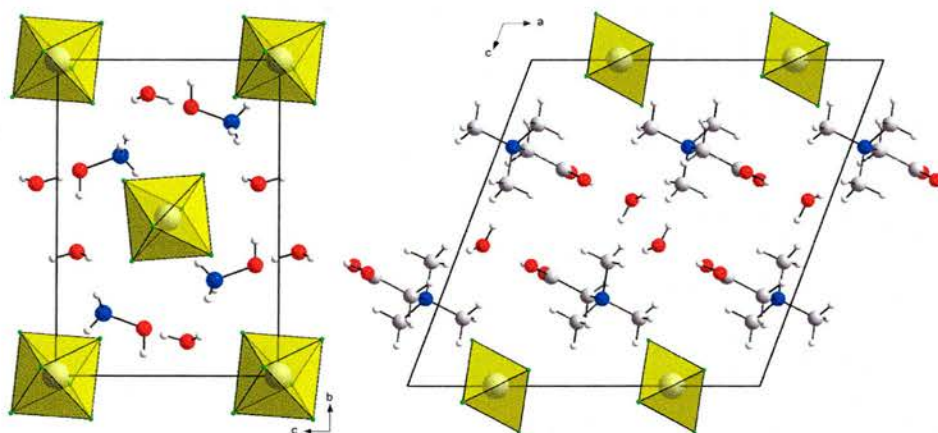


Figure 4.7:  $[\text{NH}_3\text{OH}]_2[\text{TiF}_6] \cdot \text{H}_2\text{O}$  (left) and  $[\text{C}_5\text{NH}_{12}\text{O}_2]_2[\text{TaF}_6]$  (right).

## Thermogravimetric Analysis

The TGA plot of Sc-1 is shown in Figure 4.8.

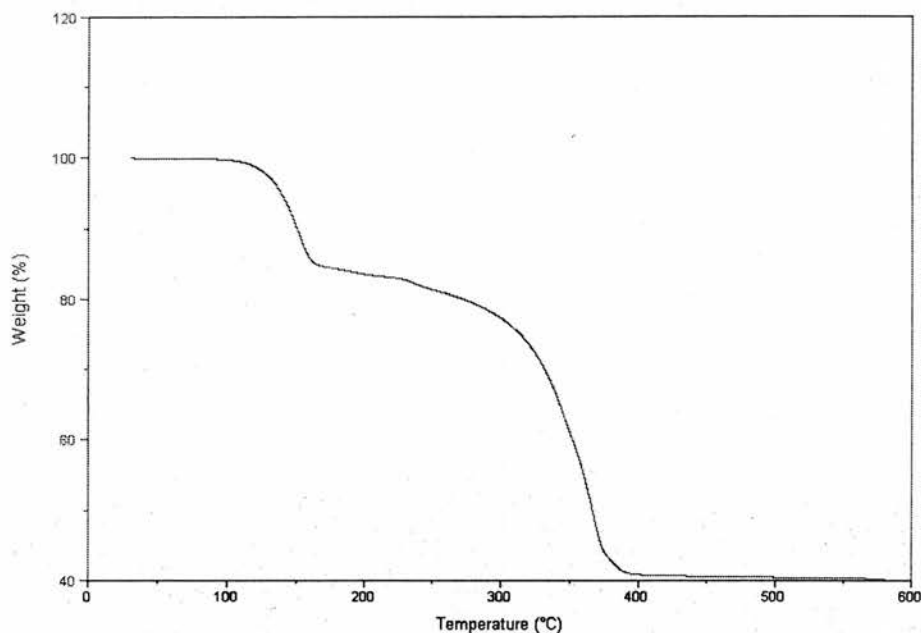


Figure 4.8: A TGA plot of Sc-1.

Under  $N_2$ , the weight loss can be split into two steps. The first step from 131 to 160 °C can be represented by a loss of a single water molecule, the oxonium cation and one  $F^-$  ligand (observed 16 %, calc. 18 %). The second step is a gradual weight loss from the end of the first step up to 313 °C, and a sudden drop in weight up to 377 °C. This can be represented by a loss of two  $F^-$  ligands and the protonated template (observed 56 %, calc. 60 %). The residue was examined by powder diffraction, which confirms  $ScF_3$  (PDF no. 44-1096) as the end product of total decomposition.  $ScF_3$  conforms to the  $ReO_3$  structure, which is a cubic perovskite with the A cation absent.

## 4.3 [C<sub>2</sub>N<sub>2</sub>H<sub>10</sub>][ScF<sub>5</sub>] (Sc-2)

### 4.3.1 Experimental

#### Synthesis

Sc<sub>2</sub>O<sub>3</sub> (0.1379 g, 1 mmol) was placed into a polypropylene bottle with 0.5 ml HF and 5 ml water. This was heated at 100 °C for one hour. The contents of the bottle were transferred to a Teflon lined steel autoclave and any remaining reactants were washed into the autoclave with 5 ml ethylene glycol. Ethylenediamine (0.26 g, 4 mmol) was added to the mixture to give a pH of 3. This was heated for five days at 190 °C. At the end of the reaction the pH was 10.

The thin needle like crystals were filtered, washed in water and dried at room temperature (Found: C, 11.84 %; H, 4.73 %; N, 13.48 %. [C<sub>2</sub>N<sub>2</sub>H<sub>10</sub>][ScF<sub>5</sub>] requires: C, 11.89 %; H, 4.99 %; N, 13.86 %).

#### Characterisation

Thermogravimetric analysis (TGA) was carried out from room temperature to 750 °C, at a heating rate of 5 °C min<sup>-1</sup> under N<sub>2</sub>. The residue was examined with X-ray powder diffraction.

## 4.3.2 Discussion

### Structure

Sc-2 consists of linear chains of *trans* corner-shared  $\text{ScF}_6$  octahedra. One chain is in an eclipsed conformation, and the other is in a staggered conformation.

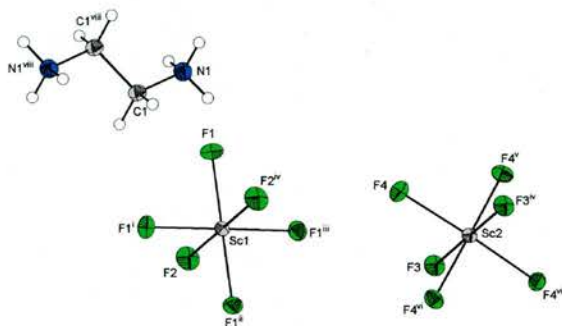


Figure 4.9: An ORTEP diagram of Sc-2 with thermal ellipsoids at 50 % probability (arbitrary spheres for the H atoms) (i)  $1-y, 1-x, 1/2-z$  (ii)  $1/2-x, 1.5-y, z$  (iii)  $-1/2+y, 1/2+x, 1/2-z$  (iv)  $x, 3/2-y, 1/2+x$  (v)  $3/2-y, x, z$  (vi)  $y, 3/2-x, z$  (vii)  $3/2-x, 3/2-y, z$  (viii)  $-x, 3/2-y, -1/2+z$ .

Figure 4.10 shows the unit cell of Sc-2 along the *c*-axis.

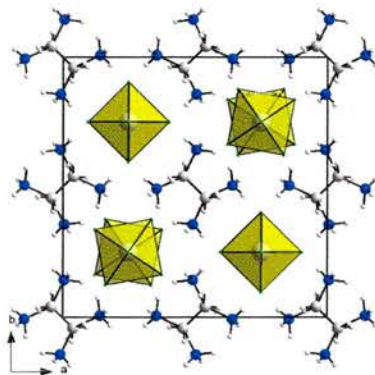


Figure 4.10: The unit cell of Sc-2 along the *c*-axis.

The torsion angle of F4a-Sc2a-Sc2b-F4b formed by two adjacent ScF<sub>6</sub> octahedra in the staggered chain is 21.32 °, as shown in Figure 4.11. CaCrF<sub>5</sub>[9] consists of one crystallographically independent CrF<sub>5</sub> chain made from *trans*-connected CrF<sub>6</sub> octahedra. The torsion angle here is only 9.24 ° and the Cr-F-Cr angle is 143 °. However, the dihedral angle in Sc-2 is not the widest known; [C<sub>6</sub>N<sub>2</sub>H<sub>18</sub>][AlF<sub>5</sub>][10] has a torsion angle of 29 °.

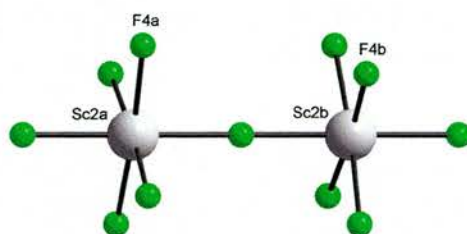


Figure 4.11: A view of part of the staggered chain seen in Sc-2.

Along the same direction as each ScF<sub>5</sub> chain, the ethylene diammonium cations stack in alternating directions. This is shown in Figure 4.12.

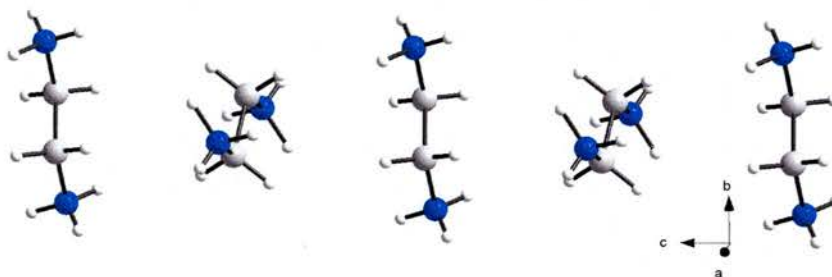


Figure 4.12: The stacking of ethylenediammonium cations.

Shown in Figure 4.13 is the hydrogen bonding scheme around two ethylenediammonium cations. Each one links two eclipsed and two staggered chains together. Both orientations of the ethylenediammonium cations are shown.

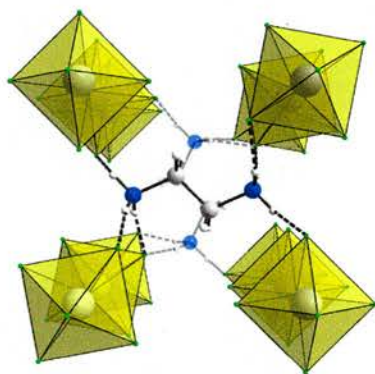


Figure 4.13: A perspective view of the hydrogen bonding seen in Sc-2.

Table 4.5 shows three unique hydrogen bonds in Sc-2.

Table 4.5: Selected hydrogen bonding of Sc-2 (i)  $-y+1, x+1/2, -z+1$ , (ii)  $x-1/2, -y+2, -z+1/2$ .

D	H	A	D-H (Å)	H...A (Å)	D...A (Å)	∠DHA
N1	H1	F1	0.91	2.02	2.66(1)	126
N1	H2	F4 <sup>i</sup>	0.91	1.89	2.79(1)	172
N1	H3	F4 <sup>ii</sup>	0.91	1.84	2.71(1)	159

Table 4.6 shows bond distances and valence sums in Sc-2. F2 and F3 correspond to the F atoms involved in linking the ScF<sub>6</sub> octahedra together. The underbonding of F1 and F4 require H-bonds from the organic cations.

Table 4.6: Bond distances and valence sums in Sc-2 (*i*)  $x, 3/2-y, 1/2+z$ .

Bond	Distance (Å)	Atom	$\Sigma s_{ij}$
Sc1-F1	2.00(1)	Sc1	3.048
Sc1-F2	2.04(1)	Sc2	3.018
Sc2-F3	2.05(1)	F1	0.524
Sc2-F3 <sup><i>i</i></sup>	2.02(1)	F2	0.952
Sc2-F4	2.00(1)	F3	0.95
		F4	0.517

Other infinite chain structures exist. [C<sub>2</sub>N<sub>2</sub>H<sub>10</sub>][MnF<sub>5</sub>][11] consists of Jahn-Teller distorted MnF<sub>6</sub> octahedra, which are *trans* connected to form [MnF<sub>5</sub>]<sup>2-</sup> chains. Figure 4.14 shows the structure of [C<sub>2</sub>N<sub>2</sub>H<sub>10</sub>][MnF<sub>5</sub>] along the *c*-axis.

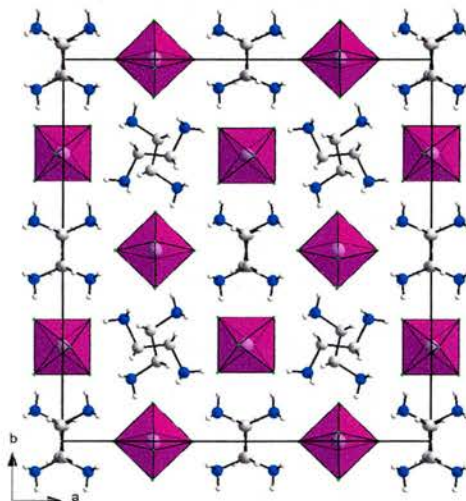


Figure 4.14: [C<sub>2</sub>N<sub>2</sub>H<sub>10</sub>][MnF<sub>5</sub>] along the *c*-axis

As shown in Figure 4.15, the two types of  $\text{MnF}_5$  chains have different Mn-F-Mn angles. In chain A, the angle is  $161^\circ$ , while in chain B, the angle is  $158^\circ$ .

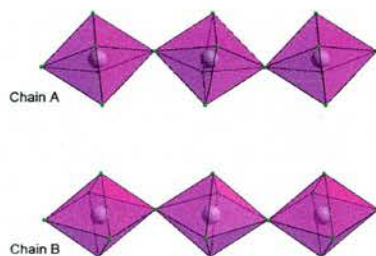


Figure 4.15: The  $\text{MnF}_5$  chains in  $[\text{C}_2\text{N}_2\text{H}_{10}][\text{MnF}_5]$ .

The unit cell parameters of Sc-2 and  $[\text{C}_2\text{N}_2\text{H}_{10}][\text{MnF}_5]$  are shown in Table 4.7. It appears that Sc-2 is a pseudo  $\sqrt{2}$  distortion of  $[\text{C}_2\text{N}_2\text{H}_{10}][\text{MnF}_5]$ .

Table 4.7: Selected crystal parameters for Sc-2 and  $[\text{C}_2\text{N}_2\text{H}_{10}][\text{MnF}_5]$ ,

	Sc-2	$[\text{C}_2\text{N}_2\text{H}_{10}][\text{MnF}_5]$
Crystal system	Tetragonal	Orthorhombic
Space group	P4/ncc	Cccm
a(Å)	13.055(2)	17.105(4)
b(Å)		17.992(4)
c(Å)	8.142(2)	8.478(2)
Cell Volume(Å <sup>3</sup> )	1383.4(5)	2609(10)

$(\text{NH}_4)_2\text{MnF}_5$ [12] consists of  $\text{MnF}_6$  octahedra, which are also *trans*-connected but the chains are eclipsed.  $\text{Rb}_2\text{MnF}_5$ [13] has *trans*-connected  $\text{MnF}_6$  octahedra forming eclipsed linear chains. Both of these examples have M-F-M angles of  $180^\circ$ , identical to Sc-2. Sc-2 is the first example of eclipsed and staggered chains present in this structure type.

$\text{Tl}_2\text{AlF}_5$ [14] is composed of linear chains of  $\text{AlF}_6$  octahedra, which are *trans*-connected by an Al-F-Al angle of  $160^\circ$ .

### Thermogravimetric Analysis

The TGA plot of Sc-2 is shown in Figure 4.16.

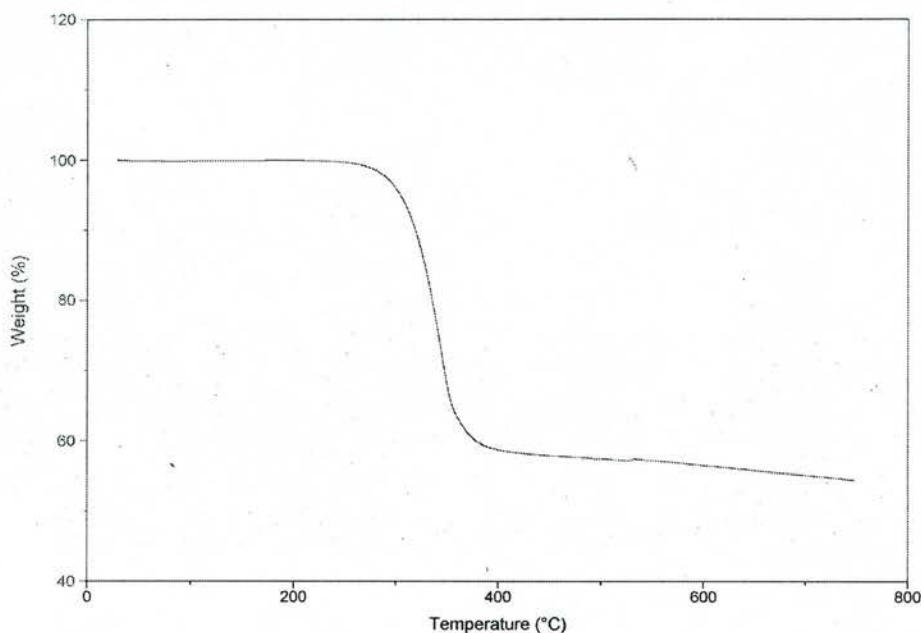
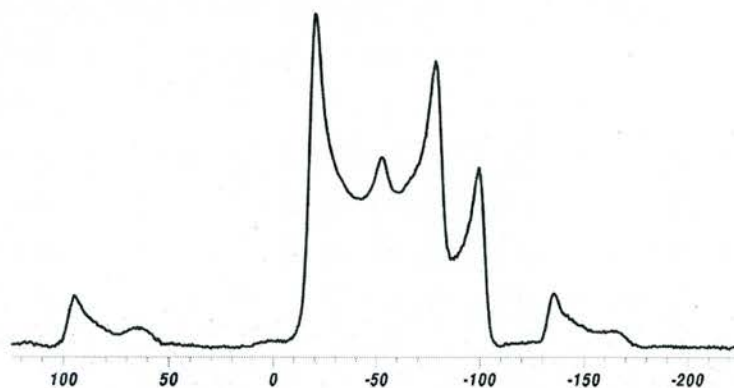


Figure 4.16: TGA plot of Sc-2.

Under  $\text{N}_2$ , a single weight loss occurs from 250 to 400 °C. This is due to the loss of ethylenediammonium cations and two  $\text{F}^-$  ligands, causing the structure to condense to  $\text{ScF}_3$  (observed 42.8 %, calculated 50.5 %). A powder X-ray diffraction pattern of the residue was taken to reveal that the only decomposition product is  $\text{ScF}_3$  (PDF no. 44-1096).

## MAS NMR

$^{45}\text{Sc}$  MAS NMR shows two peaks at -55 ppm and -80 ppm.  $^{45}\text{Sc}$  is a quadrupolar nucleus, and each peak is split into two. This is consistent with two crystallographic Sc sites. The identities of the two pairs of peaks at 75 ppm and -150 ppm are unclear.



*Figure 4.17: The MAS-NMR spectrum of Sc-2.*

## 4.4 $\text{NH}_4\text{ScF}_4$ (Sc-3)

### 4.4.1 Experimental

#### Synthesis

0.138 g of  $\text{Sc}_2\text{O}_3$ , 5 ml of water and 0.5 ml of a 40 % solution of HF was heated in a Teflon lined steel autoclave for one hour at 190 °C. To this, 5 ml of ethylene glycol and 0.4 ml 1,3-propylenediamine was added and heated at the same temperature for four days. The colourless prismatic crystals were washed in water and allowed to dry at room temperature overnight (Found: H, 2.02 %; N, 7.28 %,  $\text{NH}_4\text{ScF}_4$  requires H, 2.90 %; N, 10.08 %). The difference between the expected values and the experimental values suggest an impurity in the sample. Powder X-ray diffraction shows that this impurity is  $\text{ScF}_3$  (PDF no.44-1096).

Hydrogen atoms for the  $\text{NH}_4^+$  cations were located from the difference Fourier map, and could be refined successfully without the need to fix the bond distances and the tetrahedral angles.

Thermogravimetric analysis was carried out from room temperature to 800 °C, at a heating rate of 5 °C  $\text{min}^{-1}$  under  $\text{N}_2$ .

## 4.4.2 Discussion

### Structure

Sc-3 consists of a 2-dimensional array of corner sharing  $\text{ScF}_6$  octahedra, which produces sheets stacked along the c-axis. The building unit is shown in Figure 4.18.

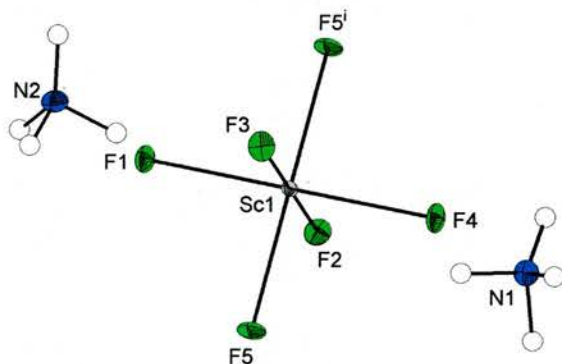


Figure 4.18: An ORTEP diagram of Sc-3 with thermal ellipsoids at 50 % probability (arbitrary spheres for the H atoms) ( $i$ )  $-x, 1/2+y, 1/2-z$ .

Figure 4.19 shows the stacking of the  $[\text{ScF}_4]^-$  sheets compared to  $\text{KScF}_4$ .

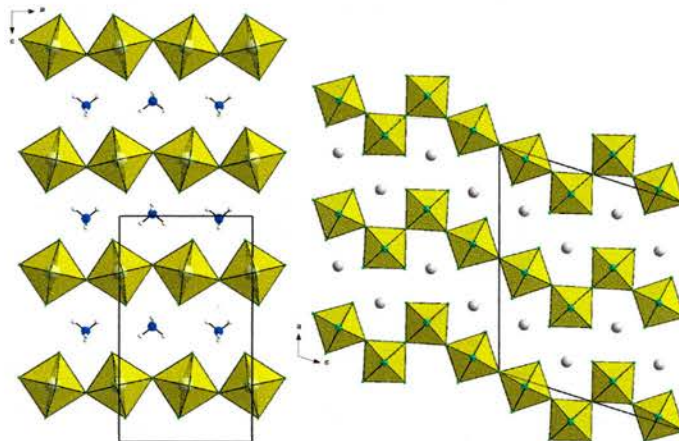
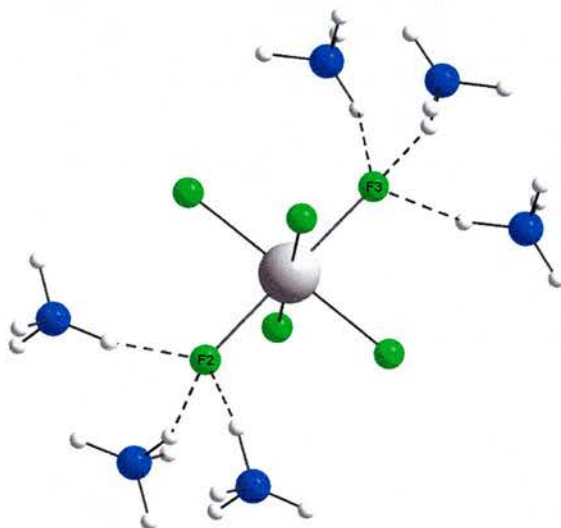


Figure 4.19: The layering topology of Sc-3 (left) compared to  $\text{KScF}_4$  (right).

Sc-3 is an example of a Dion-Jacobson phase[15][16]. These consist of perovskite-like blocks separated from each other by a single layer of alkali metal cations. The only difference between Sc-3 and typical Dion-Jacobson phases is the single two-dimensional sheets rather than perovskite blocks, which are separated by interlayer ammonium cations. Since ammonium cations and  $K^+$  cations are of similar size, it is expected that  $KScF_4$ [17] would be isostructural. It is not however, because the sheets are stepped in  $KScF_4$ .

A hydrogen bonding scheme is shown in Figure 4.20. The ammonium cations hydrogen bond to F2 and F3, which are the F atoms that point in between each  $[ScF_4]^-$  sheet.



*Figure 4.20: The hydrogen bonding scheme of Sc-3.*

Table 4.8 shows the hydrogen bonding around the  $\text{ScF}_6$  octahedron. F1, F4 and F5 are involved in linking the  $\text{ScF}_6$  octahedra into the  $[\text{ScF}_4]^-$  sheets. The  $\text{NH}_4^+$  cations interact with F2 and F3, which protrude into the inter-layer space. Table 4.9 shows the bond distances and valences.

Table 4.8: Selected hydrogen bonding of Sc-3 (i)  $x, -y+3/2, z-1/2$ , (ii)  $x+1/2, -y+2, -z$ , (iii)  $-x, -y+2, -z+1$ , (iv)  $-x-1/2, y, z$ , (v)  $-x-1/2, -y+3/2, z+1/2$ .

D	H	A	D-H	H...A	D...A	$\angle$ DHA
N1	H1	F2	0.91(3)	1.97(3)	2.84(1)	158(2)
N1	H1	F4	0.91(3)	2.59(2)	3.07(1)	114(2)
N1	H2	F3 <sup>i</sup>	0.95(4)	2.13(3)	2.86(1)	133(1)
N1	H3	F2 <sup>ii</sup>	0.92(5)	2.17(4)	2.85(1)	129(2)
N2	H4	F3 <sup>iii</sup>	0.89(5)	2.21(4)	2.86(1)	130(2)
N2	H5	F3 <sup>iv</sup>	0.93(3)	1.96(3)	2.84(1)	158(2)
N2	H6	F2 <sup>v</sup>	0.96(4)	2.13(2)	2.88(1)	133(1)

The bond valence sums show that F2 and F3 are underbonded, so these require hydrogen bonding from the ammonium cations.

Table 4.9: Bond distances and valence sums of Sc-3.

Bond	Distance ( $\text{\AA}$ )	Atom	$\Sigma s_{ij}$
Sc1-F1	2.03(1)	Sc1	3.001
Sc1-F2	1.99(1)	F1	0.972
Sc1-F3	1.99(1)	F2	0.537
Sc1-F4	2.03(1)	F3	0.534
Sc1-F5	2.03(1)	F4	0.972
		F5	0.958

Sc-3 is very similar to  $\text{NH}_4\text{FeF}_4$  [18]. This is shown in Figure 4.21 along side Sc-3. The  $[\text{MF}_4]^-$  sheets of Sc-3 are staggered, while the  $[\text{MF}_4]^-$  sheets of  $\text{NH}_4\text{FeF}_4$  are not. These two structures are interrelated by their crystal parameters, which are shown in Table 4.10.

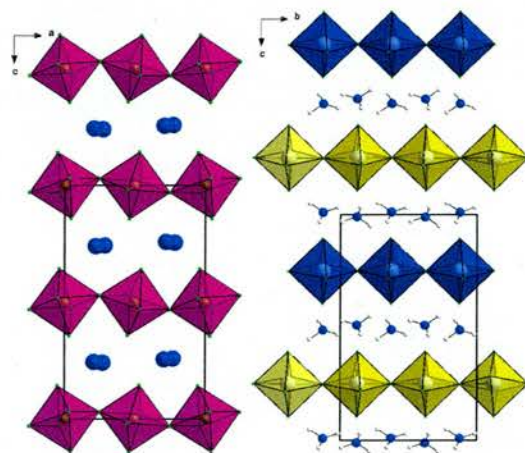


Figure 4.21:  $\text{NH}_4\text{FeF}_4$  (left) and Sc-3 (right).

The difference in parameters and space group, between  $\text{NH}_4\text{FeF}_4$  and Sc-3 allows the sheets to be displaced.

Table 4.10: Selected crystal parameters for  $\text{NH}_4\text{FeF}_4$  and Sc-3.

	$\text{NH}_4\text{FeF}_4$	Sc-3
Crystal system	Orthorhombic	Orthorhombic
Space group	Pnma	Pmcn
a(Å)	7.559(4)	7.862(2)
b(Å)	7.575(4)	8.088(2)
c(Å)	12.754(8)	13.503(4)

$\text{KCeF}_4$  [19] has a similar layering scheme, except with  $\text{CeF}_9$  double-capped square antiprisms.  $\text{NH}_4\text{BF}_4$  [20] conforms to the same formula type, but it

consists of isolated  $\text{BF}_4$  tetrahedra. A higher symmetry version of the Dion-Jacobson structure is  $\text{KFeF}_4$  [21], which is in the space group  $\text{Cmcn}$  and has comparable lattice parameters to Sc-3 but with the a-axis halved and the b- and c-axes exchanged.

### Thermogravimetric Analysis

The TGA plot of Sc-3 is shown in Figure 4.22.

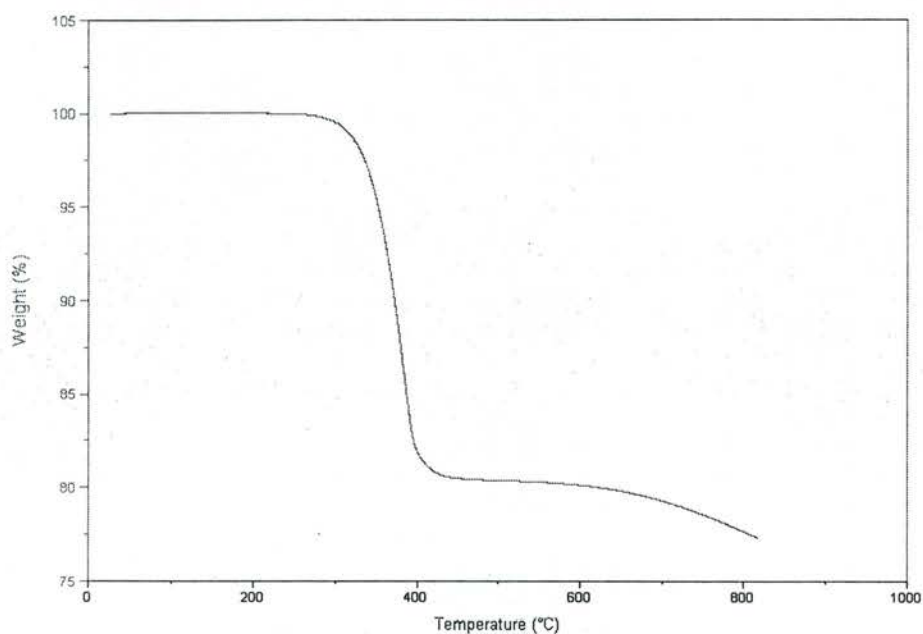


Figure 4.22: The TGA plot of Sc-3.

Under  $\text{N}_2$ , a single step weight loss occurs from 300 to 425 °C. This can be represented by the loss of ammonium cations and one  $\text{F}^-$  ligand (observed 19.6 %, calc. 20 %). Powder X-ray diffraction was carried out on the residue, which proves that the decomposition product is  $\text{ScF}_3$  (PDF no. 44-1096).

## 4.5 $[\text{C}_2\text{N}_2\text{H}_{10}]_{0.5}[\text{ScF}_4]$ (Sc-4)

### 4.5.1 Experimental

#### Synthesis

$[\text{C}_2\text{N}_2\text{H}_{10}]_{0.5}[\text{ScF}_4]$  (Sc-4) was formed hydrothermally by heating a mixture of  $\text{Sc}_2\text{O}_3$  (0.1379 g, 1 mmol), 0.5 ml HF and 5 ml water in a polypropylene bottle at 100 °C for one hour. The mixture was then placed in a Teflon lined steel autoclave. Any remaining contents of the bottle were washed into the autoclave with 5 ml ethylene glycol. 0.5 ml ethylenediamine was added to the reaction mixture and the pH was 10. The mixture was heated at 190 °C for 5 days. The resulting needle like crystals were washed and filtered. Earlier experiments were carried out with 0.1046 g  $\text{GeO}_2$  and 0.258 g piperazine. Although larger prismatic rod like crystals were formed, neither  $\text{GeO}_2$  nor piperazine was found in the product (Found: C, 7.90 %; H, 3.32 %; N, 9.21 %.  $[\text{C}_2\text{N}_2\text{H}_{10}]_{0.5}[\text{ScF}_4]$  requires C, 7.57 %; H, 3.01 %; N, 8.92 %).

#### Characterisation

Thermogravimetric analysis was carried out from room temperature to 750 °C, with a heating rate of 5 °C  $\text{min}^{-1}$  under  $\text{N}_2$ .

## 4.5.2 Discussion

### Structure

Sc-4 is a two dimensional layer structure constructed from  $\text{ScF}_6$  octahedra and ethylenediammonium cations. Figure 4.23 shows the building unit.

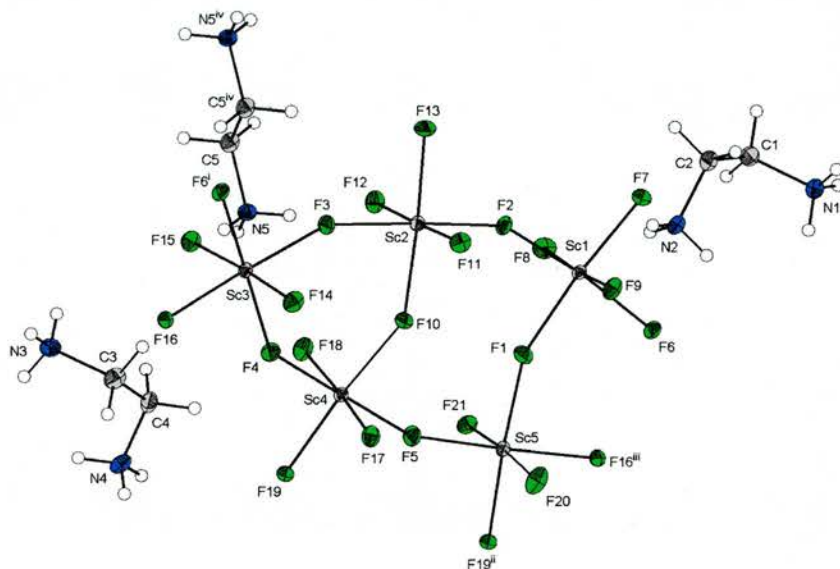


Figure 4.23: An ORTEP diagram of Sc-4 at 50 % probability (arbitrary spheres for the H atoms). (i)  $-1+x, 1+y, z$  (ii)  $-x, -y, 1-z$  (iii)  $1+x, -1+y, z$  (iv)  $-1-x, 1-y, -z$ .

The structure consists of  $[\text{ScF}_4]^-$  sheets of corner sharing  $\text{ScF}_6$  octahedra. The sheets are separated by the ethylenediammonium cations *via* hydrogen bonding, by a distance of 8.9 Å. From the TGA data, the ethylenediammonium cations are burned off and the sheets condense without preserving their topologies. A decomposition to  $\text{ScF}_3$  occurs (PDF No. 44-1096).

The sheets are composed of “bow-tie” units, shown in Figure 4.24. They are made up of five crystallographically independent  $\text{ScF}_6$  corner sharing octahedra.

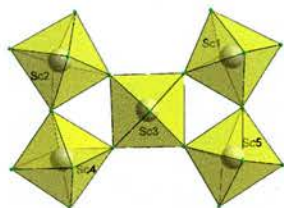


Figure 4.24: The “bow-tie” unit found in Sc-4.

A single  $[\text{ScF}_4]^-$  sheet is shown in Figure 4.25, with the hexagonal tungsten bronze (HTB)  $\text{WO}_3$ . Each  $[\text{ScF}_4]^-$  sheet eclipses another exactly.

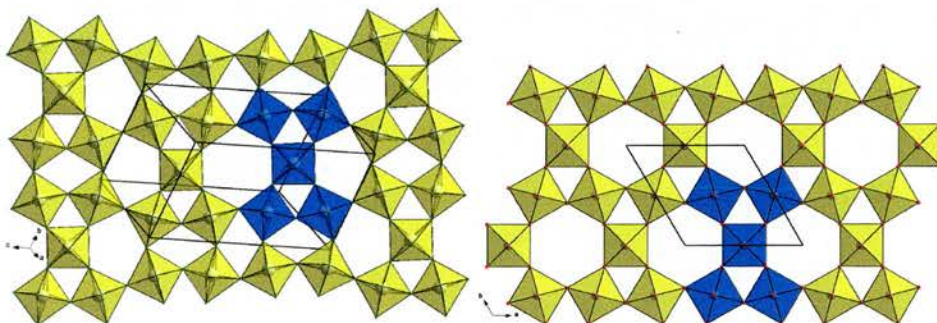


Figure 4.25: Sc-4 (left) and  $\text{WO}_3$  along the c-axis (right).

The building unit of Sc-4 is arranged not unlike that seen in the HTBs. In HTB, the building unit shown in blue is arranged in a linear fashion to produce a structure with 3- and 6-membered rings. In Sc-4, the building units are arranged in a more complex way to form 3-, 4-, 5-, and 6-membered rings.

Figure 4.26 shows how two  $[\text{ScF}_4]^-$  sheets are hydrogen bonded by a layer of ethylenediammonium cations.

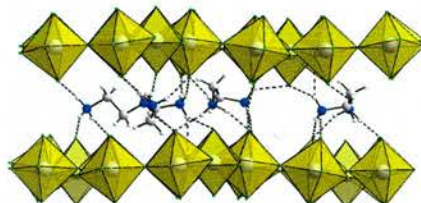


Figure 4.26: Two  $[\text{ScF}_4]^-$  sheets and one layer of ethylenediammonium cations.

Table 4.11: Hydrogen bonds in Sc-4 (i)  $x+1, y, z$  (ii)  $x+1, y+1, z$  (iii)  $x, y+1, z$  (iv)  $x-1, y+1, z$  (v)  $x-1, y, z$  (vi)  $-x, -y, -z+1$  (vii)  $-x-1, -y+1, -z+1$ .

D	H	A	D-H (Å)	H...A (Å)	D...A (Å)	$\angle\text{DHA}$
N1	H1	F11 <sup>i</sup>	0.890	2.129	2.76(1)	128
N1	H2	F21 <sup>ii</sup>	0.890	1.939	2.76(1)	152
N1	H3	F8 <sup>ii</sup>	0.890	1.729	2.61(1)	168
N2	H4	F18 <sup>ii</sup>	0.890	1.769	2.64(1)	167
N2	H5	F21 <sup>ii</sup>	0.890	1.908	2.77(1)	163
N2	H6	F14 <sup>i</sup>	0.890	2.250	2.84(1)	124
N2	H6	F6 <sup>iii</sup>	0.890	2.393	3.20(1)	152
N3	H11	F21 <sup>iv</sup>	0.890	2.017	2.82(1)	150
N3	H12	F17 <sup>v</sup>	0.890	1.964	2.80(1)	155
N3	H13	F11 <sup>v</sup>	0.890	1.901	2.77(1)	166
N4	H16	F20 <sup>v</sup>	0.890	1.776	2.61(1)	155
N4	16	F20 <sup>vi</sup>	0.890	2.330	2.83(1)	116
N4	H17	F17 <sup>v</sup>	0.890	1.828	2.71(1)	169
N4	H18	F16 <sup>vii</sup>	0.890	2.185	3.02(1)	156
N4	H18	F14 <sup>vii</sup>	0.890	2.324	2.94(1)	126
N5	H21	F9 <sup>v</sup>	0.890	1.872	2.75(1)	168
N5	H22	F15	0.890	1.853	2.70(1)	159
N5	H23	F12	0.890	1.812	2.68(1)	166

Bond distances are shown in Table 4.12 and bond valence sums are shown in Table 4.13.

Table 4.12: Bond distances in Sc-4 (i)  $x-1, y+1, z$ , (ii)  $-x, -y, -z+1$ , (iii)  $x+1, y-1, z$ .

Bond	Length (Å)	Bond	Length (Å)	Bond	Length (Å)
Sc1-F1	2.05(1)	Sc2-F12	1.97(1)	Sc4-F10	2.04(1)
Sc1-F2	2.05(1)	Sc2-F13	2.03(1)	Sc4-F17	2.02(1)
Sc1-F6	2.06(1)	Sc3-F3	2.03(1)	Sc4-F18	1.95(1)
Sc1-F7	2.03(1)	Sc3-F4	2.03(1)	Sc4-F19	2.02(1)
Sc1-F8	1.97(1)	Sc3-F6 <sup>i</sup>	2.04(1)	Sc5-F1	2.03(1)
Sc1-F9	1.97(1)	Sc3-F14	1.97(1)	Sc5-F5	2.03(1)
Sc2-F2	2.03(1)	Sc3-F15	1.98(1)	Sc5-F16 <sup>iii</sup>	2.05(1)
Sc2-F3	2.06(1)	Sc3-F16	2.05(1)	Sc5-F19 <sup>ii</sup>	2.04(1)
Sc2-F10	2.04(1)	Sc4-F4	2.03(1)	Sc5-F20	1.94(1)
Sc2-F11	2.01(1)	Sc4-F5	2.04(1)	Sc5-F21	2.02(1)

The underbonded F atoms shown in the following table require hydrogen bonding from the organic template cations.

Table 4.13: Bond valence sums in Sc-4

Atom	$\sigma_{s_{ij}}$	Atom	$\sigma_{s_{ij}}$	Atom	$\sigma_{s_{ij}}$	Atom	$\sigma_{s_{ij}}$
Sc1	2.98	F3	0.93	F10	0.94	F17	0.50
Sc2	2.98	F4	0.95	F11	0.51	F18	0.59
Sc3	2.99	F5	0.95	F12	0.58	F19	0.96
Sc4	3.00	F6	0.94	F13	0.96	F20	0.61
Sc5	3.01	F7	0.96	F14	0.56	F21	0.50
F1	0.95	F8	0.56	F15	0.55		
F2	0.95	F9	0.57	F16	0.92		

Other variations of the HTB structure can be seen in  $\text{Na}_5\text{W}_{14}\text{O}_{44}$  by Christidis shown in Figure 4.27 [22]. The layers are displaced relative to each other, so that no channels are formed.

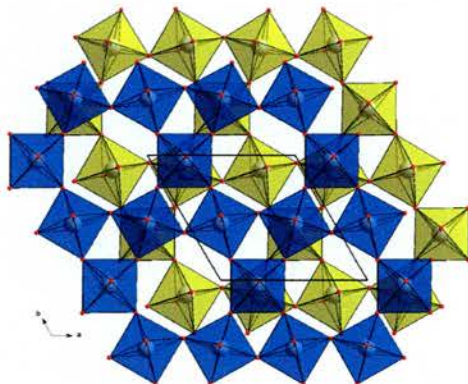


Figure 4.27: The staggered nature of the sheets in  $\text{Na}_5\text{W}_{14}\text{O}_{44}$ .

Another example is the niobium substituted HTB by Hussain *et al* [23], which have the general composition  $\text{M}_x\text{Nb}_y\text{W}_{1-y}\text{O}_3$ , where  $x = 0.2, 0.25, 0.3$  and  $0 \leq y \leq 0.2$ .

The layering of Sc-4 is reminiscent of the Ruddlesden-Popper and the Dion-Jacobson phases,  $\text{K}_2\text{NiF}_4$  and Sc-3 respectively. These consist of  $[\text{MF}_4]^-$  sheets of corner-sharing  $\text{MF}_6$  octahedra and only have 4-membered rings. Metal-organic hybrids of these structures have been developed by Mitzi [24]. These bismuth and antimony halides consist of distorted octahedra sharing edges and corners to form sheets separated by organic cations.

Other HTB structures exhibit a similar layering scheme to Sc-4. Figure 4.28 shows  $K(\text{VO}_2)_3(\text{SeO}_3)_2$  by Harrison *et al* [25], which has layers of  $\text{VO}_6$  octahedra arranged in the “bow-tie” unit, which are capped by selenium atoms.

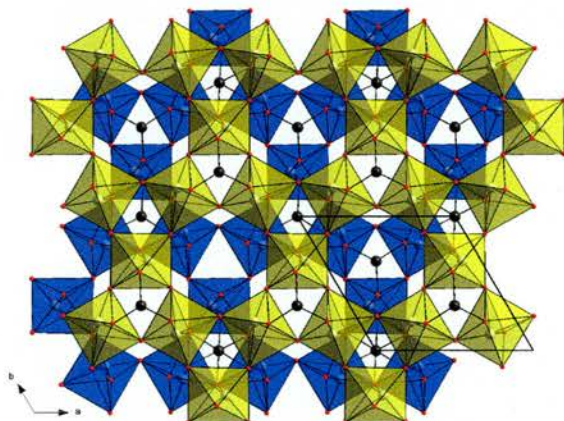


Figure 4.28: The layering scheme in  $K(\text{VO}_2)_3(\text{SeO}_3)_2$ .

Other species can cap these HTB layers, including  $\text{PO}_3\text{CH}_3^{3-}$  [26] where each  $\text{WO}_6$  octahedron shows displacement of the W atom from the centre of the octahedron towards the O atom in between the layers. This displacement along the c-axis and the acentric space group R3, will allow the material to exhibit all of the non-linear properties discussed in Table 1.1 in Chapter 1. However, the authors did not investigate this. A similar situation occurs with the Mo analogue [27], except the displacement of the Mo atom in the  $\text{MoO}_6$  octahedron is towards three O atoms. Phosphate groups cap HTB layers [28] resulting in a centrosymmetric arrangement of the layers, due to hydrogen bonding.

Sc-4 is the first organically templated structure to show a mixture of the HTB and TTB sheet topologies. Other organically templated scandium containing materials already exist, but they are limited to phosphates so far[29].

### Thermogravimetric Analysis

Figure 4.29 shows the TGA plot of Sc-4.

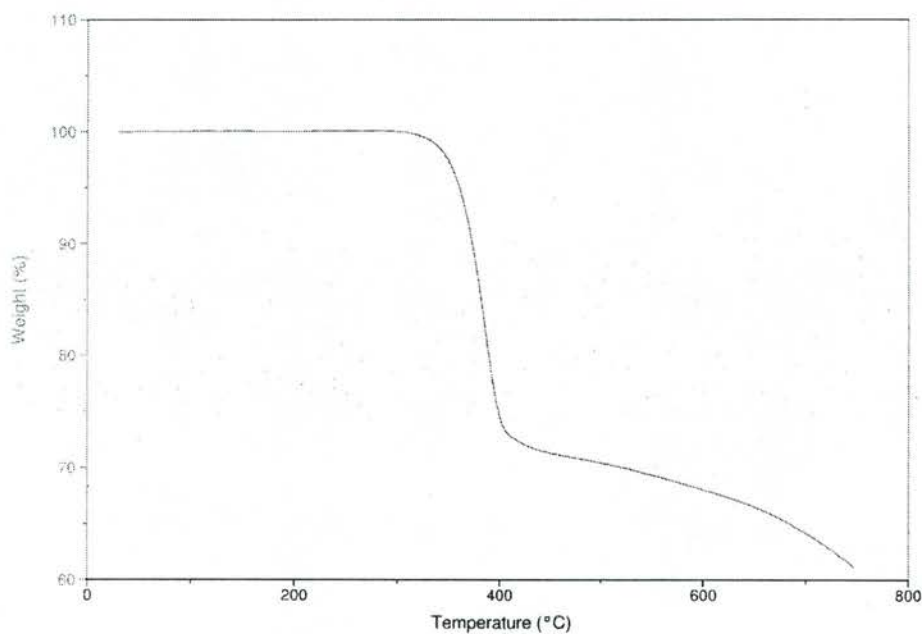


Figure 4.29: A TGA plot of Sc-4.

Under  $N_2$ , a single step weight loss occurs from 300 to 400 °C. This is due to a loss of ethylenediammonium cations and a single  $F^-$  ligand (observed 28.9 %, calc. 30 %). Powder X-ray diffraction of the residue proves that the decomposition to  $ScF_3$  (PDF no. 44-1096) takes place.

## SEM

A micrograph of the compound at 10,000 X magnification is shown in Figure 4.30. EDX microanalysis showed a Sc:F ratio of 1:4. This shows that no germanium is within the structure.



Figure 4.30: An SEM micrograph of a single crystal of Sc-4.

An average atomic percentage (Table 4.14) show a Sc:F ratio of 1:4. The quantity of Ge present is far less than that of Sc.

Table 4.14: Elemental analysis of Sc-4.

Spectrum	Atomic %		
	1	2	Mean
F	80.8	83.9	82.4
Ge	0.3	0.3	0.3
Sc	18.8	15.8	17.3

Figure 4.31 shows an elemental analysis of two single spots of the sample. A third spot showed atomic percentages of F 45.8 %, Ge 0.11 % and Sc 54.1 %. This spurious result may be due to an impurity of  $\text{ScF}_3$  powder and  $\text{Sc}_2\text{O}_3$ , one of the starting materials.

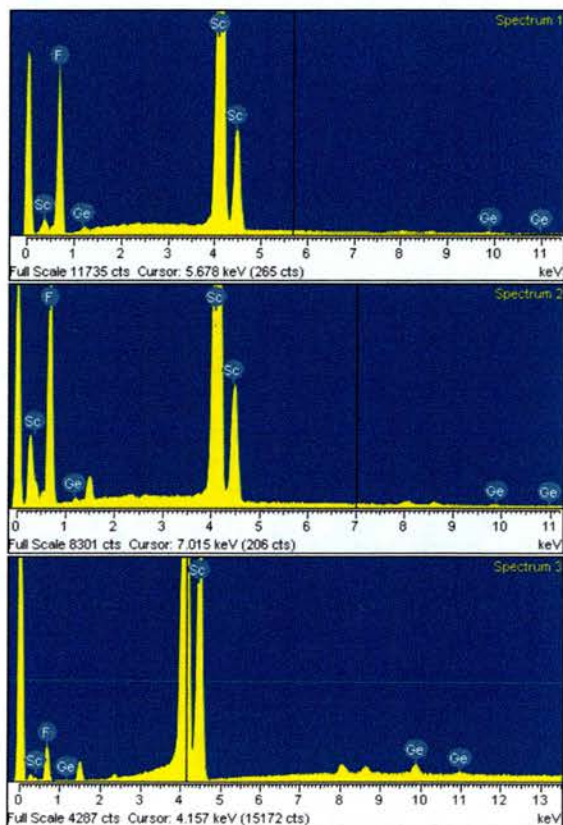


Figure 4.31: An elemental analysis of Sc-4 (spectrum 1 top, spectrum 3 bottom).

## 4.6 $(\text{NH}_4)_2\text{Sc}_3\text{F}_{11}$ (Sc-5)

### 4.6.1 Experimental

#### Synthesis

$\text{Sc}_2\text{O}_3$  (0.1379 g) was placed into a polypropylene bottle with 0.5 ml HF and 5 ml water. This was heated at 100 °C for one hour. The contents of the bottle were transferred to a Teflon lined steel autoclave and any remaining reactants were washed into the autoclave with 5 ml ethylene glycol. 0.5 ml of tris(2-aminoethyl)amine (tren) was added to the mixture to give a pH of 4. This was heated for five days at 180 °C, and the pH of the solution increased to 10. The product was filtered, washed in water and dried at room temperature to give hexagonal plate-like crystals (Found: H, 1.93 %; 7.23 %,  $(\text{NH}_4)_2\text{Sc}_3\text{F}_{11}$  requires: H, 2.12 %; N, 7.37 %).

#### Characterisation

The hydrogen atoms of the  $\text{NH}_4^+$  cations were located from the Fourier map and their bond lengths and angles were fixed to be as tetrahedral as possible. Each  $U_{iso}(\text{H})$  was fixed to be 1.5 times that of its carrier atom. Previous anisotropic refinement showed that the displacements of two fluorine atoms were elongated along the c-axis and the a-axis. They were disordered over two locations, so they were moved off their positions by 0.3 Å along these axes.

Thermogravimetric analysis was carried out from room temperature to 750 °C, with a heating rate of 5 °C  $\text{min}^{-1}$  under an atmosphere of  $\text{N}_2$ .

## 4.6.2 Discussion

### Structure

Sc-5 is a three dimensional scandium fluoride, which consists of  $\text{ScF}_6$  octahedra and  $\text{ScF}_7$  pentagonal bipyramids. The building unit is shown in Figure 4.32.

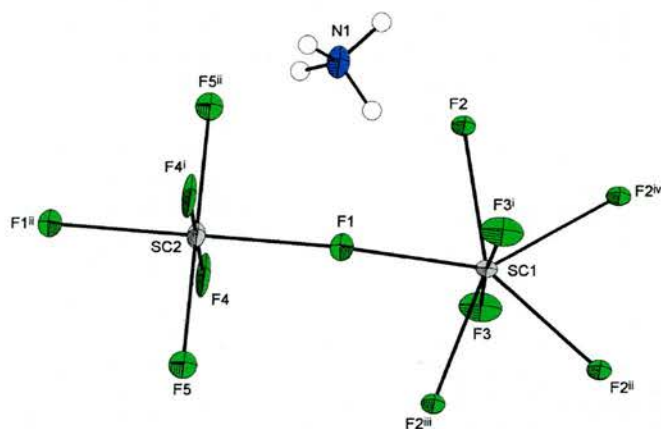
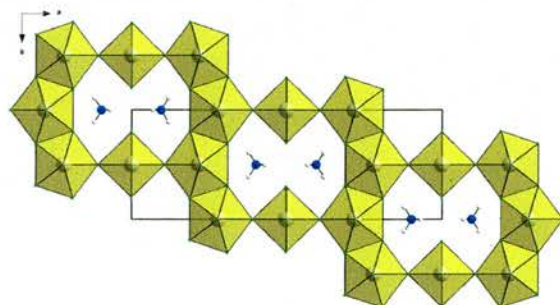


Figure 4.32: An ORTEP diagram of Sc-5 with thermal ellipsoids at 50 % probability (arbitrary spheres for the H atoms) (i)  $x, y, 1+z$  (ii)  $x, y, -z$  (iii)  $x, -y, -z$  (iv)  $1/2-x, 1/2-y, -z$ .

Considering that tren was used as the template in the reaction, the presence of ammonium cations in the X-ray structure shows that some organic templates can decompose in hydrothermal conditions. Similar experiments were carried out with 1,1,3,3-tetramethyl guanidine and the same effect occurred. The disorder of the F atoms is caused by the tilting of the  $\text{ScF}_6$  octahedra.

The structure is composed of sheets of  $\text{ScF}_7$  pentagonal bipyramids, which edge and corner share with each other in a herringbone pattern. These

sheets are linked by  $\text{ScF}_6$  octahedra to form the 3-dimensional structure. This linking forms ten-membered “butterfly” ring channels, which run along the  $c$ -axis (Figure 4.33).



*Figure 4.33: Sc-5 along the  $c$ -axis.*

Within the channels lie the ammonium cations. The hydrogen atoms of the ammonium cations hydrogen bond to the fluorine atoms. This is shown in more detail in Figure 4.34.

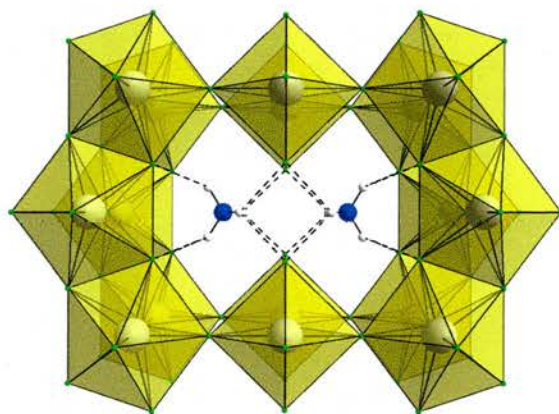


*Figure 4.34: A perspective view of the hydrogen bonding within one “butterfly” channel along the  $c$ -axis.*

Table 4.15 shows the hydrogen bonding in the “idealised” structure, without the disorder taken into account.

Table 4.15: A table of idealised hydrogen bonds in Sc-5 (i)  $-x, -y, z-1$ , (ii)  $x, -y+1, -z-1$ .

D	H	A	D-H	H...A	D...A	$\angle$ DHA
N1	H1	F5 <sup>i</sup>	0.85(2)	2.27(2)	3.00(1)	144(1)
N1	H2	F2 <sup>ii</sup>	0.85(2)	2.43(2)	2.94(1)	119(3)

Table 4.16 shows the valence sums of each atom in the ScF<sub>6</sub> octahedra and the ScF<sub>7</sub> pentagonal bipyramids, if the disorder was not accounted for. The bond valence sums shows that F2 and F5 require hydrogen bonding from the NH<sub>4</sub><sup>+</sup> cations.

Table 4.16: A table of idealised valence sums in Sc-5.

Atom	$\Sigma s_{ij}$	Atom	$\Sigma s_{ij}$
Sc1	3.03	F3	1.01
Sc2	3.15	F4	1.01
F1	1.01	F5	0.55
F2	0.79		

Table 4.17 shows selected bond distances in Sc-5.

Table 4.17: A table of selected bond distances in Sc-5 (i)  $-x+1/2, -y+1/2, -z$ .

Bond	Distance (Å)	Bond	Distance (Å)
Sc1-F1	2.05(1)	Sc2-F1	2.02(1)
Sc1-F2	2.10(1)	Sc2-F4	2.03(1)
Sc1-F2 <sup>i</sup>	2.12(1)	Sc2-F5	2.01(1)
Sc1-F3	2.01(1)		

The arrangement of  $\text{ScF}_7$  pentagonal bipyramids is similar to  $\text{KSc}_2\text{F}_7$ [30]. Six  $\text{ScF}_7$  pentagonal bipyramids share two corners and four edges to form six-membered ring channels in a distorted hexagonal conformation along the  $c$ -axis.  $\text{K}^+$  cations fill in the spaces created by the channels. The chains of  $\text{ScF}_7$  pentagonal bipyramids are the same as that shown in this new scandium fluoride. In the lower symmetry version of  $\text{Sc-5 Rb}_2\text{In}_3\text{F}_{11}$ [31], the  $\text{ScF}_6$  octahedra can tilt towards or away from each other. This is shown in Figure 4.35 with the structure of  $\text{KSc}_2\text{F}_7$ .

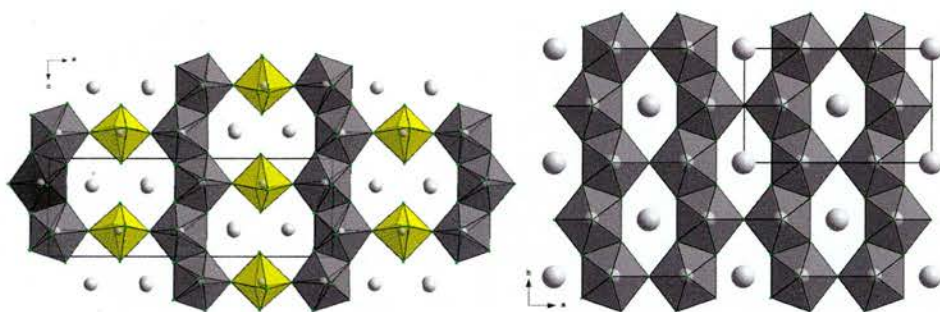


Figure 4.35: The structure of  $\text{Rb}_2\text{In}_3\text{F}_{11}$  along the  $b$ -axis and  $\text{KSc}_2\text{F}_7$  along the  $c$ -axis.

The crystallographic parameters of the three materials discussed is shown in Table 4.18. The unit cell parameters of  $\text{KSc}_2\text{F}_7$  are similar to Sc-5, but the a-axis is 8 Å shorter than the a-axis of Sc-5. This extension is due to the introduction of  $\text{ScF}_6$  octahedra.

Table 4.18: Selected crystal parameters for  $\text{Rb}_2\text{In}_3\text{F}_{11}$ ,  $\text{KSc}_2\text{F}_7$  and Sc-5.

	$\text{Rb}_2\text{In}_3\text{F}_{11}$	$\text{KSc}_2\text{F}_7$	Sc-5
Crystal system	Monoclinic	Orthorhombic	Orthorhombic
Space group	$\text{P}2_1/\text{m}$	Cmmm	Cmmm
a(Å)	18.838(3)	10.643(2)	18.50(1)
b(Å)	8.106(2)	6.540(1)	6.613(5)
c(Å)	6.633(2)	4.030(1)	4.025(3)
$\alpha(^{\circ})$	90.44(5)		

Figure 4.36 shows how the  $\text{ScF}_6$  octahedron is tilted.

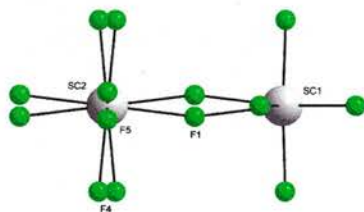
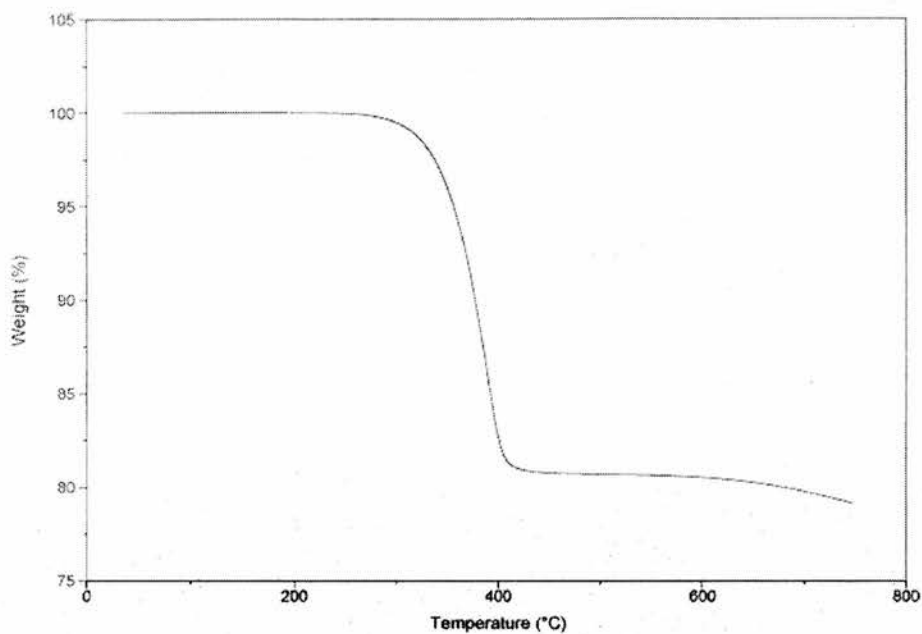


Figure 4.36: The tilting of the  $\text{ScF}_6$  octahedron in Sc-5.

## Thermogravimetric Analysis

The TGA plot of Sc-5 is shown in Figure 4.37.



*Figure 4.37: A TGA plot of Sc-5.*

Under  $N_2$ , a single weight loss takes place from 300 to 400 °C. This can be attributed to the loss of ammonium cations and  $F^-$  ligands (observed 19.3 %, calc. 19.5 %). X-ray powder diffraction confirms the decomposition of Sc-5 to  $ScF_3$  (PDF no. 44-1096).

## 4.7 Concluding Remarks

Five scandium fluoride structures with varying dimensionalities have been described in this chapter. Sc-1 is a 0-dimensional structure, which consists of isolated  $\text{ScF}_6$  octahedra, *trans*-1,4-diammoniumcyclohexane units, water molecules and  $\text{H}_3\text{O}^+$  cations. One fluorine atom is underbonded because it is hydrogen bonded to the  $\text{H}_3\text{O}^+$  cation. TGA shows two weight losses. The first represents a loss of a water molecule, the hydronium cation and one  $\text{F}^-$  ligand. The second step represents a degradation of the structure to  $\text{ScF}_3$ .

Sc-2 is a 1-dimensional structure, which consists of two types of  $[\text{ScF}_5]_\infty$  chains. One is eclipsed and the other is staggered with a F-Sc-Sc-F torsion angle of  $21.32^\circ$ . The crystallographic parameters shows that this structure is a pseudo  $\sqrt{2}$  distortion of  $[\text{C}_2\text{N}_2\text{H}_{10}][\text{MnF}_5]$ , which shows similar structural features except for the lack of staggered  $[\text{MnF}_5]_\infty$  chains. TGA shows a single step decomposition to  $\text{ScF}_3$ . MAS NMR shows two Sc-45 environments, which are split due to the quadrupolar Sc-45 nucleus.

Sc-3 is a 2-dimensional structure, which consists of sheets of corner-sharing  $\text{ScF}_6$  octahedra. Sc-3 is an example of a Dion-Jacobson phase, and is comparable to the  $\text{AMF}_4$  types. TGA shows a single step decomposition to  $\text{ScF}_3$ .

Sc-4 is another 2-dimensional structure of the  $\text{A}_{0.5}\text{MF}_4$  variety but the topology of each  $[\text{ScF}_4]^-$  sheet is a mixture of the elements reminiscent of HTBs and the TTBs. The structure of the  $[\text{ScF}_4]^-$  sheets can be reduced

down to the "bow-tie" unit, which consists of five corner-sharing  $\text{ScF}_6$  octahedra. Each sheet is separated by a layer of ethylenediammonium cations. TGA showed a single step decomposition to  $\text{ScF}_3$ . An SEM micrograph was taken to examine purity and Ge content.

Sc-5 is a 3-dimensional structure, which consists of  $\text{ScF}_6$  octahedra that corner share with edge sharing chains of  $\text{ScF}_7$  pentagonal bipyramids. The result of this connectivity are 10-membered "butterfly" channels, where ammonium cations lie. TGA showed a single step decomposition to  $\text{ScF}_3$ .

Scandium fluoride chemistry is a relatively unexplored area of solid state chemistry. It has been demonstrated that simple hydrothermal synthesis can produce a wide range of compounds with interesting structural features. This area is ripe for further development with lanthanide doping for luminescent properties, for example.

## References

- [1] R. H. Jones, J. Chen, J. M. Thomas, and A. George, *Chem. Mater.*, 1992, **4**, 808.
- [2] I. Bull, V. Young, S. J. Teat, L. Peng, C. P. Grey, and J. B. Parise, *Chem. Mater.*, 2003, **15**, 3818.
- [3] V. Soghomonian, R. C. Haushalter, and J. Zubieta, *Chem. Mater.*, 1995, **7**, 1648.
- [4] C. Reber, H. U. Guedel, G. Meyer, T. Schleid, and C. A. Daul, *Inorg. Chem.*, 1989, **28**, 3249.
- [5] V. H. Bode and E. Voss, *Z. Anorg. Allg. Chem.*, 1957, **290**, 1.
- [6] S. Carlson, X. Yiqiu, and R. Norrestam, *J. Solid State Chem.*, 1998, **135**, 116.
- [7] I. Ban, M. Kristl, B. Volavsek, and L. Golic, *Montash. Chem.*, 1999, **130**, 401.

- [8] M. Ramos Silva, A. Matos Beja, J. A. Paixao, L. Alte da Veiga, and J. Martin-Gil, *Z. Krist., New Cryst. Struct.*, 1999, **214**, 477.
- [9] K. K. Wu and I. D. Brown, *Mater. Res. Bull.*, 1973, **8**, 593.
- [10] S. P. Thanh, J. Renaudin, and V. Maisonneuve, *Solid State Sci.*, 2000, **2**, 143.
- [11] U. Bentrup, L. Schroder, and W. Massa, *Z. Naturforsch., B. J. Chem. Sci.*, 1992, **47**, 789.
- [12] D. R. Sears and J. L. Hoard, *J. Chem. Phys.*, 1969, **50**, 1066.
- [13] P. Nunez and T. Roisnel, *J. Solid State Chem.*, 1996, **124**, 338.
- [14] C. Brosset, *Z. Anorg. Allg. Chem.*, 1937, **235**, 139.
- [15] M. Dion, M. Ganne, and M. Tournoux, *Mat. Res. Bull.*, 1981, **16**, 1429.
- [16] A. J. Jacobson, J. W. Johnson, and J. T. Lewandowski, *Inorg. Chem.*, 1985, **24**, 3727.
- [17] J. Champarnaud-Mesjard and B. Frit, *Eu. J. Solid State Inorg. Chem.*, 1992, **29**, 161.
- [18] M. le Blanc, G. Férey, and R. Pape, *Acta Cryst. C*, 1985, **41**, 657.
- [19] G. Brunton, *Acta Cryst. B*, 1969, **25**, 600.
- [20] D. Goebbels and G. Meyer, *Z. Anorg. Allg. Chem.*, 2002, **628**, 1799.
- [21] J. Lapasset, P. Sciau, J. Moret, and N. Gros, *Acta Cryst. B*, 1986, **42**, 258.

- [22] S. T. Triantafyllou and P. C. Christidis, *Acta Cryst. C.*, 1999, **55**, 838.
- [23] A. Hussain, A. Ul-Monir, M. M. Murshed, and C. H. Ruscher, *Z. Anorg. Allg. Chem.*, 2002, **628(2)**, 416.
- [24] D. B. Mitzi, *Inorg. Chem.*, 2000, **39**, 6107.
- [25] W. T. A. Harrison, L. L. Dussack, and A. J. Jacobson, *Acta Cryst. C*, 1995, **39**, 1983.
- [26] W. T. A. Harrison, L. L. Dussack, J. T. Vaughey, T. Vogt, and A. J. Jacobson, *J. Mater. Chem.*, 1996, **6**, 81.
- [27] W. T. A. Harrison, L. L. Dussack, and A. J. Jacobson, *J. Solid State Chem.*, 1998, **138**, 365.
- [28] Z. Bircsak and W. T. A. Harrison, *Inorg. Chem.*, 1998, **37**, 3204.
- [29] D. Riou, D. Fayon, and D. Massiot, *Chem. Mater.*, 2002, **14**, 2416.
- [30] K. Guede and C. Hebecker, *Z. Naturforsch., B. Anorg. Chem., Organische Chem.*, 1985, **40**, 726.
- [31] J. Champarnaud-Mesjard and B. Frit, *Acta Cryst. B*, 1978, **34**, 736.

# Chapter 5

## Vanadium Oxyfluorides

### 5.1 Introduction

Several vanadium oxyfluorides and an oxide are described in this chapter, denoted VOXF-*n*. They range from polar ordering of  $[\text{VOF}_4(\text{H}_2\text{O})]^{2-}$  octahedral units,  $[\text{V}_2\text{O}_2\text{F}_6(\text{H}_2\text{O})_2]^{2-}$  dimeric units,  $[\text{V}_4\text{O}_4\text{F}_{14}]^{6-}$  tetrameric units, linear chains and a layered oxide.

Hydrothermal synthesis, X-ray crystallography, thermogravimetric analysis and CHN microanalysis experimental procedures were used throughout the work. X-ray data are shown in Tables 5.1 and 5.2. Atomic coordinates and temperature factors are tabulated in Appendix A in the file "Appendices.pdf" on the CD-ROM. Bond lengths and angles are tabulated in Appendix B.

Table 5.1: Crystallographic parameters of vanadium oxyfluorides.

	VOXF-1	VOXF-2	VOXF-3	VOXF-4
Formula	$[C_2N_2H_{10}][VOF_4(H_2O)]$	$[C_6N_2H_{16}][VOF_4(H_2O)]$	$(NH_4)_2VF_5$	$[C_2N_2H_{10}][VF_5]$
Formula weight	233.08	277.16	182.02	208.06
Crystal system	Monoclinic	Monoclinic	Orthorhombic	Tetragonal
Space group	$P2_1$	$P2_1/c$	$Pnma$	$P4/ncc$
$a$ (Å)	6.584(3)	8.816(2)	6.315(2)	12.837(2)
$b$ (Å)	5.827(2)	6.789(2)	7.636(2)	
$c$ (Å)	9.948(4)	18.724(5)	10.921(4)	7.951(2)
$\alpha$ (°)				
$\beta$ (°)		101.868(6)		
$\gamma$ (°)				
Volume(Å <sup>3</sup> )	378.6(3)	1096.7(4)	526.6(3)	1310.1(4)
Crystal size (mm)	0.2 x 0.1 x 0.03	0.2 x 0.1 x 0.05	0.17 x 0.03 x 0.03	0.1 x 0.1 x 0.1
Z	2	4	4	8
$\mu$ (mm <sup>-1</sup> )	1.342	0.945	1.900	1.542
Total reflections	1263	1958	516	593
Observed reflections ( $I > 2\sigma(I)$ )	1237	1866	467	583
$R_1, wR_2$ ( $I > 2\sigma(I)$ )	0.02, 0.05	0.02, 0.06	0.05, 0.14	0.03, 0.08
$R_1, wR_2$ (all data)	0.02, 0.05	0.02, 0.06	0.05, 0.14	0.03, 0.08

Table 5.2: Crystallographic parameters of vanadium oxyfluorides.

	VOXF-5	VOXF-6	VOXF-7
Formula	$[C_6N_4H_{21}]_2[V_4O_4F_{14}] \cdot 3H_2O$	$[C_6N_2H_{14}][V_2O_2F_6(H_2O)_2]$	$[C_3N_2H_{12}][V_4O_{10}]$
Formula weight	880.3	398.10	439.91
Crystal system	Monoclinic	Monoclinic	Monoclinic
Space group	$P2_1/c$	$P2_1/c$	$C2/c$
$a$ (Å)	9.953(3)	7.088(2)	7.977(3)
$b$ (Å)	10.621(2)	21.769(5)	10.099(3)
$c$ (Å)	15.3669(5)	12.964(4)	15.210(5)
$\alpha$ (°)			
$\beta$ (°)	104.139(8)	98.950(8)	104.08(1)
$\gamma$ (°)			
Volume(Å <sup>3</sup> )	1575.1(6)	1975.9(9)	1188.6(7)
Crystal size (mm)	0.2 x 0.1 x 0.03	0.15 x 0.15 x 0.2	0.15 x 0.01 x 0.01
Z	2	6	4
$\mu$ (mm <sup>-1</sup> )	1.279	1.506	3.098
Total reflections	2873	3545	1075
Observed reflections ( $I > 2\sigma(I)$ )	2624	1161	997
$R_w R_2$ ( $I > 2\sigma(I)$ )	0.03, 0.08	0.05, 0.16	0.03, 0.06
$R_1, wR_2$ (all data)	0.04, 0.08	0.10, 0.19	0.03, 0.06

## 5.2 [C<sub>2</sub>N<sub>2</sub>H<sub>10</sub>][VOF<sub>4</sub>(H<sub>2</sub>O)] (VOXF-1)

### 5.2.1 Experimental

#### Synthesis

0.1819 g (1 mmol) of V<sub>2</sub>O<sub>5</sub> was heated at 100 °C with 0.5 ml of HF and 5 ml of water for one hour. 5 ml of ethylene glycol was added to the solution and the colour of the solution changed from light yellow to orange. 0.5 ml of ethylene diamine was added to the solution (of pH 5) and was heated at 100 °C for 2 days. The colour of the solution changed to blue, indicating a change in oxidation state of the vanadium cations, and the pH at the end was 8. Blue plate like crystals were collected, washed in water and dried at room temperature (Found: C, 10.68 %; H, 5.64 %; N, 12.78 %. [C<sub>2</sub>N<sub>2</sub>H<sub>10</sub>][VOF<sub>4</sub>(H<sub>2</sub>O)] requires C, 10.77 %; H, 5.42 %; N, 12.56 %).

### 5.2.2 Characterisation

Single crystal X-Ray data were collected on a Rigaku single crystal diffractometer equipped with a CCD. Hydrogen atoms of the water ligand were located from the difference Fourier map. Bond valence calculations showed that the oxidation state of the vanadium atom had changed from 5+ to 4+.

VOXF-1 was heated from room temperature to 900°C, under an atmosphere of N<sub>2</sub>.

## 5.2.3 Discussion

### Structure

The structure of VOXF-1 is shown in Figure 5.1. It consists of isolated  $[\text{VOF}_4(\text{H}_2\text{O})]^{2-}$  units and ethylenediammonium cations. The  $[\text{VOF}_4(\text{H}_2\text{O})]^{2-}$  unit consists of one V atom co-ordinated by four equatorial F atoms, one O and one water molecule in the axial positions.

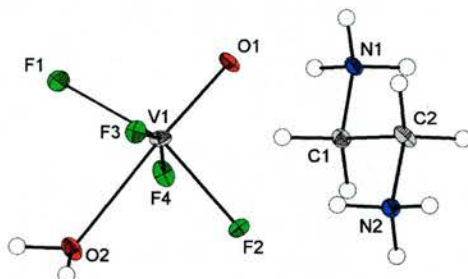


Figure 5.1: An ORTEP diagram of VOXF-1 at 50 % probability (arbitrary spheres for the H atoms).

Table 5.3 shows the distances between the V atom and the surrounding ligands, which are all underbonded and require hydrogen bonding from itself and the organic template. The V atom is displaced from the centre of the  $\text{VOF}_4(\text{H}_2\text{O})$  octahedron towards the vanadyl bond.

Table 5.3: Selected bond distances and bond valence sums of VOXF-1.

Bond	Distance ( $\text{\AA}$ )	Atom	$\Sigma S_{ij}$	Bond	Distance ( $\text{\AA}$ )	Atom	$\Sigma S_{ij}$
V1-F1	1.90(1)	V1	3.964	V1-F4	1.91(1)	F2	0.519
V1-F2	1.94(1)	O1	1.488	V1=O1	1.64(1)	F3	0.528
V1-F3	1.94(1)	O2	0.273	V1-OH <sub>2</sub>	2.26(1)	F4	0.567
		F1	0.589				

The  $[\text{VOF}_4(\text{H}_2\text{O})]^{2-}$  units are linked together *via* hydrogen bonds to the water ligand, the fluorine atoms and the ethylenediammonium cations. The interactions result in the alignment of the dipoles along the b-axis. This is shown in Figures 5.2 and 5.3.

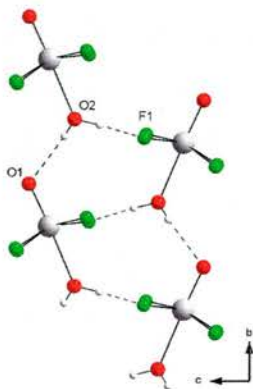


Figure 5.2: The hydrogen bonding of VOXF-1 showing the  $[\text{VOF}_4(\text{H}_2\text{O})]^{2-}$  units only.

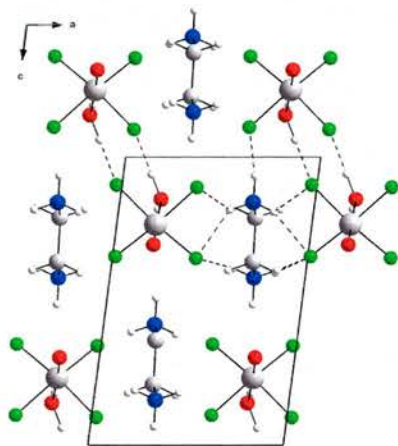


Figure 5.3: The hydrogen bonding of VOXF-1 showing the ethylenediammonium cations.

Each water ligand within the  $[\text{VOF}_4(\text{H}_2\text{O})]^{2-}$  unit hydrogen bonds to the vanadyl group and F ligand of another unit. Hydrogen bonding between this unit and the organic cations also takes place. It is worthy to note that a symmetrical organic template can arrange structural motifs into an asymmetrical structure.

Table 5.4 shows the hydrogen bonding in VOXF-1.

Table 5.4: Hydrogen bonds in VOXF-1 (i)  $-x, y-1/2, -z$  (ii)  $x, y-1, z$  (iii)  $-x+1, y+1/2, -z$  (iv)  $x+1, y+1, z$  (v)  $x, y+1, z$  (vi)  $-x+1, y+1/2, -z+1$  (vii)  $x+1, y, z$ .

D	H	A	D-H (Å)	H...A (Å)	D...A (Å)	$\angle$ DHA (°)
O2	Hw1	F1 <sup>i</sup>	0.93(4)	1.71(4)	2.65(1)	177(3)
O2	Hw2	O1 <sup>ii</sup>	0.70(4)	2.07(4)	2.76(1)	173(4)
N1	H1	F4 <sup>iii</sup>	0.91	1.79	2.66(1)	159
N1	H2	F3 <sup>iv</sup>	0.91	2.08	2.92(1)	153
N1	H2	F1 <sup>iv</sup>	0.91	2.29	2.98(1)	132
N1	H3	F2 <sup>v</sup>	0.91	2.18	2.98(1)	145
N1	H3	F4 <sup>v</sup>	0.91	2.32	3.01(1)	131
N2	H8	F2 <sup>vi</sup>	0.91	2.17	2.86(1)	132
N2	H8	F3 <sup>vi</sup>	0.91	2.20	2.86(1)	129
N2	H9	F3 <sup>vii</sup>	0.91	1.97	2.82(1)	155
N2	H10	F2	0.91	1.89	2.78(1)	163

The  $[\text{VOF}_4(\text{H}_2\text{O})]^{2-}$  unit is also seen in  $\text{Cs}_2\text{VOF}_4(\text{H}_2\text{O})$  [1]. The hydrogen bonded chains in  $\text{Cs}_2\text{VOF}_4(\text{H}_2\text{O})$  lie antiparallel to each other. The overall structure of VOXF-1 is closely related to  $[\text{C}_2\text{N}_2\text{H}_{10}][\text{AlF}_5(\text{H}_2\text{O})]$ [2]. It possesses the same space group and packing but it does not have the short vanadyl bond, so the octahedral units do not have the same degree of polarisation.

This work shows unusual hydrogen bond-mediated polar ordering of the  $[\text{VOF}_4(\text{H}_2\text{O})]^{2-}$  anion. Previous examples include the polar ordering of organic molecules within lamellar host-frameworks[3], polar ordering of template molecules within zeolites[4] and ligand mediated interactions[5].

### 5.2.4 Thermogravimetric Analysis

Figure 5.4 shows the TGA plot of VOXF-1

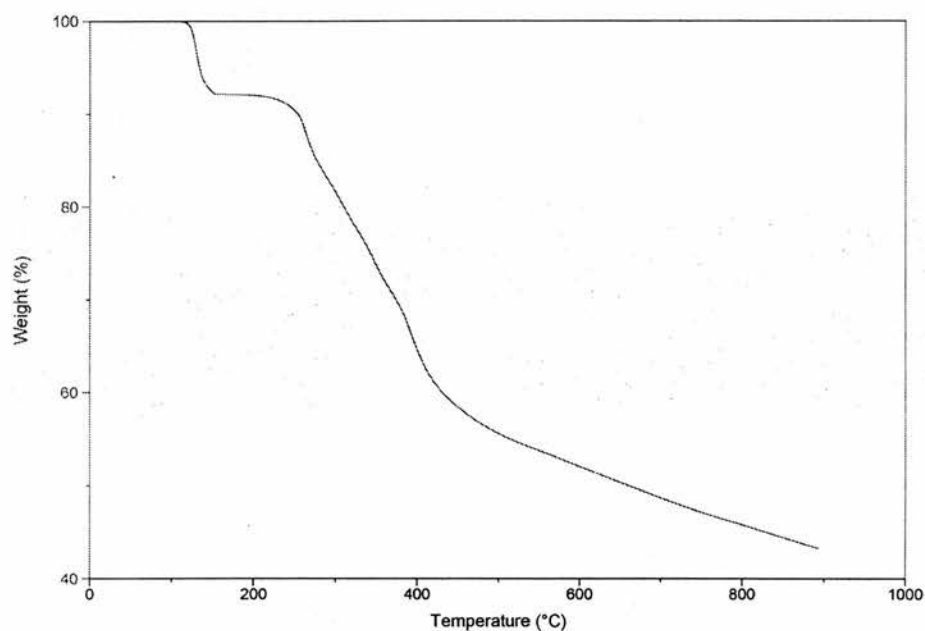


Figure 5.4: A TGA plot of VOXF-1.

Under  $\text{N}_2$ , two weight losses occur. The first step from 124 to 139 °C corresponds to the loss of the water ligand (observed 7.9 %, calculated 8.1 %). The second step from 249 to 385 °C corresponds to the degradation of the dehydrated residue to  $\text{VF}_3$  (PDF 6-209) (observed 38.1 %, calculated 47.4 %),

which is shown by the X-ray powder diffraction. This second step may be composed of several individual steps, but were difficult to resolve. The plateau from 139 °C to 249 °C indicates a stable phase. This is a dehydrated phase, although crystal quality degrades considerably (too much for single crystal X-ray diffraction). A powder pattern was taken but this phase is not closely related to VOXF-1.

Figure 5.5 shows the powder pattern of VOXF-4 before and after heating to 140 °C.

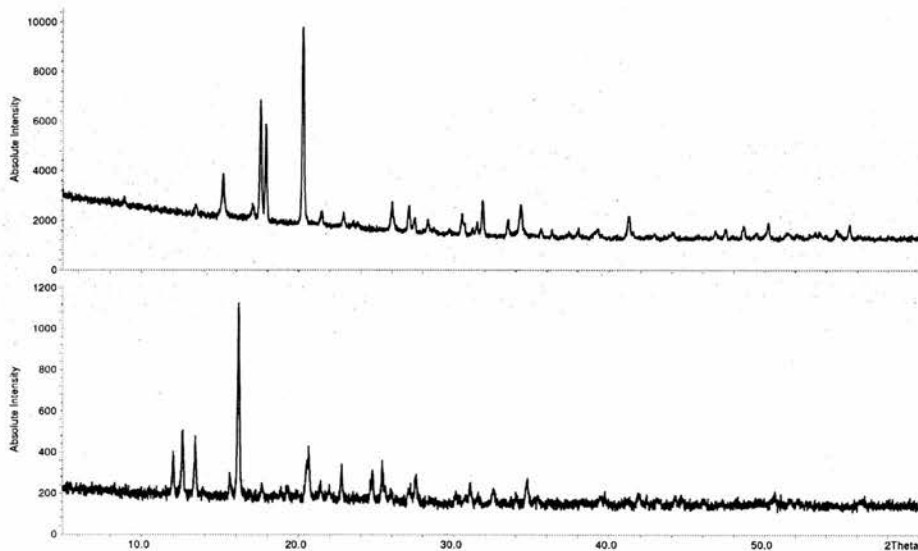


Figure 5.5: X-ray powder patterns of VOXF-1 before heating to 140 °C (top) and after heating (bottom).

### Second Harmonic Generation (SHG)

An examination of its SHG properties was carried out using the radiation from a Nd-vanadate laser. Its activity is 10-30 times less than LiNbO<sub>3</sub>, and

the damage threshold is 10 times less than the standard. This was carried out by Dr Manfred Buck.

## 5.3 [C<sub>6</sub>N<sub>2</sub>H<sub>16</sub>][VOF<sub>4</sub>(H<sub>2</sub>O)] (VOXF-2)

### 5.3.1 Experimental

#### Synthesis

0.1819 g of V<sub>2</sub>O<sub>5</sub> was heated at 100 °C for one hour with 5 ml water and 0.5 ml of HF. To the yellow solution, 5 ml of ethylene glycol was added and the solution changed to an orange colour. 0.5 ml of trans-1,4-diaminocyclohexane was added to give a green solution of pH 3. This was heated in a polypropylene bottle at 100 °C for 5 days. The blue plate like crystals were collected, washed in water and dried at room temperature overnight. The pH of the solution did not change over the course of the reaction (Found: C, 26.14 %; H, 6.41 %; N, 9.99 %. [C<sub>6</sub>N<sub>2</sub>H<sub>16</sub>][VOF<sub>4</sub>(H<sub>2</sub>O)] requires C, 26.00 %; H, 6.55 %; N, 10.11 %).

#### Characterisation

Single crystal X-ray data were collected on a Rigaku diffractometer equipped with a CCD. Hydrogen atoms for the water ligand were located from the electron density map, and could be refined.

For TGA, VOXF-2 was heated from room temperature to 625 °C, under N<sub>2</sub>.

## 5.3.2 Discussion

### Structure

VOXF-2 shows the same  $[\text{VOF}_4(\text{H}_2\text{O})]^{2-}$  unit seen in VOXF-1 however, a different hydrogen bonding scheme takes place.

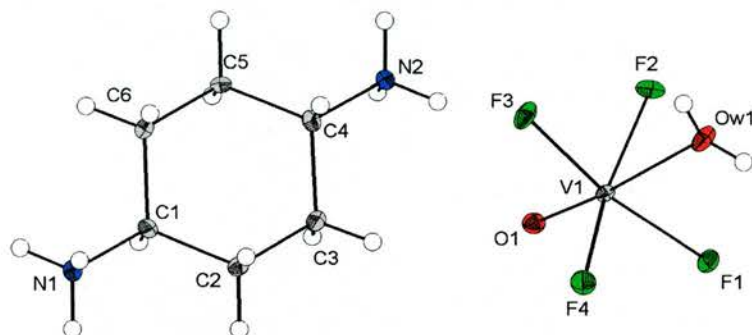


Figure 5.6: An ORTEP diagram VOXF-2 with the thermal ellipsoids at 50 % probability (arbitrary spheres for the H atoms).

Unlike VOXF-1, each water ligand bridges two units together by two fluorine atoms. Figure 5.7 shows the hydrogen bonding between each  $[\text{VOF}_4(\text{H}_2\text{O})]^{2-}$  unit.

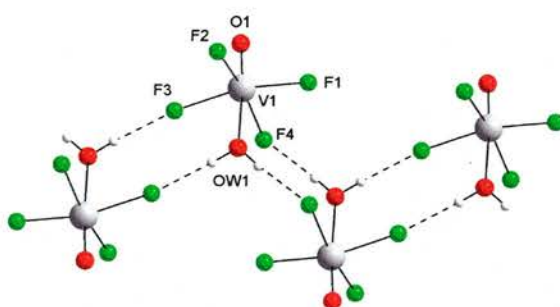


Figure 5.7: Part of the hydrogen bonding scheme of VOXF-2.

This creates hydrogen bonded units arranged in the centrosymmetric cell by the 1,4-diammoniumcyclohexane cations, as shown in Figure 5.8.

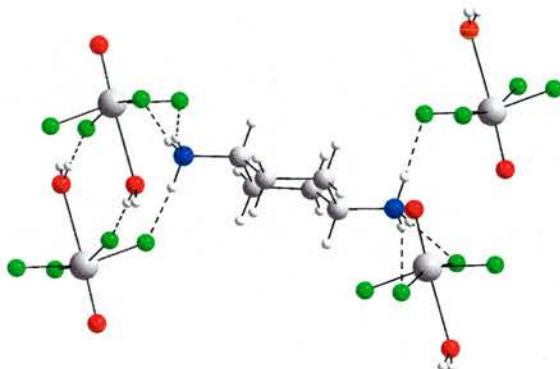


Figure 5.8: Part of the hydrogen bonding scheme of VOXF-2.

Table 5.5 shows the bond distances and bond valences of the atoms around the  $[\text{VOF}_4(\text{H}_2\text{O})]^{2-}$  unit. The bond valences of VOXF-2 are similar to VOXF-1.

Table 5.5: Selected bond distances and bond valences of VOXF-2.

Bond	Distance (Å)	Atom	$\Sigma s_{ij}$
V1-F1	1.92(1)	V1	4.005
V1-F2	1.96(1)	F1	0.550
V1-F3	1.95(1)	F2	0.501
V1-F4	1.93(1)	F3	0.516
V1-O1	1.61(1)	F4	0.540
V1-Ow1	2.26(1)	O1	1.622
		Ow1	0.276

Figure 5.9 shows the hydrogen bonding in  $[C_4N_2H_{12}][TiF_5(H_2O)]_2[6]$ , which is similar to VOXF-2 except that hydrogen bonding links the  $[TiF_5(H_2O)]^-$  units into chains that are connected together by the template cations.

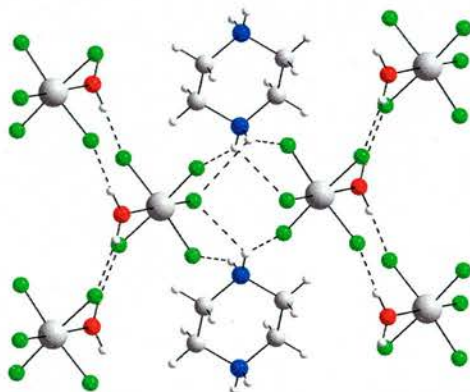


Figure 5.9: Part of the hydrogen bonding scheme of  $[C_4N_2H_{12}][TiF_5(H_2O)]_2$ .

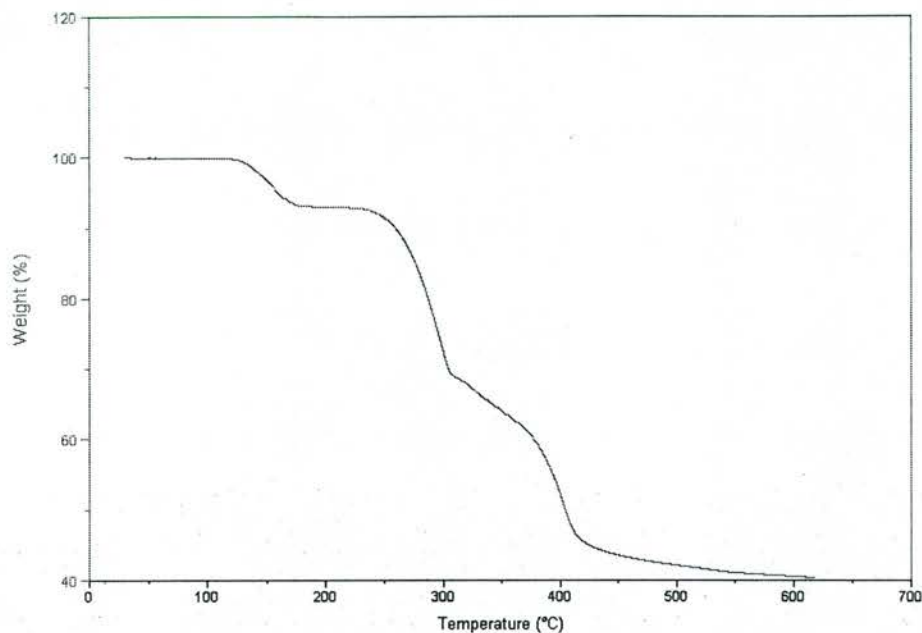
Table 5.6 shows the hydrogen bonding in VOXF-2.

Table 5.6: Hydrogen bonds in VOXF-2 (i)  $-x, -y, -z+1$  (ii)  $-x, -y+1, -z+1$  (iii)  $x, -y+3/2, z-1/2$  (iv)  $-x, y+1/2, -z+1/2$  (v)  $x, -y+1/2, z-1/2$  (vi)  $x, y+1, z$  (vii)  $-x+1, -y+1, -z+1$ .

D	H	A	D-H (Å)	H...A (Å)	D...A (Å)	∠ DHA (°)
Ow1	Hw1	F4 <sup>i</sup>	0.79(1)	1.90(1)	2.69(1)	173
Ow1	Hw2	F3 <sup>ii</sup>	0.81(1)	1.84(1)	2.65(1)	176
N1	H1	F2 <sup>iii</sup>	0.89	1.88	2.75(1)	164
N1	H1	F3 <sup>iii</sup>	0.89	2.48	3.03(1)	120
N1	H2	F4 <sup>iv</sup>	0.89	2.15	2.84(1)	133
N1	H2	F3 <sup>iv</sup>	0.89	2.44	3.21(1)	145
N1	H3	F1 <sup>v</sup>	0.89	1.80	2.67(1)	166
N2	H4	F3	0.89	1.97	2.77(1)	148
N2	H4	O1	0.89	2.42	3.12(1)	136
N2	H5	F1 <sup>vi</sup>	0.89	1.94	2.79(1)	158
N2	H6	F2 <sup>vii</sup>	0.89	1.80	2.69(1)	175
N2	H6	O1 <sup>vii</sup>	0.89	2.65	3.10(1)	112

## Thermogravimetric Analysis

Figure 5.10 shows the TGA plot of VOXF-2.



*Figure 5.10: The TGA plot of VOXF-2.*

Three weight losses occur under  $N_2$ . The first step from 134 to 169 °C shows the loss of a water ligand (observed 6.8 %, calc. 6.5 %). A second step occurs from 268 to 304 °C (observed 24.9 %) and a third step occurs from 304.4 to 412.5 °C (observed 25.0 %). X-ray powder diffraction of the residue shows that over these steps, VOXF-2 decomposes to  $VF_3$  (PDF 6-209). A stable phase exists from 169 °C to 268 °C. It is unclear what this phase is, but it is believed to be a condensed dehydrated phase. Similarly with VOXF-1, the quality of the crystals degraded too much upon heating for a single crystal X-ray study.

## 5.4 $(\text{NH}_4)_2\text{VF}_5$ (VOXF-3)

### 5.4.1 Experimental

#### Synthesis

0.1819 g of  $\text{V}_2\text{O}_5$ , 5 ml of water, 0.5 ml HF, 5 ml of ethylene glycol and 0.5 ml of tris(2-aminoethyl)amine (tren) was heated in a Teflon lined steel autoclave for 5 days at 160 °C. The green hexagonal rod like crystals were washed in water and allowed to dry at room temperature overnight. Throughout the reaction, the pH remained constant at 9 (Found: 4.17% H, 15.2% N.  $(\text{NH}_4)_2\text{VF}_5$  requires: 4.43% H, 15.39% N).

#### Characterisation

X-ray data were collected on a Rigaku single crystal diffractometer equipped with a CCD. The hydrogen atoms for the ammonium cations could be found from the electron density map and refined with the N-H distances fixed at 0.9 Å, the H-N-H angles fixed to be as close to tetrahedral as possible and each  $U_{iso}(\text{H})$  was fixed to be 1.5 times that of the carrier atoms. The presence of the ammonium cations was confirmed with CHN microanalysis. The tren molecule has decomposed hydrothermally to ammonium cations.

Thermogravimetric analysis was carried out on VOXF-3 from room temperature to 750 °C, under  $\text{N}_2$ .

## 5.4.2 Discussion

### Structure

The structure of VOXF-3 consists of *trans* connected infinite chains of  $\text{VF}_6$  octahedra, which run along the b-axis.

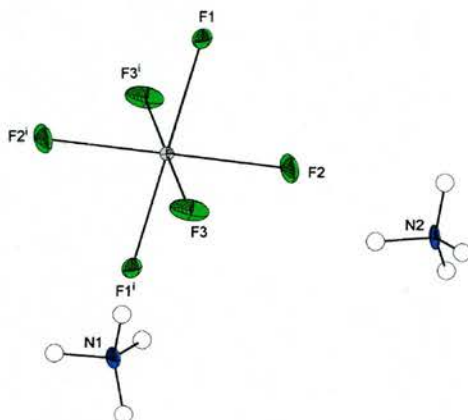


Figure 5.11: An ORTEP diagram of VOXF-3 with anisotropic displacements shown at 50 % probability (arbitrary spheres for the H atoms) (*i*)  $-x$ ,  $1-y$ ,  $-z$ .

The chains are interspersed by ammonium cations and the structure is similar to  $(\text{NH}_4)_2\text{FeF}_5$  [7] and  $(\text{NH}_4)_2\text{TiF}_5$  [8]. Figure 5.12 shows part of the  $[\text{VF}_5]^{2-}$  chain.

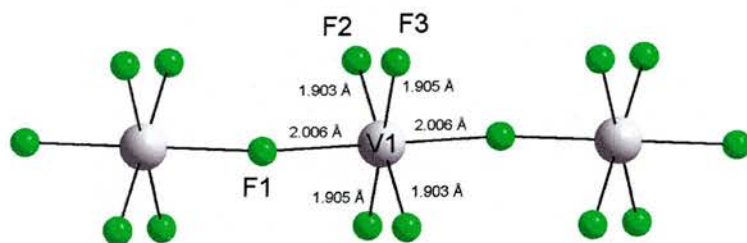


Figure 5.12: The  $\text{VF}_5$  chain found in VOXF-3.

The equatorial V-F bond lengths are within the order of 1.9 Å, while the axial V-F bond distances are closer to 2 Å. The V-F-V bond angle between  $\text{VF}_6$  octahedra is 144°, which is close to the Fe-F-Fe bond angle of 148° in  $(\text{NH}_4)_2\text{FeF}_5$ . Shown in Table 5.7 are bond distances and valence sums of VOXF-3.

Table 5.7: Bond distances and bond valence sums of VOXF-3.

Bond	Distance(Å)	Atom	$\Sigma s_{ij}$
V1-F1	2.01(1)	V1	3.198
V1-F2	1.90(1)	F1	0.880
V1-F3	1.91(1)	F2	0.581
		F3	0.578

Figure 5.13 shows the hydrogen bonding in VOXF-3. F2 is hydrogen bonded by two  $\text{NH}_4^+$  cations, F3 is hydrogen bonded by three, while F1 is only hydrogen bonded by one. F1 is the bridging atom in the  $[\text{VF}_5]^{2-}$  infinite chains.

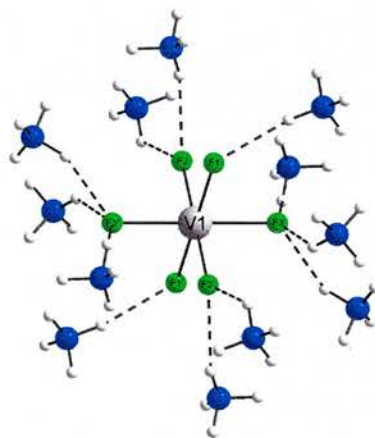


Figure 5.13: The hydrogen bonding scheme of VOXF-3 (i)  $-x, -1/2+y, -z$  (ii)  $-x, 1-y, -z$ .

Table 5.8 shows each hydrogen bond in VOXF-3. F2 and F3 are underbonded because they are the terminal F atoms in the  $\text{VF}_6$  octahedron. Hydrogen bonding from the ammonium cations is required to balance the valences of the F atoms. F1 is slightly underbonded as well, in spite of it being the bridging atom. Only one ammonium cation is required to balance the valence.

Table 5.8: Hydrogen bonds in VOXF-3 (i)  $-x+1/2, -y+1, z+1/2$ , (ii)  $x-1/2, y, -z+1/2$ , (iii)  $-x+1, -y+1, -z$ , (iv)  $-x+1/2, -y+1, z-1/2$ , (v)  $x+1/2, y, -z-1/2$ .

D	H	A	D-H (Å)	H...A (Å)	D...A (Å)	$\angle\text{DHA}$ (°)
N1	H1A	F3	0.89(2)	2.18(1)	2.84(1)	131(1)
N1	H1B	F2 <sup>i</sup>	0.87(2)	2.09(2)	2.90(1)	154(3)
N1	H1B	F2 <sup>ii</sup>	0.87(2)	2.56(3)	3.01(1)	113(3)
N1	H1C	F3 <sup>ii</sup>	0.89(2)	2.24(1)	2.91(1)	137(1)
N2	H2A	F1 <sup>iii</sup>	0.87(2)	2.05(2)	2.91(1)	170(6)
N2	H2B	F2	0.89(2)	2.15(2)	2.82(1)	132(2)
N2	H2C	F3 <sup>iv</sup>	0.86(2)	2.17(3)	2.88(1)	141(3)
N2	H2C	F2 <sup>v</sup>	0.86(2)	2.55(3)	3.24(1)	138(4)
N2	H2C	F3 <sup>iii</sup>	0.86(2)	2.59(4)	3.00(1)	111(3)

Figure 5.14 shows VOXF-3 along each crystallographic axis. VOXF-3 is a structural analogue of  $(\text{NH}_4)_2\text{FeF}_5$  [9] and  $(\text{NH}_4)_2\text{TiF}_5$  [10].

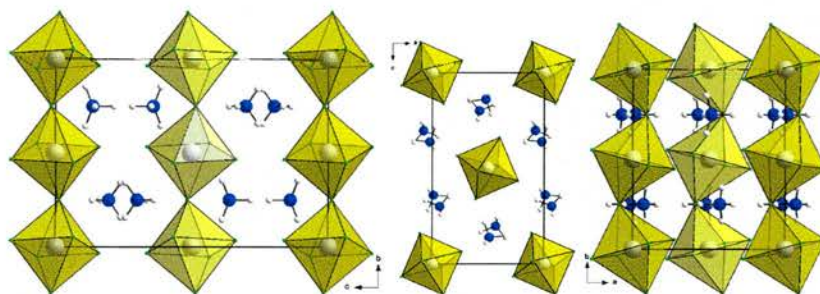
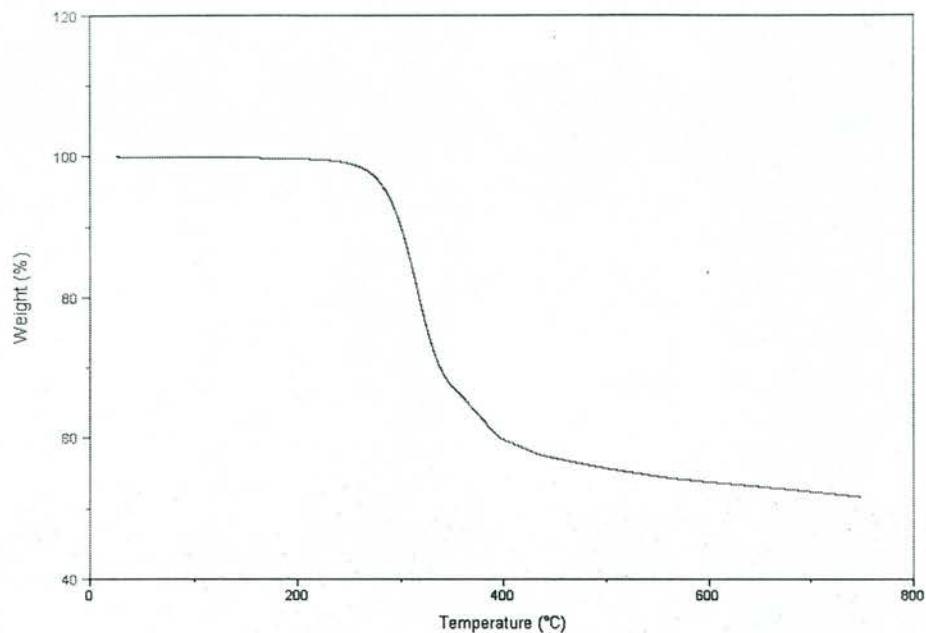


Figure 5.14: VOXF-3 along the  $a$ -,  $b$ - and  $c$ -axis (left to right).

## Thermogravimetric Analysis

Figure 5.15 shows the TGA plot of VOXF-3.



*Figure 5.15: A TGA plot of VOXF-3.*

Under  $N_2$ , one single weight loss occurs from 285 to 400 °C. This corresponds to the condensation of the structure to  $VF_3$  (PDF no. 6-209) (observed, 43 %, calc. 41 %).

## 5.5 [C<sub>2</sub>N<sub>2</sub>H<sub>10</sub>][VF<sub>5</sub>] (VOXF-4)

### 5.5.1 Experimental

#### Synthesis

0.1819 g of V<sub>2</sub>O<sub>5</sub>, 0.2665 g of CrCl<sub>3</sub>.6H<sub>2</sub>O, 5 ml H<sub>2</sub>O and 1 ml HF was heated in a polypropylene bottle for half an hour at 100 °C. 5 ml of ethylene glycol was added to the mixture and 0.5 ml ethylenediamine to bring the pH up to 8. This was heated in a Teflon lined steel autoclave for 5 days at 160 °C. The pH at the end of the experiment increased to 9 (Found: C 11.66 %, H 4.92 %, N 13.52 %; [C<sub>2</sub>N<sub>2</sub>H<sub>10</sub>][VF<sub>5</sub>] requires C 11.55 %, H 4.84 %, N 13.46 %).

### 5.5.2 Characterisation

Single crystal X-Ray data of the green rod-like crystals was collected on a Rigaku single crystal diffractometer equipped with a CCD.

VOXF-4 was heated from room temperature to 750 °C, under an atmosphere of N<sub>2</sub>.

### 5.5.3 Discussion

#### Structure

The structure of VOXF-4 is shown in Figure 5.16.

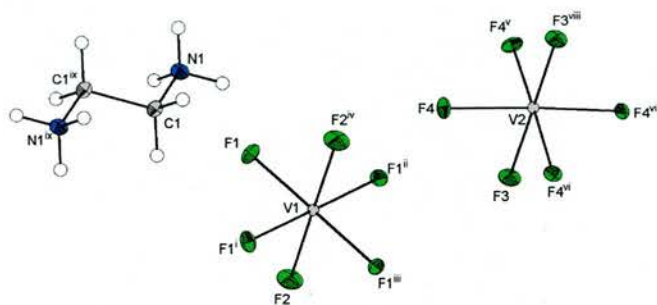


Figure 5.16: An ORTEP diagram of VOXF-4 with thermal ellipsoids shown at 50 % probability (arbitrary spheres for the H atoms) (i)  $1-y, 1-x, 1/2-z$  (ii)  $-1/2+y, 1/2+x, 1/2-z$  (iii)  $1/2-x, 3/2-y, z$  (iv)  $1/2-x, y, 1/2+z$  (v)  $3/2-y, x, z$  (vi)  $y, 3/2-x, z$  (vii)  $3/2-x, 3/2-y, z$  (viii)  $3/2-x, y, 1/2+z$  (ix)  $-x, 2-y, 1-z$ .

Because there are two metal sources in the above reaction, it can be unclear whether each metal site is occupied by a vanadium atom, a chromium atom or both. However, elemental percentages for VOXF-4 with chromium atoms in each metal site would be lower than for vanadium atoms in each metal site with C 11.49 %, H 4.82 %, N 13.4 %. The elemental percentages of VOXF-4 were much higher. Refining the metal sites occupied by chromium atoms,  $R_{all}$  increases to 0.035 and  $wR_2$  increases to 0.120. EDX confirms the absence of Cr, because it does not appear in the elemental analysis. This body of evidence suggests that vanadium is the only metal present within the structure.

The structure of VOXF-4 consists of infinite chains of  $\text{VF}_6$  octahedra, which run along the c-axis. It is isostructural to Sc-2, including the eclipsed and staggered arrangement of the  $[\text{VF}_5]^{2-}$  chains. The F-V-V-F torsion angle of  $28.21^\circ$  is wider than the F-Sc-Sc-F torsion angle of  $21.34^\circ$ .

Figure 5.17 shows the hydrogen bonding scheme of VOXF-4, and it is exactly the same as Sc-2.

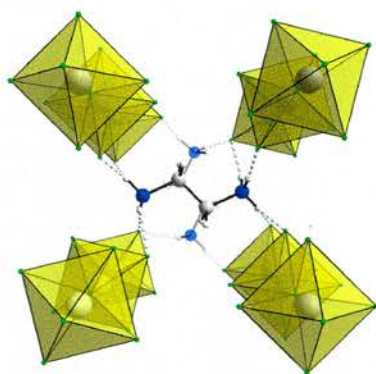


Figure 5.17: The hydrogen bonding scheme of VOXF-4 (i)  $1/2-x, y, 1/2+z$  (ii)  $-1/2+x, 2-y, 1/2-z$  (iii)  $1-y, 1/2+x, 1-z$ .

Table 5.9 shows the hydrogen bonds in VOXF-4.

Table 5.9: Selected hydrogen bonding of VOXF-4 (i)  $-y+1, x+1/2, -z+1$ , (ii)  $x-1/2, -y+2, -z+1/2$  (iii)  $y-1/2, x+1/2, -z+1/2$ .

D	H	A	D-H (Å)	H...A (Å)	D...A (Å)	$\angle\text{DHA}$
N1	H1	F1	0.91	2.02	2.65(1)	125
N1	H2	F4 <sup>i</sup>	0.91	1.87	2.78(1)	175
N1	H3	F4 <sup>ii</sup>	0.91	1.89	2.74(1)	154
N1	H3	F4 <sup>iii</sup>	0.91	2.64	3.22(1)	122

Table 5.10 shows the bond distances and bond valence sums of the atoms around the  $\text{VF}_6$  octahedron. F1 and F4 are underbonded and require hydrogen bonding from the organic template.

Table 5.10: Bond valences of  $\text{VOXF-4}$  ( $i$ )  $3/2-x, y, 1/2+z$ .

Bond	Distance (Å)	Atom	$\Sigma s_{ij}$	Bond	Distance (Å)	Atom	$\Sigma s_{ij}$
V1-F1	1.91(1)	V1	3.216	V2-F3 <sup>i</sup>	1.97(1)	F2	0.945
V1-F2	1.99(1)	V2	3.205	V2-F4	1.91(1)	F3	0.925
V2-F3	2.00(1)	F1	0.573			F4	0.570

### Thermogravimetric Analysis

Figure 5.18 shows a TGA plot of  $\text{VOXF-4}$ .

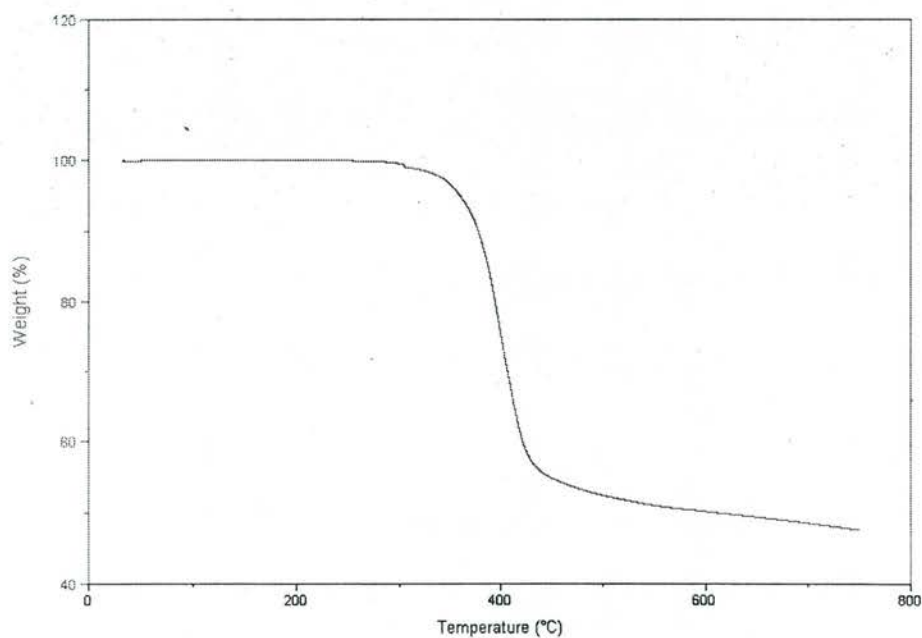
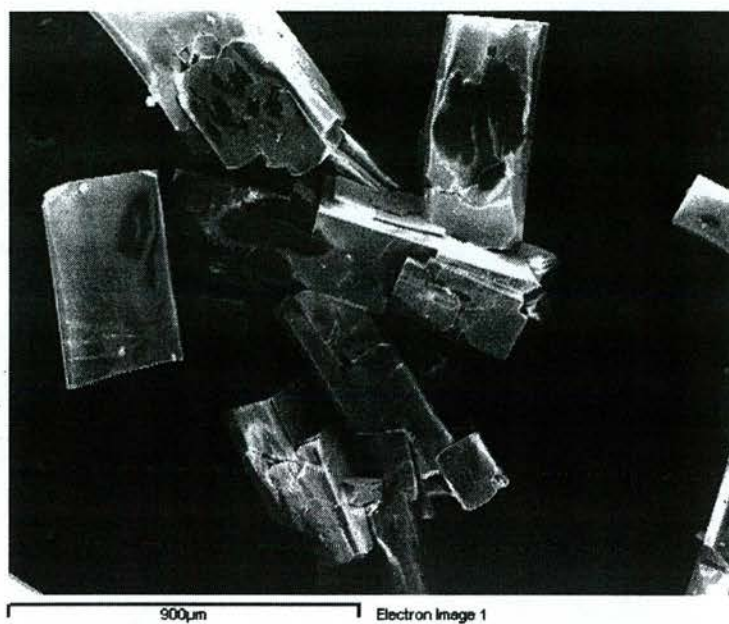


Figure 5.18: The TGA curve of  $[\text{C}_2\text{N}_2\text{H}_{10}][\text{VF}_5]$

The single step weight loss under  $N_2$  from 370 to 425 °C is the decomposition of VOXF-4 to  $VF_3$  (PDF 6-209) (observed 48.7 %, calculated 48.1 %).

## SEM

Figure 5.19 shows an electron micrograph of VOXF-4, and elemental analysis (EDX) confirms the absence of Cr atoms from the structure.



*Figure 5.19: An electron micrograph of VOXF-4.*

An average atomic percentage (Figure 5.11) show a F:V ratio of 5:1. This confirms the lack of Cr in the material. This study also shows a significant quantity of Al, a contaminant from the sample holder.

*Table 5.11: Elemental analysis of VOXF-4.*

Spectrum	Atomic %			
	1	2	3	Mean
F	85.9	81.0	83.3	83.4
Al	0.5	1.4	0.7	0.9
V	13.6	17.6	16.1	15.8

Figure 5.20 shows an elemental analysis of three single spots of the sample.

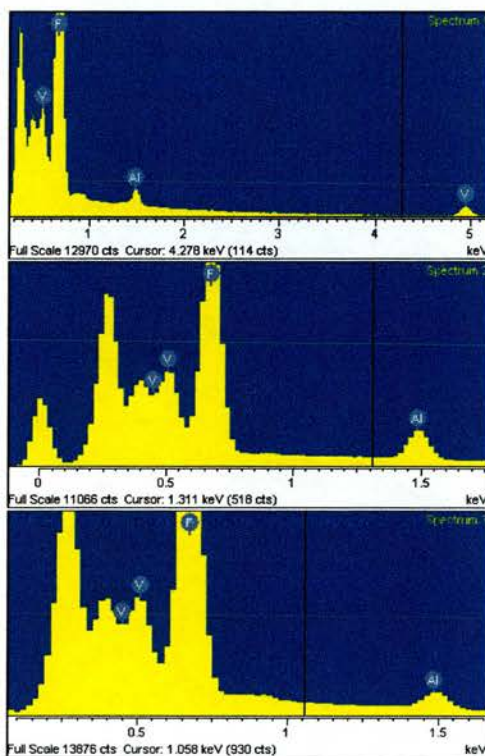


*Figure 5.20: An elemental analysis of VOXF-4 (spectrum 1 top, spectrum 2 middle and spectrum 3 bottom).*

## 5.6 $[\text{C}_6\text{N}_4\text{H}_{21}]_2[\text{V}_4\text{O}_4\text{F}_{14}]\cdot 3\text{H}_2\text{O}$ (VOXF-5)

### 5.6.1 Experimental

#### Synthesis

0.1818 g of  $\text{V}_2\text{O}_5$ , 0.5 ml HF and 5 ml water was heated in a polypropylene bottle for one hour at 100 °C. 5 ml of ethylene glycol was added to the yellow solution. The colour of the solution changed to orange. Finally, 0.5 ml tris(2-aminoethyl)amine (tren) was added and the mixture (of pH 5) was heated for 24 hours at 100 °C. After the reaction, the pH remained at 5 but the colour of the solution changed to blue indicating a change of oxidation state of the vanadium cation. Blue plate like crystals were collected, washed in water and dried at room temperature (Found: 16.51 % C, 5.41 % H, 11.74 % N;  $[\text{C}_6\text{N}_4\text{H}_{21}][\text{V}_2\text{O}_2\text{F}_7]\cdot 1.5\text{H}_2\text{O}$  requires 16.26 % C, 5.46 % H and 12.64 % N).

#### Characterisation

Single crystal X-ray data were collected on a Rigaku single crystal diffractometer equipped with a CCD. Hydrogen atoms around the water molecules could not be found from the difference Fourier map. Bond valence sum calculations showed that the oxidation state of the vanadium atoms changed from 5+ to 4+. This would be consistent with the colour change during the reaction and the coloured crystals.

VOXF-5 was heated from room temperature to 700 °C, under an atmosphere of  $\text{N}_2$ .

## 5.6.2 Discussion

### Structure

Figure 5.21 shows the structure of VOXF-5. VOXF-5 was synthesised under a higher temperature than VOXF-3, otherwise the synthetic conditions are similar. The organic template had decomposed in VOXF-3 but has remained intact in VOXF-5. VOXF-5 consists of  $[V_4O_4F_{14}]^{6-}$  cyclic tetramers interspersed by triprotonated tren molecules and water molecules.

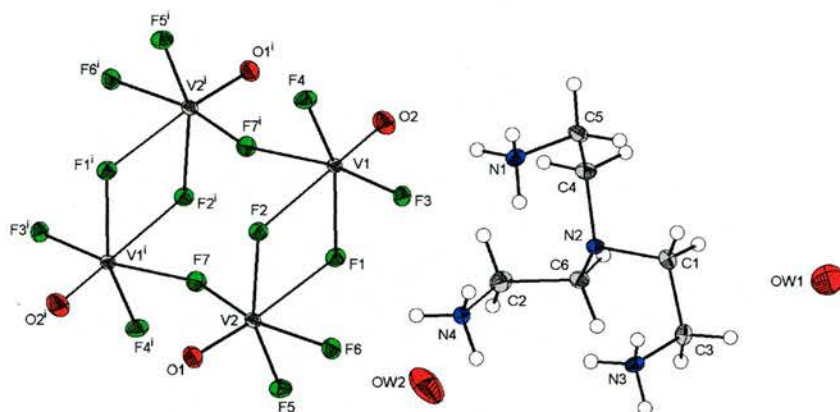


Figure 5.21: An ORTEP diagram of VOXF-5 with thermal ellipsoids at 50 % probability (arbitrary spheres for the H atoms) (*i*)-*x*, *2*-*y*, -*z*.

Two  $\text{VOF}_5$  octahedra edge-share *via* two fluorine atoms to leave the oxygen atom exposed. This double octahedron unit joins up with another *via* two linking F atoms. Figure 5.22 shows how one triprotonated tren molecule links three tetramers and one water molecule together *via* hydrogen bonding.

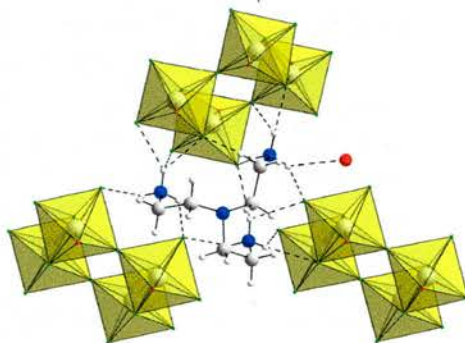


Figure 5.22: The hydrogen bonding scheme of VOXF-5.

Each vanadium atom is displaced from the centre of the octahedron towards the terminal oxygen atom. Table 5.12 show the bond distances within each  $\text{VOF}_5$  octahedron.

Table 5.12: Selected bond distances of VOXF-5 (*i*)  $-x, -y+2, -z$ .

Bond	Distance (Å)	Bond	Distance (Å)
V1-O2	1.594(2)	V2-O1	1.604(2)
V1-F1	1.972(1)	V2-F1	2.277(2)
V1-F2	2.260(2)	V2-F2	1.953(1)
V1-F3	1.920(1)	V2-F5	1.905(1)
V1-F4	1.924(1)	V2-F6	1.910(1)
V1-F7 <sup>z</sup>	1.973(1)	V2-F7	1.936(1)

Table 5.13 shows the bond valence sums in VOXF-5. Some of the ligand atoms are underbonded, and they require hydrogen bonding from the template cations to balance the valences.

Table 5.13: Bond valence sums of VOXF-5.

Atom	$\Sigma s_{ij}$	Atom	$\Sigma s_{ij}$
V1	3.947	F5	0.575
V2	4.009	F6	0.567
F1	0.689	F7	1.008
F2	0.726	O1	1.671
F3	0.552	O2	1.622
F4	0.546		

Table 5.14 shows this hydrogen bonding in detail.

Table 5.14: The hydrogen bonding in VOXF-5 (i)  $x, -y+3/2, z+1/2$  (ii)  $-x, y-1/2, -z+1/2$  (iii)  $x, y-1, z$  (iv)  $-x, -y+1, -z$ .

D	H	A	D-H (Å)	H...A (Å)	D...A (Å)	$\angle DHA$ °
N1	H1	F1 <sup>i</sup>	0.890	1.964	2.849	172.70
N1	H1	F7 <sup>i</sup>	0.890	2.522	2.983	112.95
N1	H1	F5 <sup>i</sup>	0.890	2.639	3.093	112.72
N1	H2	F2 <sup>ii</sup>	0.890	2.160	2.821	130.57
N1	H2	F4 <sup>ii</sup>	0.890	2.299	3.077	145.88
N1	H3	F3	0.890	2.007	2.776	143.83
N1	H3	Ow2 <sup>i</sup>	0.890	2.599	3.157	121.56
N3	H4	F4 <sup>iii</sup>	0.890	1.875	2.730	160.32
N3	H5	F5 <sup>iv</sup>	0.890	2.022	2.711	133.36
N3	H6	F2 <sup>ii</sup>	0.890	2.042	2.770	138.23
N3	H6	F6 <sup>ii</sup>	0.890	2.226	2.990	143.70
N4	H7	F6	0.890	2.071	2.742	131.40
N4	H7	F1	0.890	2.190	2.947	142.64
N4	H8	F3	0.890	2.291	2.752	112.04
N4	H8	F4 <sup>ii</sup>	0.890	2.412	3.172	143.50
N4	H9	F5 <sup>iv</sup>	0.890	1.860	2.690	154.27
N4	H9	F6 <sup>iv</sup>	0.890	2.593	3.284	135.13

Figure 5.23 shows the tetrameric unit in  $[\text{C}_{10}\text{H}_{10}\text{WCl}_2]_2[\text{W}_4\text{F}_{18}]$ [11]. The  $\text{WF}_6$  octahedra are linked *via* their corners to form the tetrameric cluster. In this example, the W atoms are displaced from the centre of the cluster towards the apex of each  $\text{WF}_6$  octahedron.

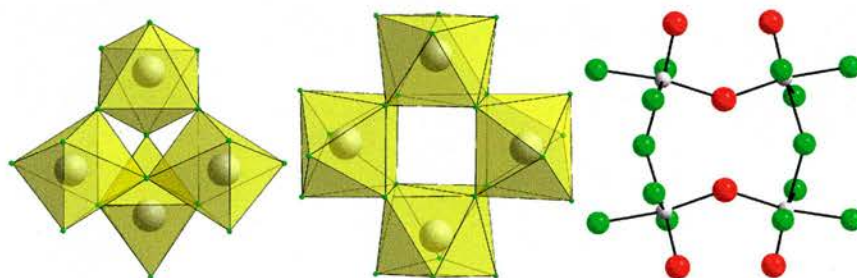


Figure 5.23: The  $[\text{C}_{10}\text{H}_{10}\text{WCl}_2]_2[\text{W}_4\text{F}_{18}]$  (left),  $[\text{C}_1\text{N}_4\text{H}_8]_4[\text{Zr}_4\text{F}_{24}]\cdot 4\text{H}_2\text{O}$  (centre) and  $[\text{V}_4\text{O}_6\text{F}_{14}]^{6-}$  tetrameric units (right).

Also shown is another tetrameric unit in  $[\text{C}_1\text{N}_4\text{H}_8]_4[\text{Zr}_4\text{F}_{24}]\cdot 4\text{H}_2\text{O}$ [12]. Each  $\text{ZrF}_8$  square antiprism is connected to three others *via* edge-sharing to produce the  $[\text{Zr}_4\text{F}_{24}]^{4-}$  tetrameric unit.

$\text{Ba}_3\text{V}_4\text{O}_6\text{F}_{14}$  [13] also shows a tetramer arrangement, which is built up of corner-sharing  $\text{VO}_2\text{F}_4$  octahedra instead of the edge-sharing  $\text{VOF}_5$  octahedra in VOXF-5. The V-F bond *trans* to the vanadyl bond is 0.2 Å shorter than that of VOXF-5.

## Thermogravimetric Analysis

Figure 5.24 shows a TGA plot of VOXF-5.

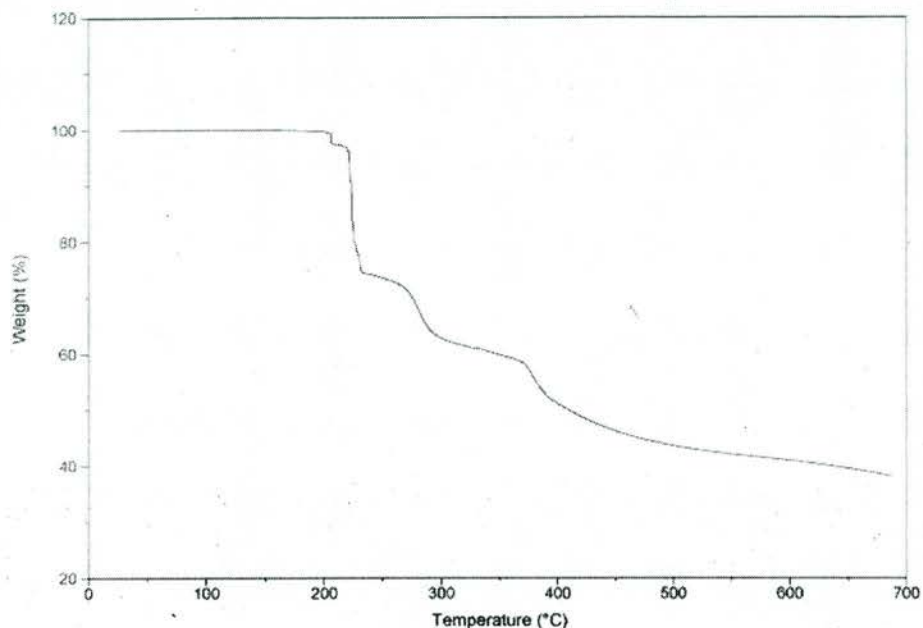


*Figure 5.24: A TGA plot of VOXF-5.*

Under  $N_2$ , there are four weight losses, one from 206 to 207 °C (2.5 %), the second from 207 to 225 °C (24 %), the third from 225 to 290 °C (11.8 %) and the fourth from 350 to 400 °C (18.5 %). It is unclear what these steps represent, but the structure decomposes to  $VF_3$  at 400 °C (PDF no. 6-209).

## 5.7 [C<sub>6</sub>N<sub>2</sub>H<sub>14</sub>][V<sub>2</sub>O<sub>2</sub>F<sub>6</sub>(H<sub>2</sub>O)<sub>2</sub>] (VOXF-6)

### 5.7.1 Experimental

#### Synthesis

0.1819 g of V<sub>2</sub>O<sub>5</sub>, 5 ml of water and 0.5 ml of HF was heated in a polypropylene bottle for one hour at 100 °C. To this yellow solution, 5 ml of ethylene glycol was added and the colour of the solution changed to orange. Finally, 0.3363 g of diazabicyclo[2.2.2]octane (dabco) was mixed with the solution (of pH 3). This was heated at the same temperature for five days and turquoise prismatic crystals with rounded edges precipitated. The pH of the solution increased to 5 (Found: 18.33 % C, 4.53 % H and 6.98 % N; [C<sub>6</sub>N<sub>2</sub>H<sub>14</sub>][V<sub>2</sub>O<sub>2</sub>F<sub>6</sub>(H<sub>2</sub>O)<sub>2</sub>] requires 18.10 % C, 4.56 % H and 7.04 % N).

#### Characterisation

Single crystal X-ray analysis was carried out on a Rigaku diffractometer equipped with a CCD. The dabco molecules are rotationally disordered in two positions. This is shown in Figure 5.25.

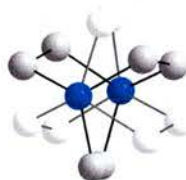


Figure 5.25: The dabco molecule showing the two alternative positions of the [dabcoH<sub>2</sub>]<sup>2+</sup> cation.

VOXF-6 was heated from room temperature to 750 °C, under an atmosphere of N<sub>2</sub>.

## 5.7.2 Discussion

### Structure

The structure consists of  $[V_2O_2F_6(H_2O)_2]^{2-}$  dimers surrounded by the disordered  $[dabcoH_2]^{2+}$  cations. The dimers are shown in Figure 5.26.

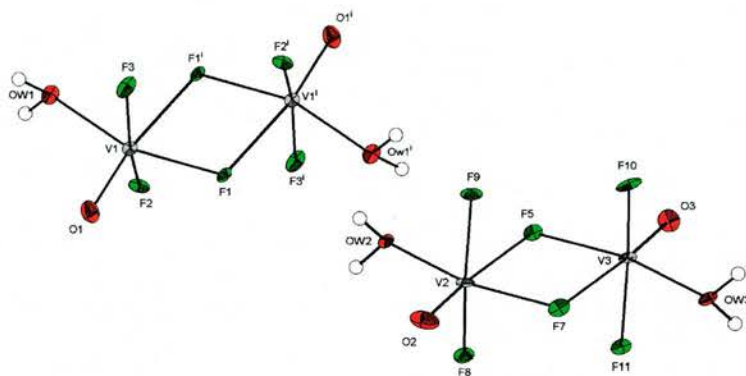


Figure 5.26: An ORTEP diagram of the  $[V_2O_2F_6(H_2O)_2]^{2-}$  dimers, with the thermal ellipsoids shown at 50 % probability (arbitrary spheres for the H atoms) (i)  $-x, 1-y, 1-z$ .

The asymmetric unit contains one whole molecule and half of a  $[dabcoH_2]^{2+}$  cation. The carbon atoms on the first  $[dabcoH_2]^{2+}$  cation were refined with half occupancy, and the hydrogen atoms were fixed riding upon their carriers. The carbon and nitrogen atom positions for the other half of the second  $dabcoH_2^{2+}$  cation was calculated and the bond distances within each half were fixed. The two halves were refined to reach an optimum distance from

each other and the hydrogen atoms were fixed in a similar way. Each  $U_{iso}(H)$  on the water molecules were refined to be 1.5 times that of the O atom.

Table 5.15 shows the bond distances between each V atom and its ligands. As expected, there are short V=O bonds and long V-OH<sub>2</sub> bonds, producing the characteristic displacement of the V atom away from the centre of the co-ordination sphere.

Table 5.15: Selected bond distances of VOXF-6 (i) -x, 1-y, 1-z.

Bond	Distance (Å)	Bond	Distance (Å)
V1-O1	1.595(4)	V2-F7	1.960(3)
V1-F3	1.921(3)	V2-Ow2	2.034(3)
V1-F2	1.948(3)	V2-F5	2.153(3)
V1-F1	1.953(2)	V3-O3	1.615(3)
V1-Ow1	2.026(3)	V3-F10	1.935(3)
V1-F1 <sup>†</sup>	2.148(3)	V3-F11	1.943(3)
V2-O2	1.601(4)	V3-F5	1.967(2)
V2-F8	1.925(3)	V3-OW3	2.025(3)
V2-F9	1.936(3)	V3-F7	2.166(3)
		F1-V1 <sup>†</sup>	2.148(3)

The bond valence sums in Table 5.16 shows significant underbonding of the terminal ligands, which require hydrogen bonding from the organic templated and other dimeric units.

Table 5.16: The bond valence sums of VOXF-6.

Atom	$\Sigma s_{ij}$	Atom	$\Sigma s_{ij}$	Atom	$\Sigma s_{ij}$
V1	3.960	Ow1	0.483	F5	0.774
V2	3.962	Ow2	0.501	F7	0.778
V3	3.855	Ow3	0.514	F8	0.503
O1	1.667	F1	0.790	F9	0.520
O2	1.649	F2	0.505	F10	0.506
O3	1.562	F3	0.519	F11	0.510

Figure 5.27 shows the hydrogen bonding scheme between the water molecules, fluorine atoms and [dabcoH<sub>2</sub>]<sup>2+</sup> cations.

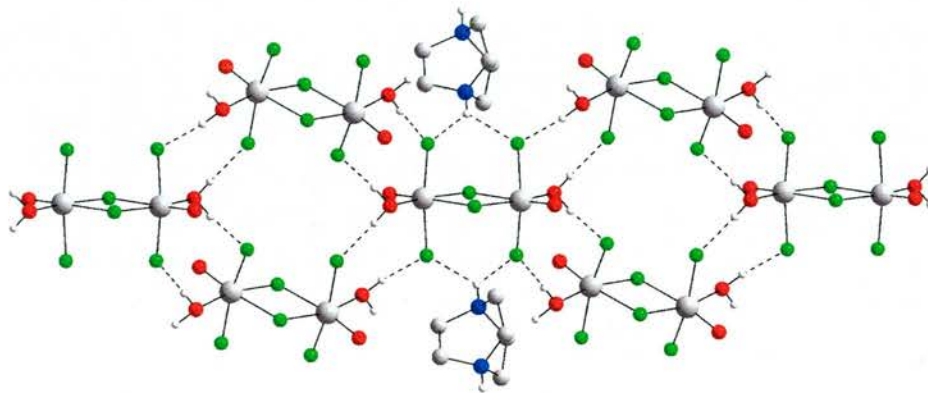


Figure 5.27: The hydrogen bonding of VOXF-6.

Figure 5.28 shows the dimeric unit in [C<sub>7</sub>NH<sub>10</sub>]<sub>2</sub>[V<sub>2</sub>O<sub>2</sub>F<sub>6</sub>(H<sub>2</sub>O)<sub>2</sub>][14]. This is an isomer of the dimer in VOXF-6, where the H<sub>2</sub>O ligand is *cis* to the F linkages. In VOXF-6, the H<sub>2</sub>O ligands are *trans* to the F linkages.

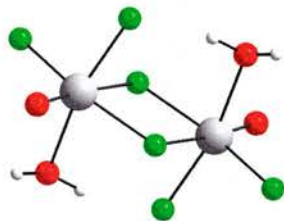


Figure 5.28: [C<sub>7</sub>NH<sub>10</sub>]<sub>2</sub>[V<sub>2</sub>O<sub>2</sub>F<sub>6</sub>(H<sub>2</sub>O)<sub>2</sub>]

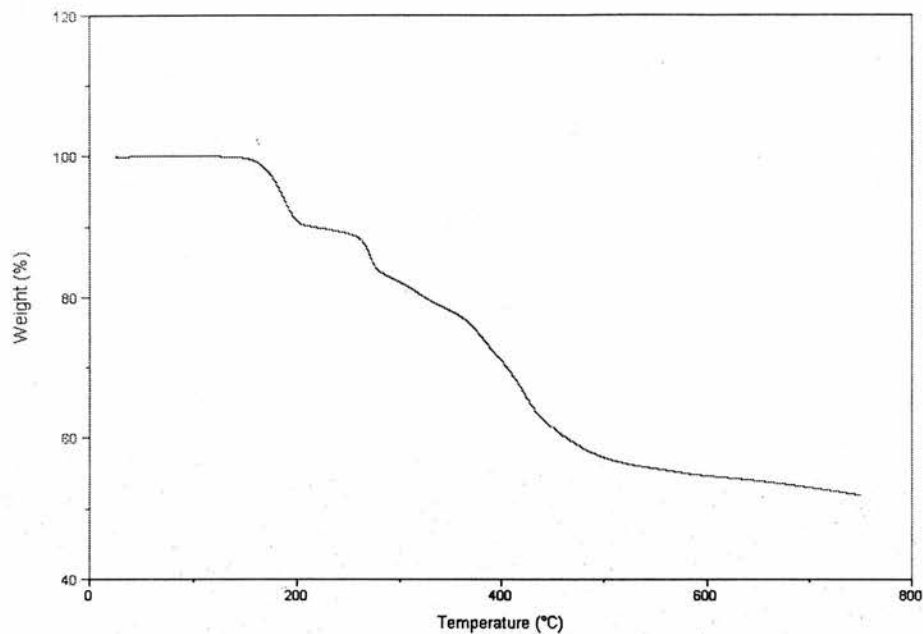
Table 5.17 shows these hydrogen bonds in detail.

Table 5.17: Hydrogen bonds in VOXF-6 (i)  $-x+1, y-1/2, -z+1/2$  (ii)  $x+1, -y+1/2, z-1/2$  (iii)  $-x-1, -y+1, -z$  (iv)  $-x, -y+1, -z+1$  (v)  $x, y, z+1$  (vi)  $-x, -y+1, -z+1$  (vii)  $x, -y+1/2, z+1/2$  (viii)  $x, -y+1/2, z-1/2$  (ix)  $x, y, z-1$ .

D	H	A	D-H (Å)	H...A (Å)	D...A (Å)	$\angle$ DHA (°)
N1	H4a	F8	0.91	2.08	2.80(1)	135.30
N1	H4a	F11	0.91	2.15	2.81(1)	129.29
N2	H5a	F3 <sup>i</sup>	0.91	2.07	2.79(1)	135.06
N2	H5a	F2 <sup>ii</sup>	0.91	2.14	2.81(1)	130.41
N3	H3c	F9	0.91	1.99	2.69(1)	131.99
N3	H3c	F10	0.91	2.17	2.85(1)	131.26
N3	H3c	F5	0.91	2.62	3.31(1)	132.98
N4	H30c	F10 <sup>iii</sup>	0.91	2.01	2.77(1)	140.59
N4	H30c	F9 <sup>iii</sup>	0.91	2.29	2.94(1)	127.97
OW1	H1	F9 <sup>iv</sup>	0.85	1.73	2.57(1)	173.80
OW1	H2	F10 <sup>v</sup>	0.78	1.82	2.60(1)	172.16
OW2	H3	F3 <sup>vi</sup>	0.78	1.81	2.59(1)	173.30
OW2	H4	F11 <sup>vii</sup>	0.86	1.72	2.57(1)	171.60
OW3	H5	F8 <sup>viii</sup>	0.81	1.79	2.59(1)	176.84
OW3	H6	F2 <sup>ix</sup>	0.84	1.74	2.58(1)	172.16

## Thermogravimetric Analysis

Figure 5.29 shows the TGA plot of VOXF-6.



*Figure 5.29: A TGA plot of VOXF-6.*

Under  $N_2$ , three weight losses occur. The first from 170 to 200 °C is the removal of the water ligands (observed 10 %, calculated 9 %). The next step from 250 to 275 °C, which is joined to the third weight loss up to 450 °C, is not known. Overall, the structure decomposes to  $VF_3$  (PDF no. 6-209).

## 5.8 $[\text{C}_3\text{N}_2\text{H}_{12}][\text{V}_4\text{O}_{10}]$ (VOXF-7)

### 5.8.1 Experimental

#### Synthesis

0.1819 g of  $\text{V}_2\text{O}_5$  was heated at 100 °C for one hour with 5 ml water and 0.5 ml of HF. To the yellow solution, 5 ml of ethylene glycol was added and the solution changed to an orange colour. Finally, 0.5 ml of 1,3-propylenediamine was added to give a green solution of pH 10. This was heated in a polypropylene bottle at 100 °C for 5 days. The dark blue crystals were washed in water and dried at room temperature overnight. Over the course of the reaction, the pH of the solution remained constant throughout (Found: 8.34 % C, 2.21 % H, 6.41 % N;  $[\text{C}_3\text{N}_2\text{H}_{12}][\text{V}_4\text{O}_{10}]$  requires 8.19 % C, 2.75 % H and 6.37 % N). This represents an attempt to synthesise a material similar to VOXF-1, but with a “longer” template.

## 5.8.2 Discussion

### Structure

The structure of VOXF-7 is shown in Figure 5.30.

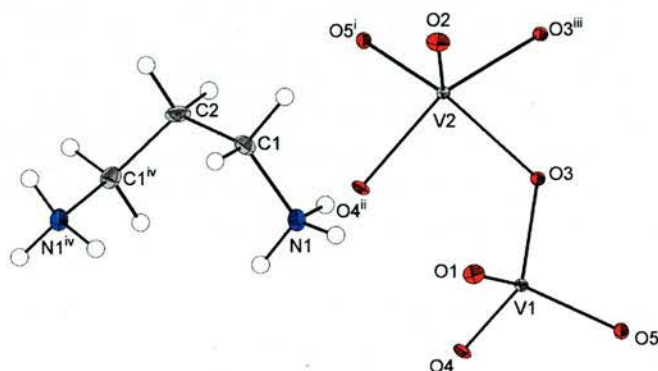


Figure 5.30: An ORTEP diagram of VOXF-7 with thermal ellipsoids at 50 % probability (arbitrary spheres for the H atoms) (i)  $-1/2+x, 1/2+y, z$  (ii)  $-1/2-x, 1/2-y, -z$  (iii)  $-x, 1-y, -z$  (iv)  $-1-x, y, 1/2-z$ .

VOXF-7 consists of  $\text{VO}_4$  tetrahedra and  $\text{VO}_5$  square pyramids. These form  $[\text{V}_4\text{O}_{10}]^{2-}$  layers, which are separated by the 1,3-propylenediammonium cations. VOXF-7 has the same composition of the oxide found by Riou and Férey [15]. There are two structural differences between the two. The  $\text{VO}_4$  tetrahedra in VOXF-7 are perfectly aligned along the  $c$ -axis, while in the Riou and Férey structure, the  $\text{VO}_4$  tetrahedra are aligned away from the direction of the  $c$ -axis. The organic template in VOXF-7 has a *syn* conformation, but it has a *gauche* conformation in the Riou and Férey structure. VOXF-7 was synthesised at a lower temperature than the Riou and Férey structure and without  $\text{SiO}_2$ .

Table 5.18 shows that VOXF-7 represents a higher symmetry version of the Riou and Férey structure with a similar cell size.

Table 5.18: A comparison of the unit cell parameters of VOXF-7 and the Riou and Férey structure.

	VOXF-7	Riou and Férey structure
Space group	C2/c	P2 <sub>1</sub> /n
a (Å)	7.977(3)	7.999(1)
b (Å)	10.099(3)	10.008(1)
c (Å)	15.210(5)	15.703(1)
$\beta$ (°)	104.08(1)	100.49(1)
Volume (Å <sup>3</sup> )	1188.6(7)	1236.2(2)

Figure 5.31 shows the conformation of the organic template in the two versions of the layered structure.

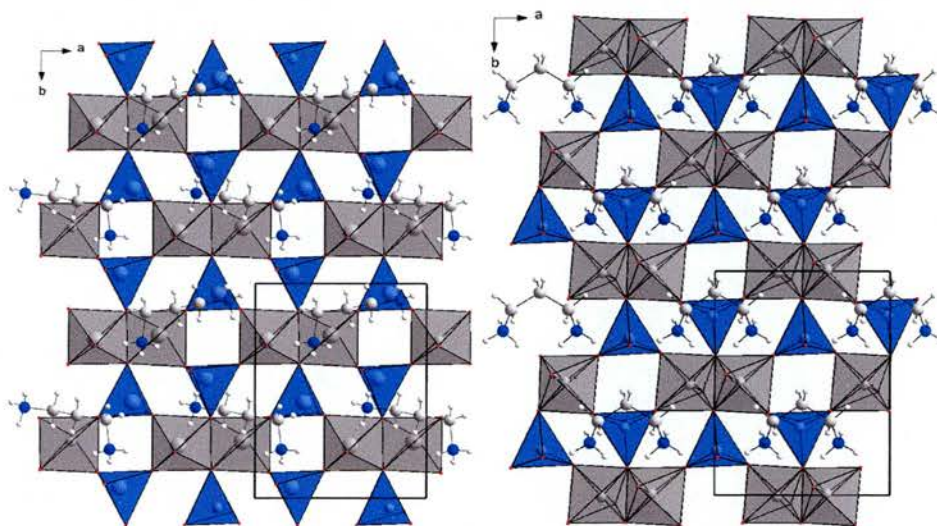


Figure 5.31: A view of the Férey layer topology (left) and the layer topology found in VOXF-7 (right).

Figure 5.32 shows the nature of the hydrogen bonding between each  $[\text{V}_4\text{O}_{10}]^{2-}$  layer and 1,3-propylenediammonium cations.

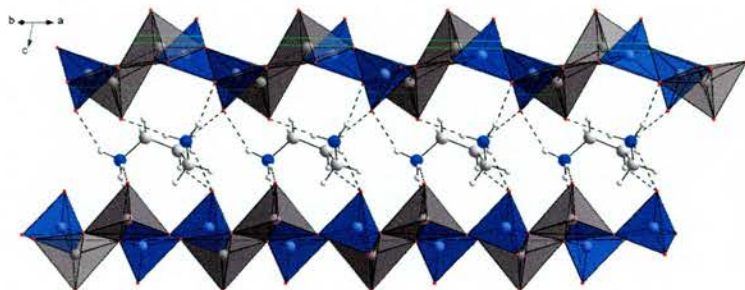


Figure 5.32: The hydrogen bonding scheme of VOXF-7.

Bond valence sums show that V1 is in the 5+ oxidation state, while V2 is in the 4+ oxidation state. Table 5.19 shows that O1, O3 and O5 require hydrogen bonding from the organic template to maintain their correct valencies.

Table 5.19: The bond valence sums of VOXF-7.

Atom	$\Sigma s_{ij}$
V1	4.983
V2	4.111
O1	1.575
O2	1.994
O3	1.830
O4	2.082
O5	1.613

Table 5.20 shows the bond distances around the  $\text{VO}_4$  tetrahedra and the  $\text{VO}_5$  trigonal bipyramids.

Table 5.20: Selected bond distances of  $\text{VOXF-7}$  (i)  $-1/2+x, 1/2+y, z$  (ii)  $-1/2-x, 1/2-y, -z$  (iii)  $-x, 1-y, -z$ .

Bond	Distance (Å)	Bond	Distance (Å)
V1-O1	1.64(1)	V2-O2 <sup>i</sup>	1.92(1)
V1-O2	1.71(1)	V2-O3 <sup>ii</sup>	1.95(1)
V1-O3	1.74(1)	V2-O4	1.97(1)
V1-O4	1.84(1)	V2-O4 <sup>iii</sup>	1.98(1)
		V2-O5	1.61(1)

Most of the hydrogen bonding takes place between terminal oxygen atoms and 1,3-propylenediammonium cations, although some bridging oxygen atoms take part as well. This is shown in more detail in Figure 5.33.

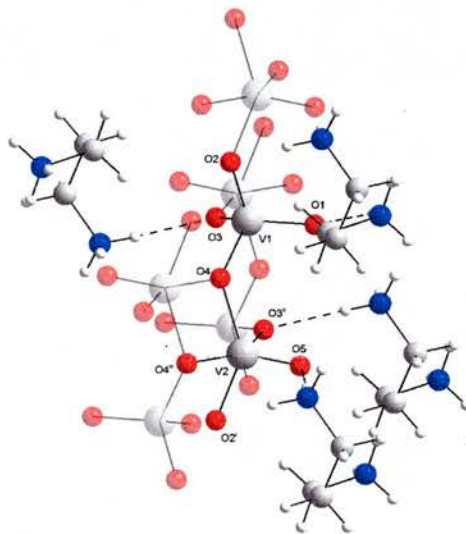


Figure 5.33: A closer look at the hydrogen bonding scheme of  $\text{VOXF-7}$ . (i)  $-1/2+x, 1/2+y, z$ ; (ii)  $-1/2-x, 1/2-y, -z$ ; (iii)  $-x, 1-y, -z$ .

Table 5.21 shows the hydrogen bonding in VOXF-7.

Table 5.21: Hydrogen bonds in VOXF-7 (i)  $-x, y, -z+1/2$  (ii)  $-x-1/2, -y+1/2, -z$  (iii)  $x-1/2, y-1/2, z$  (iv)  $-x-1/2, y-1/2, -z+1/2$ .

D	H	A	D-H (Å)	H...A (Å)	D...A (Å)	∠DHA (°)
N1	H1	O1 <sup>i</sup>	0.91	2.13	2.93(1)	147
N1	H2	O3 <sup>ii</sup>	0.91	2.02	2.91(1)	164
N1	H3	O5 <sup>iii</sup>	0.91	2.04	2.95(1)	176
N1	H3	O5 <sup>iv</sup>	0.91	2.64	3.10(1)	112

## 5.9 Concluding Remarks

A wide variety of vanadium oxyfluorides have been synthesised hydrothermally.

VOXF-1 consists of polar  $[\text{VOF}_4\text{H}_2\text{O}]^{2-}$  units, which align along the polar axis in  $P2_1$ . These vanadium atoms have a tendency to be displaced from the centre of the octahedron towards the vanadyl bond. It has a lower SHG activity and damage threshold than  $\text{LiNbO}_3$ . A centrosymmetric organic template molecule can arrange units into a polar direction, and the nature of the hydrogen bonding is very important.

The same polar  $[\text{VOF}_4\text{H}_2\text{O}]^{2-}$  units are also seen in VOXF-2, but they are arranged about a centrosymmetric cell. Similar displacement of the vanadium atom is also shown. Both VOXF-1 and VOXF-2 appear to be dehydrated to a stable condensed phase. These phases are currently unknown and this will require further investigation in the future.

VOXF-3 shows infinite chains of  $\text{VF}_6$  octahedra along the b-axis. The bridging V-F bond distances are 2 Å, and the terminal V-F bond distances are 1.9 Å. This satisfies the bond valence sums of these atoms.

VOXF-4 also shows infinite chains of  $\text{VF}_6$  octahedra, but these run along the c-axis. Two chains have eclipsed octahedra and the other two chains have staggered octahedra. This is isostructural to Sc-2, but the F-V-V-F torsion angle is wider than the scandium version.

VOXF-5 consists of cyclic  $[\text{V}_4\text{O}_4\text{F}_{14}]^{6-}$  tetramers. Each tetramer molecule hydrogen bonds with three of these tetramers to produce a complex hydrogen bonding framework. Each vanadium atom is displaced from the centre of the octahedron towards the vanadyl bond, which do not take part in hydrogen bonding.

VOXF-6 consists of  $[\text{V}_2\text{O}_2\text{F}_6(\text{H}_2\text{O})_2]^{2-}$  dimeric units surrounded by rotationally disordered diazoniumbicyclo[2.2.2]octane cations. The vanadium atom was displaced from the centre of each  $\text{VOF}_4(\text{H}_2\text{O})$  octahedron, towards the vanadyl bond and the water ligand.

VOXF-7 is a mixed valence oxide with  $\text{VO}_4$  tetrahedra and  $\text{VO}_5$  trigonal bipyramids, which corner- and edge-share to form layers separated by 1,3-propylenediammonium cations. It is structurally analogous to an existing polymorph of  $[\text{C}_3\text{N}_2\text{H}_{12}][\text{V}_4\text{O}_{10}]$ , except for a difference in the orientation of the 1,3-propylenediammonium cations, which *via* hydrogen bonding, causes a change in the orientation of the  $\text{VO}_4$  tetrahedra.

## References

- [1] R. Mattes and H. Foerster, *J. Solid State Chem.*, 1982, **45**, 154.
- [2] U. Bentrup, A. Ahmadi, H. C. Kang, and W. Massa, *Z. Anorg. Allg. Chem.*, 1998, **624**, 1465.
- [3] J. A. Swift and M. D. Ward, *Chem. Mater.*, 2000, **12**, 1501.
- [4] I. Bull, L. A. Villaescusa, S. J. Teat, M. A. Cambor, P. A. Wright, P. Lightfoot, and R. E. Morris, *J. Am. Chem. Soc.*, 2000, **122**, 7128.
- [5] M. E. Welk, A. J. Norquist, C. L. Stern, and K. P. Poeppelmeier, *Inorg. Chem.*, 2001, **40**, 5479.
- [6] L.-Q. Tang, M. S. Dadachov, and X.-D. Zou, *Z. Krist. New Cryst. Struct.*, 2001, **216**, 259.
- [7] L. Croguennec, P. Deinard, R. Brec, M. Couzi, C. Sourisseau, J. L. Fourquet, and Y. Calage, *J. Solid State Chem.*, 1997, **131**, 189.
- [8] M. Dadachov and L. Eriksson, *Acta Cryst. C*, 1999, **55**, 1739.

- [9] L. Croguennec, P. Deniard, R. Brec, M. Couzi, C. Sourisseau, J. L. Fourquet, and Y. Calage, *J. Solid State Chem.*, 1997, **131**, 189.
- [10] M. Dadachov and L. Eriksson, *Acta Cryst. C*, 1999, **55**, 1739.
- [11] T. S. Cameron, T. M. Klapotke, A. Schulz, and J. Valkonen, *J. Chem. Soc., Dalton Trans.*, 1993, p. 659.
- [12] C. R. Ross II, B. L. Paulsen, R. M. Nielson, and S. C. Abrahams, *Acta Cryst. B*, 1998, **54**, 417.
- [13] M. P. Crosnier-Lopez, H. Duroy, and J. L. Forquet, *Z. Anorg. Allg. Chem.*, 1993, **619**, 1597.
- [14] A. Demsar, I. Leban, and G. Giester, *Acta Chim. Slov.*, 2002, **49**, 259.
- [15] D. Riou and G. Férey, *J. Solid State Chem.*, 1995, **120**, 137.

# Chapter 6

## Miscellaneous

Several novel transition metal fluorides are described in this chapter and denoted misc-*n*. These range from 0-dimensional structures consisting of isolated MF<sub>6</sub> octahedra, through to dimeric units and complex 3-dimensional structures with MF<sub>8</sub> square antiprisms and MF<sub>9</sub> mono-capped square antiprisms.

Hydrothermal synthesis, X-ray diffraction, thermogravimetric analysis and CHN microanalysis experimental procedures were used in the work. X-ray data are shown in Table 6.1. All hydrogen atoms were refined riding upon their carrier atoms, unless otherwise stated. Atomic co-ordinates and temperature factors are tabulated in Appendix A in the file "Appendices.pdf" on the CD-ROM. Bond lengths and angles are tabulated in Appendix B.

Table 6.1: Crystallographic parameters of miscellaneous fluorides.

	Misc-1	Misc-2	Misc-3	Misc-4*
Formula	$[C_2N_2H_{10}]_{1.5}[TiF_6]F$	$[C_2N_2H_{10}]_2[Nb_2O_3F_8]$	$[C_2N_2H_{10}]_{0.5}[Y_2F_7]$	$[C_3N_2H_{12}]_{0.5}[Y_3F_{10}]$
Formula weight	548.16	510.06	341.88	
Crystal system	Monoclinic	Monoclinic	Orthorhombic	Cubic
Space group	$P2_1/c$	$P2_1/n$	Fddd	$Fd\bar{3}m$
$a(\text{\AA})$	13.270(4)	11.712(1)	8.017(3)	15.4187(1)
$b(\text{\AA})$	6.849(2)	10.198(1)	14.076(5)	
$c(\text{\AA})$	11.277(3)	11.971(1)	22.614(9)	
$\beta(^{\circ})$	108.81(6)	93.44(2)		
Volume( $\text{\AA}^3$ )	970.1(4)	1427.3(2)	2552(2)	
Crystal size (mm)	0.15 x 0.15 x 0.1	0.1 x 0.1 x 0.03	0.15 x 0.1 x 0.05	
Z	2	4	16	8
$\mu(\text{mm}^{-1})$	0.958	1.711	18.18	
Total reflections	1977	2608	589	
Observed reflections ( $I > 2\sigma(I)$ )	1683	2419	467	
$R_1, wR_2$ ( $I > 2\sigma(I)$ )	0.04, 0.13	0.02, 0.06	0.05, 0.11	
$R_1, wR_2$ (all data)	0.06, 0.22	0.03, 0.06	0.06, 0.12	

\* X-ray powder diffraction data:  $R_{wp} = 0.097$ ,  $\chi^2 = 14.4$ , for 10500 data points, 236 contributing reflections, 9 restraints and 31 variables, with  $2\theta$  from 5 to  $110^{\circ}$ .

## 6.1 [C<sub>2</sub>N<sub>2</sub>H<sub>10</sub>]<sub>1.5</sub>[TiF<sub>6</sub>]F (misc-1)

### 6.1.1 Experimental

### 6.1.2 Synthesis

0.08 g of TiO<sub>2</sub>, 5 ml of water and 0.75 ml of a 40 % solution of HF was heated in a Teflon lined steel autoclave for one hour at 100 °C. To this solution, 5 ml of ethylene glycol and 0.5 ml of ethylenediamine was added and heated for six days at 190 °C. The pH of the solution changed from 3 to 7 throughout. The solution was left to evaporate over two weeks. Off white aggregations were collected and washed in acetone. From these, a single crystal suitable for analysis was collected. (Found: C, 13.05 %; H, 5.52 %; N, 15.31 %. [C<sub>2</sub>N<sub>2</sub>H<sub>10</sub>]<sub>1.5</sub>[TiF<sub>6</sub>]F requires C, 13.15 %; H, 5.52 %; N, 15.33 %.) CHN microanalysis showed that a lone F<sup>-</sup> anion is present, since there is little discrepancy between the observed and calculated values. There is a possibility that this anion is a water molecule, but there is no hydrogen bonding between this location and the [TiF<sub>6</sub>]<sup>2-</sup> anion. Attempts to refine the F<sup>-</sup> anion site as a water molecule failed. According to the software CheckCIF, the data set is only 80 % complete.

A TGA plot of misc-1 was taken from room temperature to 600 °C, at a heating rate of 5 °C min<sup>-1</sup> under an atmosphere of N<sub>2</sub>.

### 6.1.3 Discussion

#### Structure

$[\text{C}_2\text{N}_2\text{H}_{10}]_{1.5}[\text{TiF}_6]\text{F}$  consists of isolated  $\text{TiF}_6$  octahedra, ethylenediammonium cations and  $\text{F}^-$  anions.

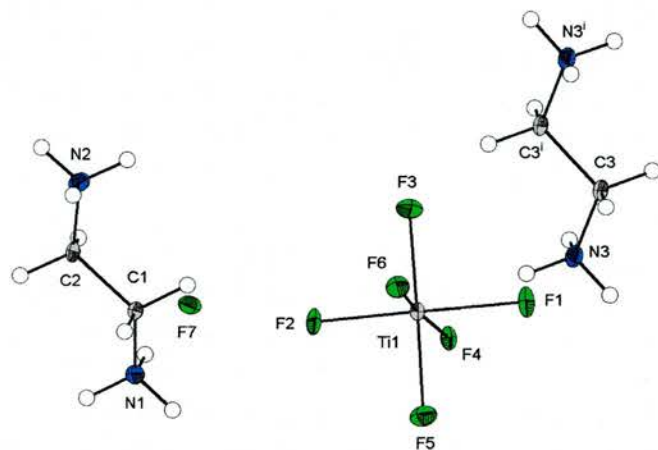
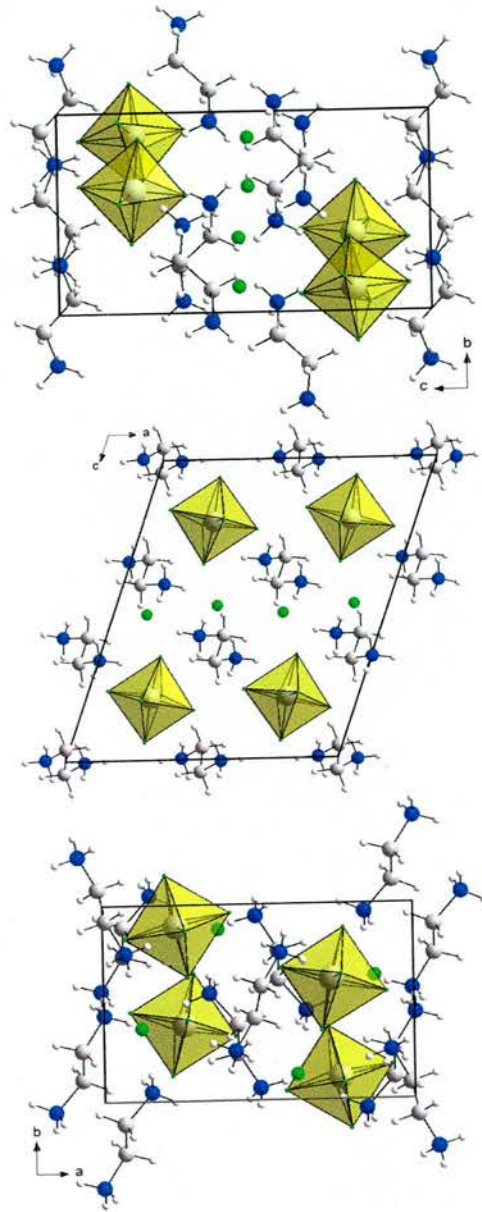


Figure 6.1: An ORTEP diagram of misc-1 with displacements at 50 % probability (arbitrary spheres for the H atoms) (i) 1-x, 1-y, -z.

Figure 6.2 shows the structure of misc-1 along each principal axis.



*Figure 6.2: misc-1 along the a-, b- and c-axis.*

A hydrogen bonding scheme of misc-1 is shown in Figure 6.3.

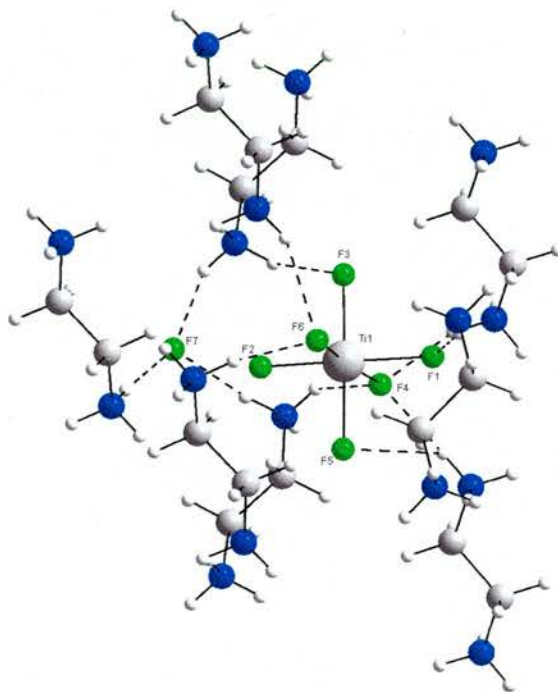


Figure 6.3: The hydrogen bonding scheme of misc-1.

Only five F atoms are hydrogen bonded to ethylenediammonium cations. The lone F<sup>-</sup> anion is hydrogen bonded by three ethylenediammonium cations. F4 experiences hydrogen bonding from three donors, so the Ti1-F4 bond distance is longer than the others. The underbonding is shown by the bond valence. *Trans* to this bond, F6 is only hydrogen bonded by one donor. F1 experiences similar hydrogen bonding, while F2 does not experience any hydrogen bonding at all. There is also a very short H...F distance of 2.18 Å, which may be the shortest known.

Table 6.2 shows all of the hydrogen bonding in this system.

Table 6.2: Hydrogen bonds in misc-1 (i)  $-x+1, y+1/2, -z+1/2$ , (ii)  $-x+1, -y+1, -z$ , (iii)  $-x+1, -y, -z$ , (iv)  $x, y-1, z$ , (v)  $-x+1, y-1/2, -z+1/2$ , (vi)  $-x+2, y+1/2, -z+1/2$ , (vii)  $x, -y+1/2, z-1/2$ .

D	H	A	D-H (Å)	H-A (Å)	D-A (Å)	∠ DHA (°)
N1	H1a	F4 <sup>i</sup>	0.91	2.16	2.89(1)	137
N1	H1a	F6 <sup>ii</sup>	0.91	2.23	2.97(1)	138
N1	H1b	F7 <sup>ii</sup>	0.91	2.29	2.79(1)	114
N1	H1b	F5 <sup>iii</sup>	0.91	2.53	3.12(1)	123
N1	H1c	F7	0.91	1.78	2.67(1)	167
N2	H2c	F7 <sup>iv</sup>	0.91	1.82	2.67(1)	155
N2	H2d	F3 <sup>v</sup>	0.91	2.30	2.98(1)	132
N2	H2d	F6 <sup>iii</sup>	0.91	2.34	3.01(1)	130
N2	H2e	F7 <sup>v</sup>	0.91	1.76	2.64(1)	162
N3	H3a	F4 <sup>vi</sup>	0.91	2.00	2.90(1)	168
N3	H3a	F5 <sup>vi</sup>	0.91	2.48	3.02(1)	119
N3	H3a	F1 <sup>vi</sup>	0.91	2.54	3.14(1)	124
N3	H3b	F1	0.91	1.84	2.72(1)	163
N3	H3c	F4 <sup>vii</sup>	0.91	1.90	2.78(1)	163

Table 6.3 shows bond lengths and bond valence sums for each atom around the TiF<sub>6</sub> octahedron.

Table 6.3: Selected bond distances of misc-1.

Bond	Distance (Å)	Bond	Distance (Å)
Ti-F1	1.88(2)	Ti-F4	1.93(2)
Ti-F2	1.83(2)	Ti-F5	1.84(2)
Ti-F3	1.85(2)	Ti-F6	1.84(2)

The BVS of the Ti atom is 4.59, much higher than expected for Ti<sup>4+</sup>. These are shown in Table 6.4. This is due to a R<sub>0</sub> value of 1.76 Å from the work done by Brese and O'Keeffe [1] used in VaList [2].

Table 6.4: Bond valence sums of *misc-1* with  $R_0 = 1.76$ .

Atom	$\Sigma s_{ij}$	Atom	$\Sigma s_{ij}$
Ti1	4.59	F4	0.63
F1	0.72	F5	0.80
F2	0.84	F6	0.81
F3	0.79		

Using VALENCE [3], this parameter is 1.72 Å and produces a BVS of 4.01. This software uses the  $R_0$  values from work by Brese, O’Keeffe, Brown and Altermatt [4]. Table 6.5 shows the bond valences with this alternative  $R_0$ . When  $\text{Cu}(\text{pyz})(\text{H}_2\text{O})_2\text{TiF}_6$  [5] is analysed with VaList, the BVS is 4.64. VALENCE puts the value at 4.14.

Table 6.5: Bond valence sums of *misc-1* with  $R_0 = 1.718$ .

Atom	$\Sigma s_{ij}$	Atom	$\Sigma s_{ij}$
Ti1	4.09	F4	0.56
F1	0.65	F5	0.72
F2	0.74	F6	0.72
F3	0.70		

The Ti atom is displaced from the centre of the octahedron towards F6. This is shown in Figure 6.4. This is due to the  $d^0$  electronic configuration of the  $\text{Ti}^{4+}$  cation.

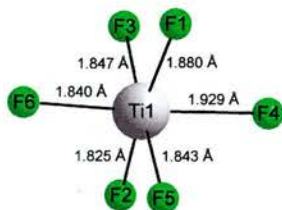


Figure 6.4: The  $\text{TiF}_6$  octahedron found in  $[\text{C}_2\text{N}_2\text{H}_{10}]_{1.5}[\text{TiF}_6]\text{F}$  showing bond distances.

The  $\text{TiF}_6$  octahedra present in  $\text{TiF}_4$  [6] shows a larger displacement of the Ti cation than in misc-1.  $\text{TiF}_4$  consists of corner-sharing  $\text{TiF}_6$  octahedra, which connect together to form three-membered rings. These extend along the b-axis to produce  $[\text{Ti}_3\text{F}_{15}]^{3-}$  chains. This is shown in Figure 6.5. The displacement is towards one edge because of the linking F atoms, causing the *trans* Ti-F bond to be shortened so the Ti atom retains its proper valence.

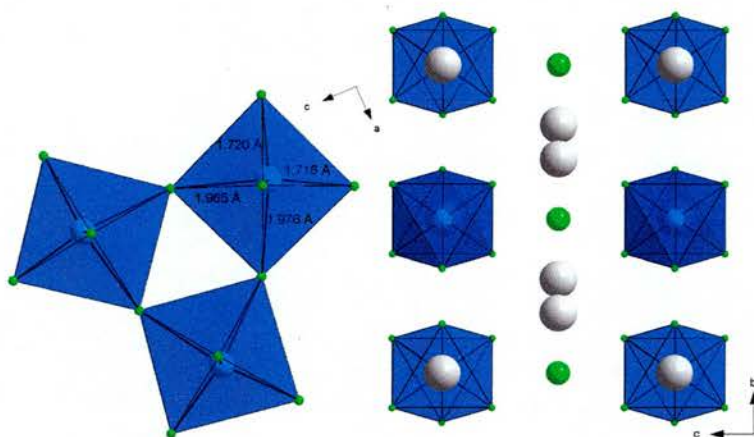


Figure 6.5: The 3-membered ring system in  $\text{TiF}_4$  (left) and  $\text{Cs}_3\text{TiF}_7$  along the c-axis with  $\text{Cs}^+$  in grey and  $\text{F}^-$  in green (right).

Individual  $\text{F}^-$  anions occupying spaces between  $\text{TiF}_6$  octahedra also occurs in the tetragonal  $\text{Cs}_3\text{TiF}_7$  [7]. This is also shown in Figure 6.5. It consists of isolated  $\text{TiF}_6$  octahedra and is similar to misc-1, because of the way the isolated  $\text{F}^-$  anions align in between the  $\text{TiF}_6$  octahedra. The  $\text{TiF}_6$  octahedra do not show any second order Jahn-Teller effects and the BVS (3.89) is close to the expected value of 4.

$\text{NH}_4\text{CuTiF}_7(\text{H}_2\text{O})_4$  [8] consists of infinite chains constructed of alternating  $\text{TiF}_6$  and  $\text{CuO}_4\text{F}_2$  octahedra. Each chain is staggered in a similar fashion to Sc-2 by  $10.6^\circ$ . Chains of ammonium cations are also interrupted by  $\text{F}^-$  anions. This is shown in Figure 6.6.

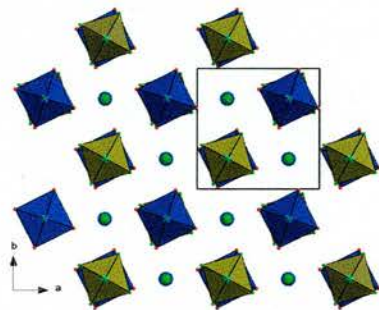


Figure 6.6:  $\text{NH}_4\text{CuTiF}_7(\text{H}_2\text{O})_4$  along the  $c$ -axis, with  $\text{TiF}_6$  octahedra in yellow,  $\text{CuO}_2\text{F}_4$  octahedra in blue,  $\text{NH}_4^+$  cations in blue and  $\text{F}^-$  anions in yellow.

$\text{Ni}_3(\text{py})_{12}\text{F}_6 \cdot 7\text{H}_2\text{O}$  [9] is shown in Figure 6.7. Each N atom is in a pseudo-square planar arrangement. The crystal packing produces chains, which hydrogen bond via lattice water molecules.

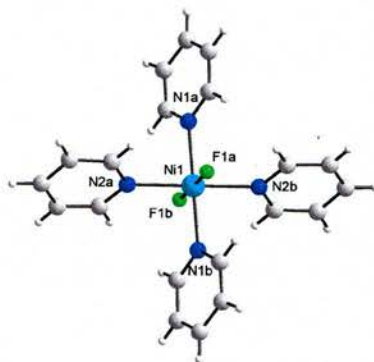


Figure 6.7: A single isolated unit in  $\text{Ni}_3(\text{py})_{12}\text{F}_6 \cdot 7\text{H}_2\text{O}$ .

## Thermogravimetric Analysis

Figure 6.8 shows a TGA plot of misc-1.

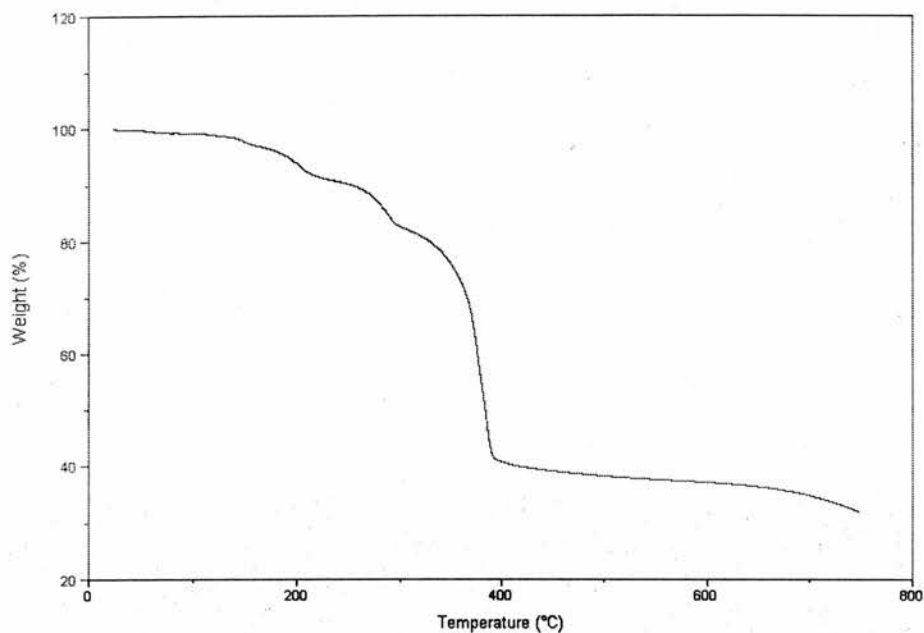


Figure 6.8: The TGA plot of  $[C_2N_2H_{10}]_{1.5}[TiF_6]F$ .

Under  $N_2$ , the weight loss is split into four steps, from 100 to 150 °C, 150 to 200 °C, 200 to 300 °C and from 300 to 390 °C. It is unclear what these steps represent.

An X-ray powder diffraction of the TGA residue however, shows a presence of  $TiF_3$  (PDF no. 9-112) and the polymorphs of  $TiO_2$ , anatase (PDF no. 21-1272) and rutile (PDF no. 21-1276), shown in Figure 6.9. This implies a presence of these polymorphs in the starting material. The TGA was performed on the bulk sample and not single crystals.

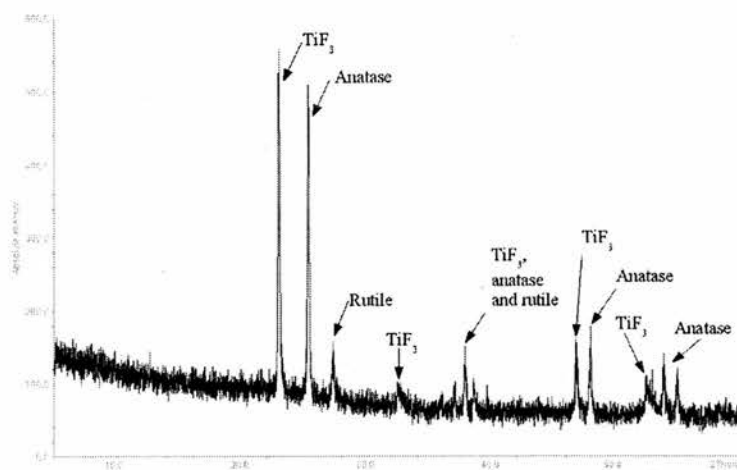


Figure 6.9: An X-ray powder diffraction of the TGA residue.

## 6.2 $[\text{C}_2\text{N}_2\text{H}_{10}]_2[\text{Nb}_2\text{O}_3\text{F}_8]$ (misc-2)

### 6.2.1 Experimental

#### Synthesis

0.2658 g of  $\text{Nb}_2\text{O}_5$ , 5 ml of  $\text{H}_2\text{O}$  and 0.5 ml of a 40 % solution of HF was heated in a polypropylene bottle at 100 °C for 1 hour. The contents of the bottle were washed into a Teflon lined steel autoclave with 5 ml ethylene glycol. To that, 0.25 ml ethylenediamine was added to give a pH of 4. This was heated at 190 °C for 5 days. The pH increased to 6.5 over this time. The product was in the form of colourless prisms, and they were washed, filtered and allowed to dry at room temperature (Found: C, 8.62 %; H, 3.45 %; N, 9.26 %.  $[\text{C}_2\text{N}_2\text{H}_{10}]_2[\text{Nb}_2\text{O}_3\text{F}_8]$  requires C, 9.42 %; H, 3.95 %; N, 10.99 %.) The slight discrepancy may be due to unreacted starting materials.

## Characterisation

TGA was carried out on misc-2 from room temperature to 600 °C under an atmosphere of N<sub>2</sub>.

### 6.2.2 Discussion

#### Structure

Figure 6.10 shows [Nb<sub>2</sub>O<sub>3</sub>F<sub>8</sub>]<sup>4-</sup> dimers and ethylenediammonium cations. The [Nb<sub>2</sub>O<sub>3</sub>F<sub>8</sub>]<sup>4-</sup> dimers are made up of one NbO<sub>2</sub>F<sub>4</sub> octahedron linked to another *via* O3.

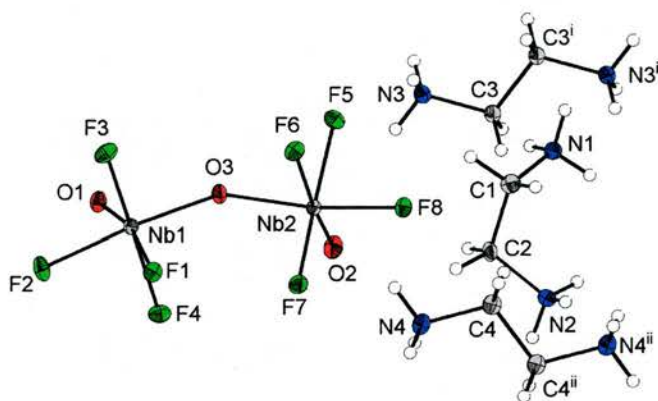
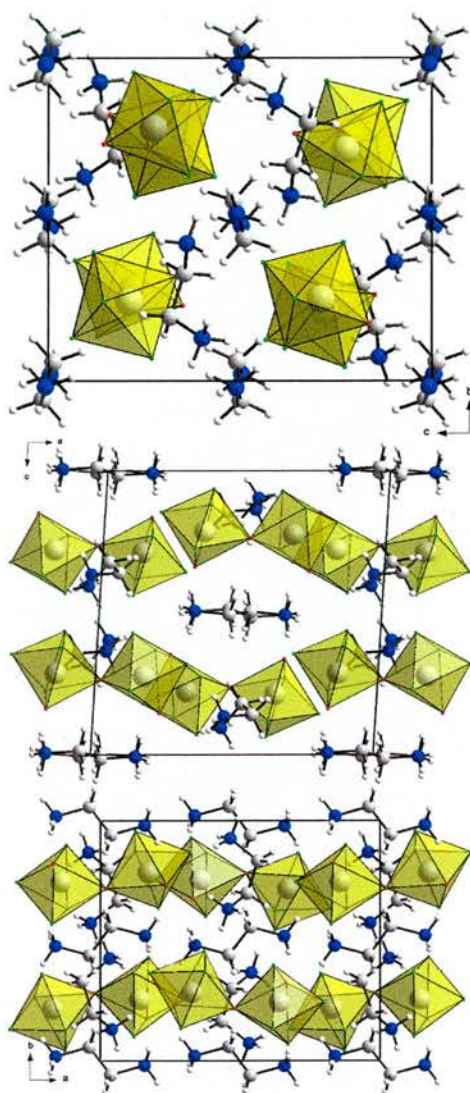


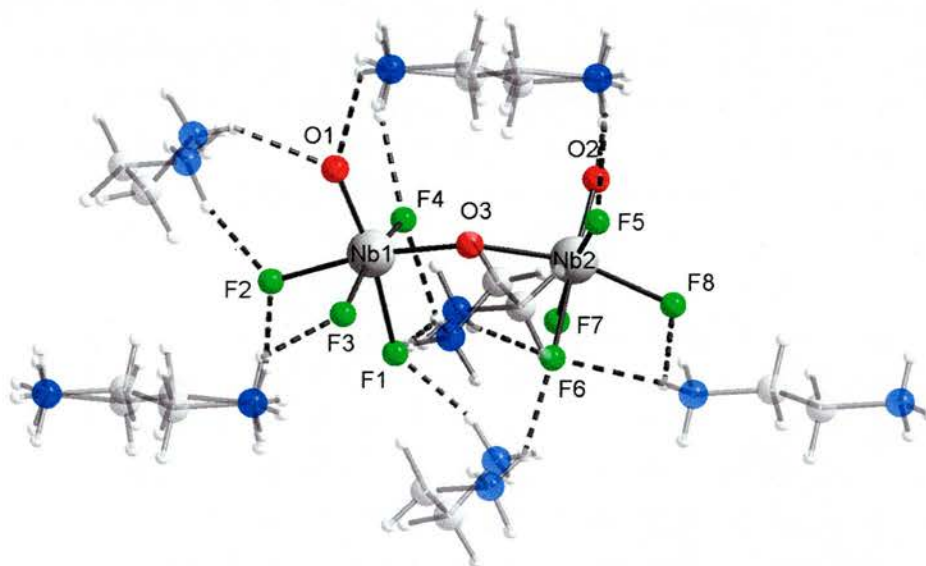
Figure 6.10: An ORTEP diagram of [C<sub>2</sub>N<sub>2</sub>H<sub>10</sub>]<sub>2</sub>[Nb<sub>2</sub>O<sub>3</sub>F<sub>8</sub>] with thermal ellipsoids at 50 % probability (arbitrary spheres for the H atoms) (i) 1-x, 1-y, 1-z (ii) 1-x, -y, 1-z.

Figure 6.11 shows the dimers with the ethylenediammonium cations viewed along the three principle crystallographic axes. The dimers point up and down in a herringbone pattern along the c-axis.



*Figure 6.11: Misc-2 along the a-, b- and axis.*

Figure 6.12 shows the hydrogen bonding scheme of misc-2, with the ethylenediammonium cations shaded for clarity. The Nb atoms have a tendency to be displaced from the centre of the  $\text{NbO}_2\text{F}_4$  octahedron towards the terminal and the bridging O atoms.



*Figure 6.12: The hydrogen bonding scheme of misc-2.*

A table of hydrogen bonds is shown in Table 6.6.

*Table 6.6: Hydrogen bonds in misc-2*

D	H	A	D-H (Å)	H-A (Å)	D-A (Å)	∠ DHA (°)
N1	H9	F1 <sup>i</sup>	0.91	2.05	2.83(1)	142
N1	H10	F1 <sup>ii</sup>	0.91	1.82	2.70(1)	160
N1	H9	F4 <sup>t</sup>	0.91	2.17	2.92(1)	140
N1	H11	O1 <sup>iii</sup>	0.91	2.04	2.83(1)	144
N1	H11	F6 <sup>ii</sup>	0.91	2.59	3.22(1)	127
N2	H12	F6 <sup>iv</sup>	0.91	2.02	2.86(1)	153
N2	H12	O3 <sup>iv</sup>	0.91	2.63	3.22(1)	123
N2	H13	F2 <sup>iii</sup>	0.91	1.93	2.75(1)	150
N2	H14	F6 <sup>ii</sup>	0.91	1.87	2.69(1)	148
N3	H15	F6	0.91	2.13	2.89(1)	140
N3	H15	F8	0.91	2.16	2.86(1)	133
N3	H16	O2 <sup>i</sup>	0.91	1.83	2.72(1)	164
N3	H17	F4 <sup>v</sup>	0.91	2.03	2.78(1)	139
N3	H17	F3 <sup>vi</sup>	0.91	2.09	2.79(1)	133
N4	H18	O1 <sup>v</sup>	0.91	2.32	3.01(1)	132
N4	H18	F8	0.91	2.37	2.91(1)	118
N4	H18	F7	0.91	2.40	2.93(1)	117
N4	H19	F2 <sup>vii</sup>	0.91	1.87	2.76(1)	165
N4	H19	F1 <sup>vii</sup>	0.91	2.53	3.11(1)	122
N4	H20	F5 <sup>iv</sup>	0.91	1.90	2.79(1)	165

Bond distances around each dimeric unit is shown in Table 6.7. The long Nb2-F6 bond is a result of hydrogen bonding from an ethylenediammonium cation and the *trans* effect from the Nb=O bond. The terminal O atoms show similar behaviour.

Table 6.7: Selected bond distances of *misc-2*.

Bond	Distance (Å)	Bond	Distance (Å)
Nb1-O1	1.77(1)	Nb2-O2	1.74(1)
Nb1-O3	1.91(1)	Nb2-O3	1.94(1)
Nb1-F1	2.10(1)	Nb2-F5	1.97(1)
Nb1-F2	2.06(1)	Nb2-F6	2.17(1)
Nb1-F3	1.94(1)	Nb2-F7	1.95(1)
Nb1-F4	1.97(1)	Nb2-F8	1.98(1)

All of the ligand atoms show underbonding, some more than others and this is expressed in the hydrogen bonding scheme. All ligand atoms require hydrogen bonding except for the linking oxygen atom.

Table 6.8: Bond valence sums of *misc-2*.

Atom	$\Sigma s_{ij}$	Atom	$\Sigma s_{ij}$
Nb1	5.22	F3	0.82
Nb2	5.30	F4	0.77
O1	1.48	F5	0.76
O2	1.61	F6	0.44
O3	1.95	F7	0.81
F1	0.54	F8	0.74
F2	0.60		

This is the first example of an organically templated niobium oxyfluoride. Isolated  $[\text{NbOF}_5]^{2-}$  units have already been found in  $\text{Li}_2\text{NbOF}_5$  [10], with  $\text{NbF}_7$  and  $\text{NbOF}_6$  units found in  $\text{Rb}_5\text{Nb}_3\text{OF}_{18}$ [11] and  $\text{Ba}_4\text{Nb}_2\text{O}_3\text{F}_{12}$ [12]. These are shown in Figure 6.13.

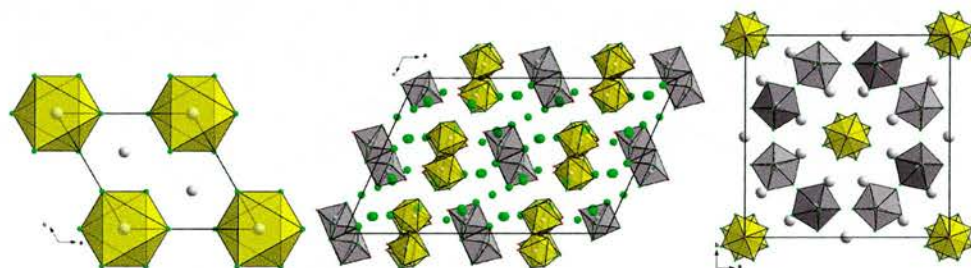
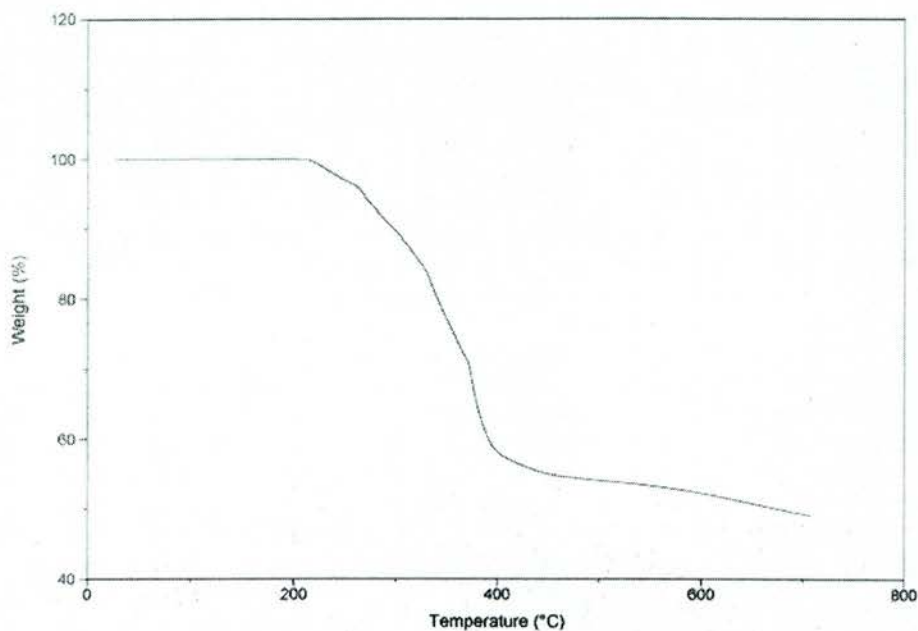


Figure 6.13:  $\text{Li}_2\text{NbOF}_5$  (left),  $\text{Ba}_4\text{Nb}_2\text{O}_3\text{F}_{12}$  (centre) and  $\text{Rb}_5\text{Nb}_3\text{OF}_{18}$  (right).

Other examples are  $\text{NbF}_6$  octahedra co-ordinated to two Cu complexes[13] and isolated  $\text{NbF}_6$  octahedra templated by Cu complexes[14]. In the first example, the linking F atom is displaced towards the Nb atom due to the Jahn-Teller distortion of the  $\text{Cu}^{2+}$  cation. In the isolated case, all of the Nb-F bond distances are equal to each other.

## Thermogravimetric Analysis

A TGA plot of misc-2 is shown in Figure 6.14.



*Figure 6.14: A TGA plot of misc-2.*

Under  $N_2$ , one weight loss of 51 % occurs from 200 to 450 °C, which may be composed of four unresolvable steps. Therefore, it is unclear what the intermediate decomposition products are.

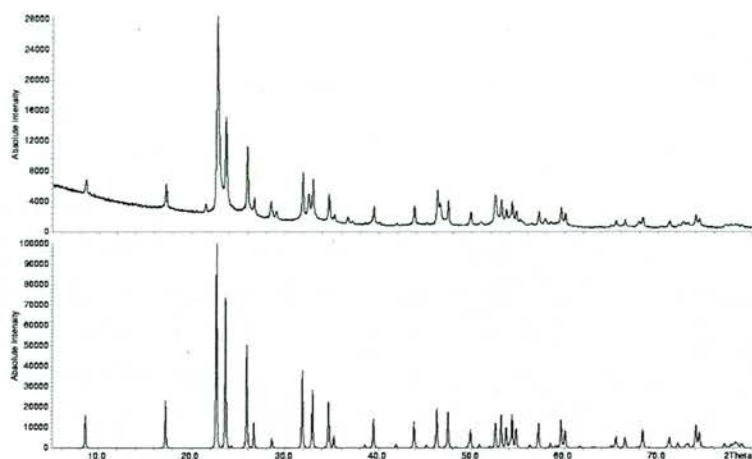


Figure 6.15: Powder X-ray patterns of the TGA residue and  $Nb_3O_7F$ .

According to XRD, the residue is  $Nb_3O_7F$  (PDF no. 74-2363). This is shown in Figure 6.15, where the X-ray powder diffraction pattern above corresponds to the residue and the pattern below is a simulated powder pattern of  $Nb_3O_7F$ .

The structure of  $Nb_3O_7F$  is shown in Figure 6.16.

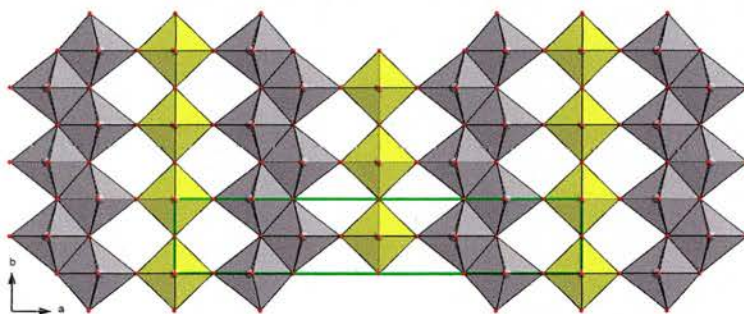


Figure 6.16: The structure of  $Nb_3O_7F$ .

It consists of two layers of edge-sharing double octahedra, which are bridged by  $\text{NbO}_6$  octahedra. This, in many ways is reminiscent of Sc-5. Table 6.9 shows how the cell parameters are related to Sc-5 and  $\text{KSc}_2\text{F}_7$ .

Table 6.9: The cell parameters of  $\text{KSc}_2\text{F}_7$ , Sc-5 and  $\text{Nb}_3\text{O}_7\text{F}$ .

	$\text{KSc}_2\text{F}_7$	Sc-5	$\text{Nb}_3\text{O}_7\text{F}$
a(Å)	10.643(2)	18.501(12)	20.67
b(Å)	6.54(1)	6.613(5)	3.833
c(Å)	4.03(1)	4.025(3)	3.927
Space group	Cmmm	Cmmm	Cmmm

As mentioned in Chapter 4, Sc-5 shares a resemblance with  $\text{KSc}_2\text{F}_7$ . Layers of  $\text{ScF}_7$  pentagonal bipyramids are separated by  $\text{ScF}_6$  octahedra, creating “butterfly” channels. In the case of  $\text{Nb}_3\text{O}_7\text{F}$ , layers of double octahedra are separated in a similar way, except for the absence of the “butterfly” channels.

## 6.3 $[\text{C}_2\text{N}_2\text{H}_{10}]_{0.5}[\text{Y}_2\text{F}_7]$ (misc-3)

### 6.3.1 Experimental

#### Synthesis

0.0383 g of  $\text{Y}(\text{NO}_3)_6 \cdot 6\text{H}_2\text{O}$ , 5 ml  $\text{H}_2\text{O}$  and 2 ml HF was heated in a polypropylene bottle at 100 °C for 1 hour. The contents were transferred to a Teflon lined steel autoclave and any remaining residue was washed into the autoclave with 5 ml ethylene glycol. 1.25 ml ethylenediamine was added to give a gel with pH of 6. This was heated at 180 °C for 5 days. The pH remained constant through the reaction. The prismatic crystals obtained were washed in water, filtered and dried at room temperature (Found: C, 3.55 %; H, 1.08 %; N, 3.97 %.  $[\text{C}_2\text{N}_2\text{H}_{10}]_{0.5}[\text{Y}_2\text{F}_7]$  requires C, 3.51 %; H, 1.47 %; N, 4.1 %.)

TGA was carried out on the sample from room temperature to 750 °C, at a heating rate of 5 °C  $\text{min}^{-1}$  under  $\text{N}_2$ .

## 6.3.2 Discussion

### Structure

The structure of misc-3 consists of  $YF_8$  square antiprisms and  $YF_9$  mono-capped square antiprisms.

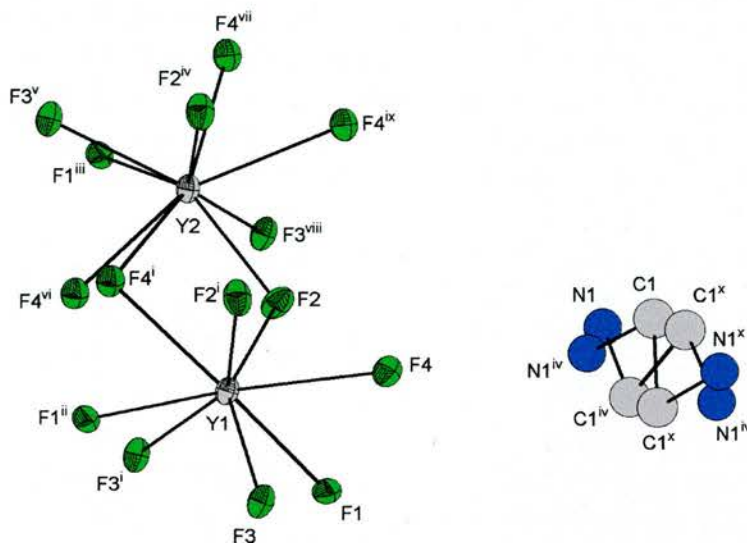


Figure 6.17: An ORTEP diagram of misc-3 with thermal ellipsoids at 50% probability (arbitrary spheres for the H atoms) (i)  $1/4-x, y, 1/4-z$  (ii)  $-1/2+y, 3/4-y, 1/4-z$  (iii)  $1/4-x, 1/4+y, -1/4+z$  (iv)  $1/4-x, 5/4-y, z$  (v)  $1/4+x, 1-y, 1/4+z$  (vi)  $-1/4+x, 1-y, -1/4+z$  (vii)  $1/2-x, -1/4+y, 1/4+z$  (viii)  $1/2-x, -1/4+y, 1/2+z$  (ix)  $x, 5/4-y, 1/4-z$  (x)  $x, 5/4-y, 5/4-z$ .

The ethylenediammonium cations were disordered in two equivalent positions about a site of 222 symmetry. In the refinement, the molecule was split into the two alternative conformations. This is the first example of an organically templated yttrium fluoride.

A hydrogen bonding scheme is shown in Figure 6.18. Each N atom hydrogen bonds to three F atoms and the organic cation lies inside a cavity.

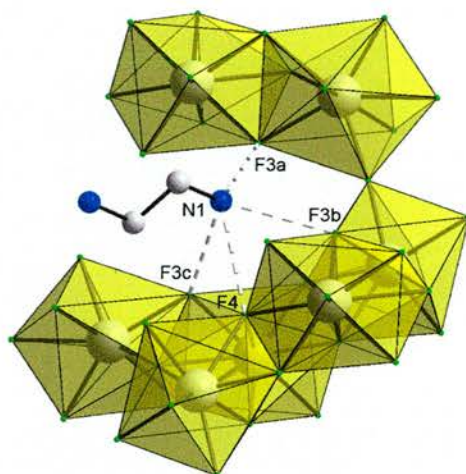


Figure 6.18: The hydrogen bonding of *misc-3* omitting hydrogen atoms.

Hydrogen bonds are tabulated in Table 6.10

Table 6.10: Hydrogen bonds in *misc-3* (i)  $x+1/4, -y+1, z+1/4$ , (ii)  $-x+1/4, y+1/2, -z+3/4$ , (iii)  $-x, y+1/4, z+1/4$ , (iv)  $x-1/2, -y+5/4, -z+3/4$ .

D	H	A	D-H (Å)	H-A (Å)	D-A (Å)	∠ DHA (°)
N1	H2	F3 <sup>i</sup>	0.91	2.30	2.79(2)	113
N1	H2	F3 <sup>ii</sup>	0.91	2.34	2.96(2)	125
N1	H3	F3 <sup>iii</sup>	0.91	2.11	2.92(2)	147
N1	H3	F4 <sup>iv</sup>	0.91	2.45	2.97(1)	116

Table 6.11 shows the bond distances around the  $YF_8$  square antiprisms and the  $YF_9$  mono-capped square antiprisms.

Table 6.11: Bond distances in misc-3; (i)  $x-1/4, -y+1, z-1/4$ , (ii)  $x, -y+5/4, -z+1/4$ , (iii)  $-x+1/2, y+1/4, z-1/4$ .

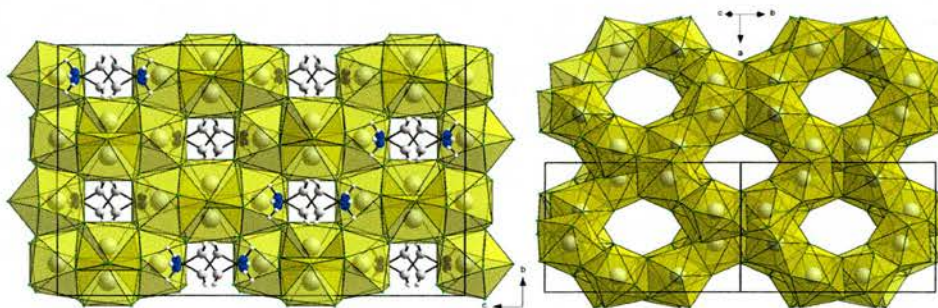
Bond	Distance (Å)	Bond	Distance (Å)
Y1-F1 x2	2.23(1)	Y2-F2 x2	2.21(1)
Y1-F2 x2	2.20(1)	Y2-F3 x2	2.23(1)
Y1-F3 x2	2.26(1)	Y2-F4 <sup>i</sup> x2	2.33(1)
Y1-F4 x2	2.41(1)	Y2-F4 <sup>ii</sup> x2	2.42(1)
		Y2-F1 <sup>iii</sup>	2.68(1)

Table 6.12 shows the bond valence sums of misc-3. F3 and F4 are slightly underbonded than the other F atoms, and these are hydrogen bonded by the ethylenediammonium cations.

Table 6.12: Bond valence sums in misc-3.

Atom	$\Sigma s_{ij}$	Atom	$\Sigma s_{ij}$
Y1	3.00	F2	0.88
Y2	2.94	F3	0.80
F1	0.94	F4	0.82

Because of the large co-ordination number of the yttrium atoms, and the relatively large number of symmetry operations, a very complicated structure is produced (Figure 6.19). It can however, be reduced into more simple motifs.



*Figure 6.19: Two views of misc-3.*

Figure 6.20 shows the 4-membered ring window produced by two edge sharing  $YF_8$  square antiprisms and two edge sharing  $YF_9$  mono capped square antiprisms. The disordered ethylenediammonium cation lies behind this window.

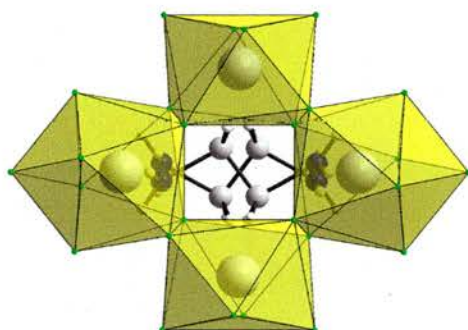


*Figure 6.20: The 4-membered ring window.*

Another structural motif present is a linear chain of *cis* corner connected  $YF_8$  square antiprisms shown in Figure 6.21. The chain runs along the a-axis, and forms part of a larger helical chain.

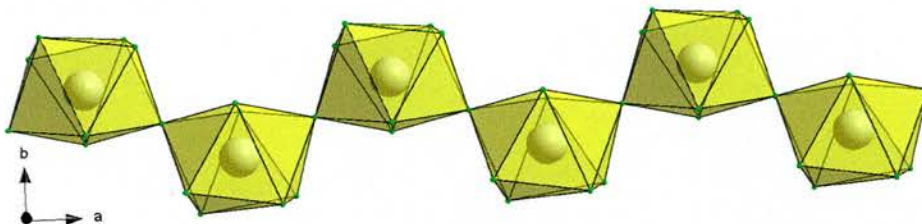


Figure 6.21: The *cis* chain found in *misc-3*.

The helical chain shown in Figure 6.22 consists of a single  $YF_8$  square antiprism face sharing with a  $YF_9$  mono capped square antiprism. This lies on the 2-fold screw axis, creating the helical chain. The *cis* chain already mentioned forms part of this helical chain, where parts of the *cis*-chain is highlighted in blue.

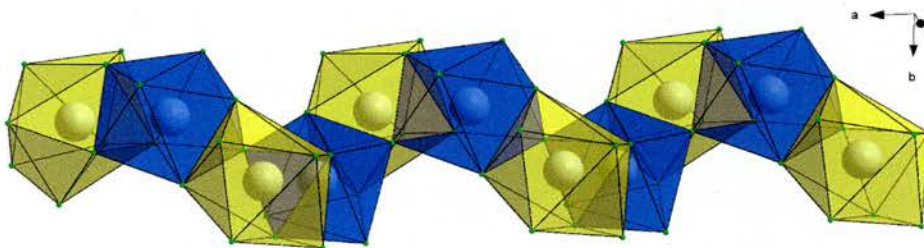


Figure 6.22: The helical chain found in *misc-3*.

It can be argued that these structural motifs are held together by another chain, which runs along the  $[110]$  direction, which consists of the  $YF_9$  monocapped square antiprisms sharing an edge with one another.

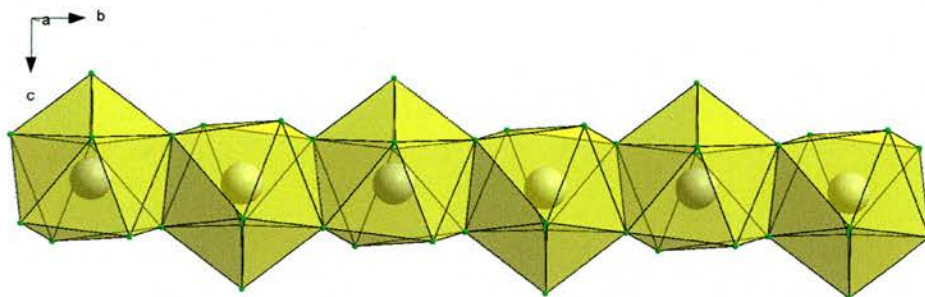


Figure 6.23: The edge-sharing chain found in *misc-3*.

Yttrium can be six co-ordinate in  $Rb_2KYF_6$ [15], but the most common co-ordination is eight.  $YF_8$  square antiprisms have been seen in  $Ba_4Y_3F_{17}$ , which exhibits edge-sharing and corner-sharing only [16]. It is more usual for eight co-ordinate yttrium polyhedra to conform to  $YF_8$  cubes in  $YF_3$ , but a square antiprism polymorph also exists[17]. These are shown in Figure 6.24.

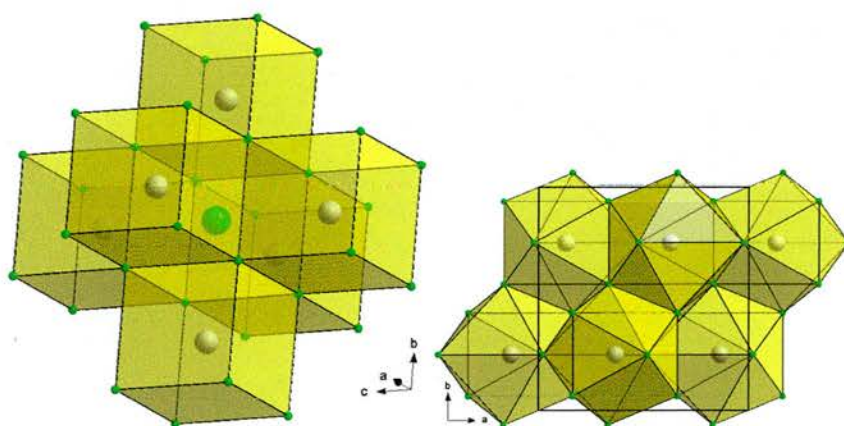


Figure 6.24: The two polymorphs of  $YF_3$ .

## Thermogravimetric analysis

The TGA plot of misc-3 is shown in Figure 6.25.

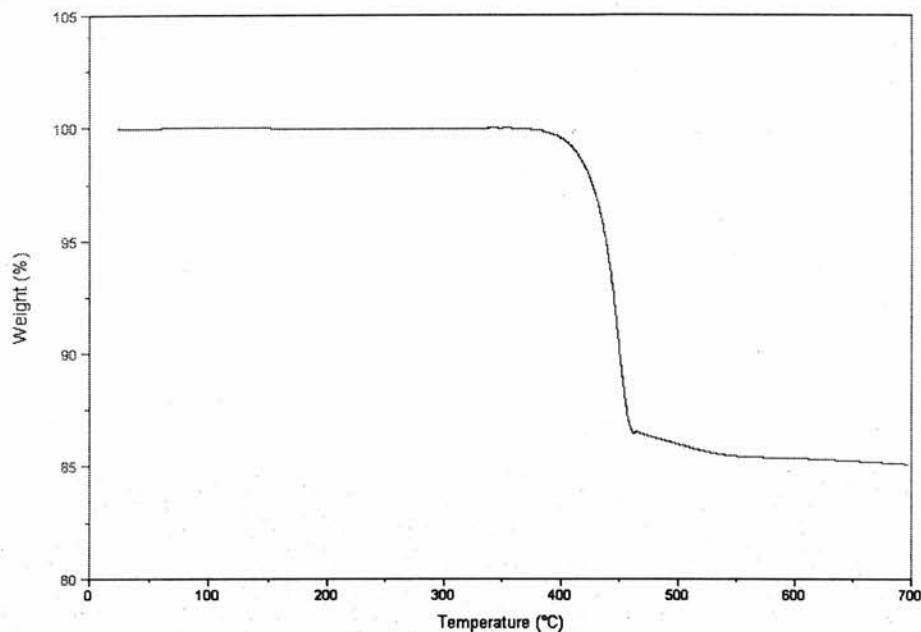


Figure 6.25: The TGA plot of misc-3.

Under  $N_2$ , a single step weight loss occurs from 375 to 460 °C, which corresponds to a loss of the organic template and HF (observed 14.7 %, calculated 14.6 %). This produces  $YF_3$  (PDF no. 32-1431), which was confirmed by powder XRD of the residue.

Inorganic lanthanide fluorides and lanthanide-doped yttrium fluorides are known for their excellent luminescent properties [18][19], and this work can pave the way for novel hybrid materials.

## 6.4 $[\text{C}_3\text{N}_2\text{H}_{12}]_{0.5}[\text{Y}_3\text{F}_{10}]$ (misc-4)

### 6.4.1 Experimental

#### Synthesis

0.0383 g of  $\text{Y}(\text{NO}_3)_3 \cdot 6\text{H}_2\text{O}$ , 5 ml of  $\text{H}_2\text{O}$  and 2 ml of a 40 % solution of HF was heated in a polypropylene bottle at 100 °C for 1 hour. The contents were transferred to a Teflon lined steel autoclave and any remaining residue was washed to the autoclave with 5 ml ethylene glycol. 1.5 ml of 1,3-propylenediamine was added to give a pH 6. This was heated at 180 °C for 5 days. The pH remained constant throughout the reaction. A white powder was washed in water, filtered and dried at room temperature. Subsequent attempts to synthesise crystals suitable for single crystal X-ray analysis failed (Found: C, 3.73 %; H, 1.21 %; N, 2.97 %.  $[\text{C}_3\text{N}_2\text{H}_{12}]_{0.5}[\text{Y}_3\text{F}_{10}]$  requires C, 3.64 %; H, 1.22 %; N, 2.83 %).

#### Characterisation

Powder X-ray data were collected on a Stoe STADI/P transmission diffractometer using  $\text{CuK}_{\alpha 1}$  radiation. The pattern was indexed with the Visser algorithm using the first twenty diffraction maxima. A face-centred cubic cell with  $a = 15.48 \text{ \AA}$  was found with a figure of merit,  $F_{20} = 163$ . A resemblance of the structure of misc-4 to  $\text{H}_3\text{O}[\text{Yb}_3\text{F}_{10}] \cdot \text{H}_2\text{O}$  [20] was noted, and this was used as a model for Rietveld refinement. The lattice, background and profile parameters were also refined. Positions of the framework Y and F atoms in space group  $\text{Fd}\bar{3}\text{m}$  were input into the refinement. At this

stage, the fit was good with  $R_{wp} = 0.161$  and  $\chi^2 = 41$ . The template molecule is located in a cage of 28 F atoms. The centre of this cage is of  $\bar{4}3m$  symmetry. Difference Fourier maps showed a large peak, which was defined as the N atom. This was located near the framework F atoms forming a hexagonal face of the cage for sensible hydrogen bonding. This high symmetry site means that the N atom is disordered in four locations, each of 50 % occupancy. A sensible location of the C atom in the 2-position of the 1,3-propylenediammonium cation was assumed to be on this central site. The remaining C atom was located at a 96g position and bond lengths and angles were restrained with C-N 1.48 Å, C-C 1.51 Å, C-C-C 108 °, and Reitveld refinement lead to  $R_{wp} = 0.097$ , and  $\chi^2 = 16.4$ . Figure 6.26 shows the conformation of the template molecule within the 28 fluorine cage. Location of these C atoms *via* the difference Fourier map was unsuccessful, due to the disorder.

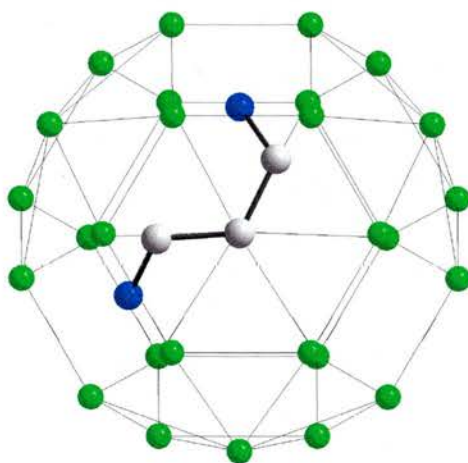


*Figure 6.26: The assumed positions of the C and N atoms of the template molecule.*

## 6.4.2 Discussion

### Structure

$[\text{C}_3\text{N}_2\text{H}_{12}]_{0.5}[\text{Y}_3\text{F}_{10}]$  is a structural analogue of the other  $\text{AM}_3\text{F}_{10}$  types. These have been described by Maguer and Courbion [21] as a structural analogue of the diamond structure, where each carbon atom is replaced by the  $[\text{Y}_6\text{F}_{32}]^{14-}$  cubo-octahedron (Figure 6.27), which resembles the shape of a Maltese cross. These units link up together *via* corner and edge-sharing. The main framework consists of a cage of 28 fluorine atoms with some hexagonal faces, where in  $[\text{H}_3\text{O}][\text{Yb}_3\text{F}_{10}]\cdot\text{H}_2\text{O}$ , the  $\text{H}_3\text{O}^+$  cation is located.

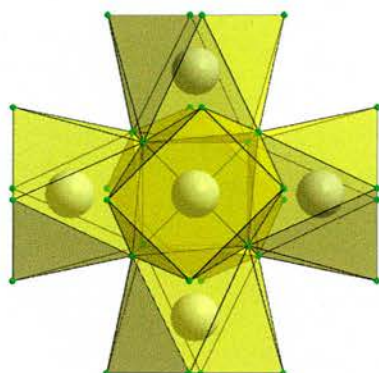


Figure 6.27: The  $\text{Y}_6\text{F}_{32}$  cubo-octahedron.

The approximate positions of the C atoms mentioned earlier, were allowed to move within an energy minimisation model by Dr Paul Cox, University of Portsmouth. The carbon atom in the 2-position of the organic template is positioned off-centre, exacerbating the disorder of the carbon atoms. Each 28 fluorine cage consists of 4 capped hexagons, 4 uncapped hexagons and 6 rectangles.

Figure 6.28 shows the structure of the  $[Y_3F_{10}]^-$  cage compared with the diamond structure, with each sphere representing a single carbon atom.

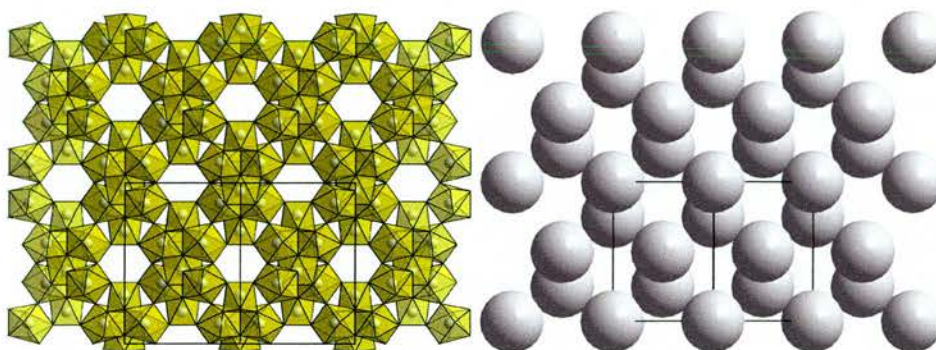


Figure 6.28: A view of *misc-4* along  $[011]$  and the diamond structure.

Both models are shown in Figure 6.29.

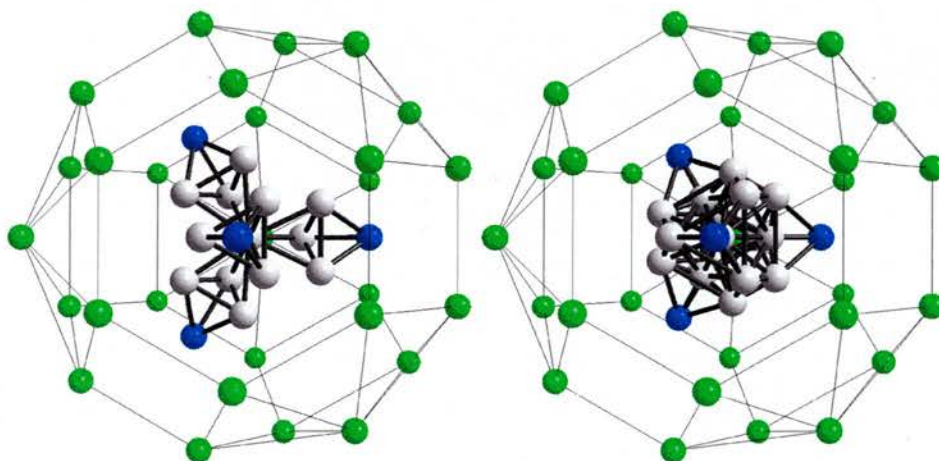


Figure 6.29: The 28 fluorine cage showing the atomic positions of the template molecule in the “ideal” model (left) and the “Cox” model (right).

Both models for the positions of the C atoms are similar to each other. One cannot distinguish between the two models using the PXRD data alone.

Figure 6.30 shows how one template molecule lies in the 28 fluorine cage in the “ideal” model and the “Cox” model. In each model, the organic template is in a slightly different conformation. This difference can be realised by measuring the torsion angles of the between the C-C-C back bone and the N atoms. Torsion angles within the template of the “ideal” model are of  $140^\circ$  and  $30^\circ$ , leading to an anticlinal-synclinal conformation. Torsion angles within the organic template in the “Cox” model are  $80^\circ$  each, leading to a synclinal-synclinal conformation.

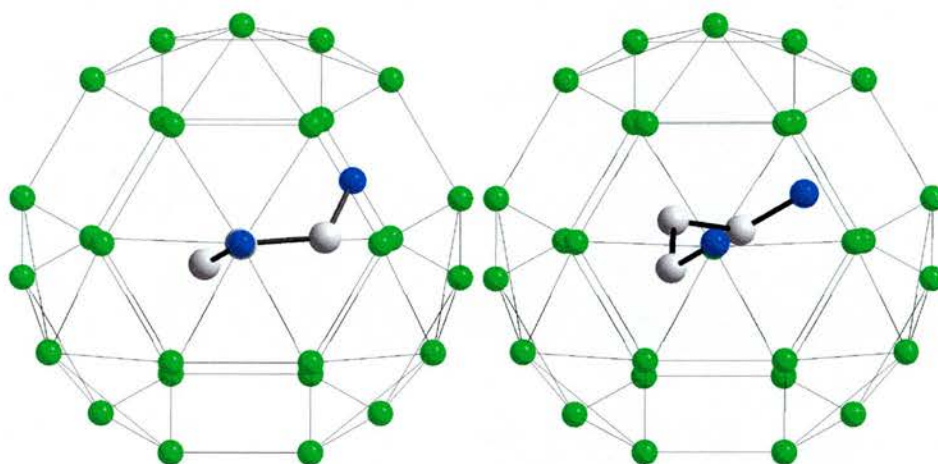


Figure 6.30: A single template molecule inside the 28 fluorine cage from the “ideal” model (left) and the “Cox” model (right).

Figure 6.31 shows the profiles of the “Cox” model. The  $R_{wp}$  of 0.097 and the  $\chi^2$  of 14.4, leads one to conclude that there is hardly any difference between the “ideal” model (which has an  $R_{wp}$  of 0.097 and a  $\chi^2$  of 16.4) and the “Cox” model, based on PXRD data.

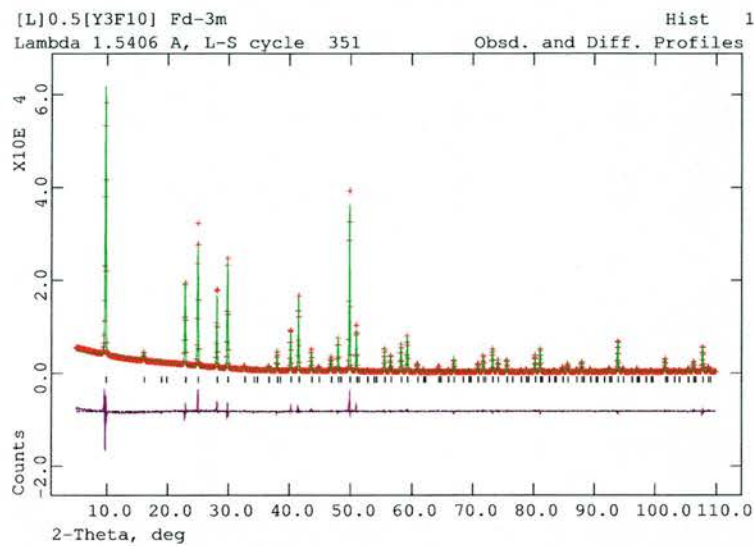
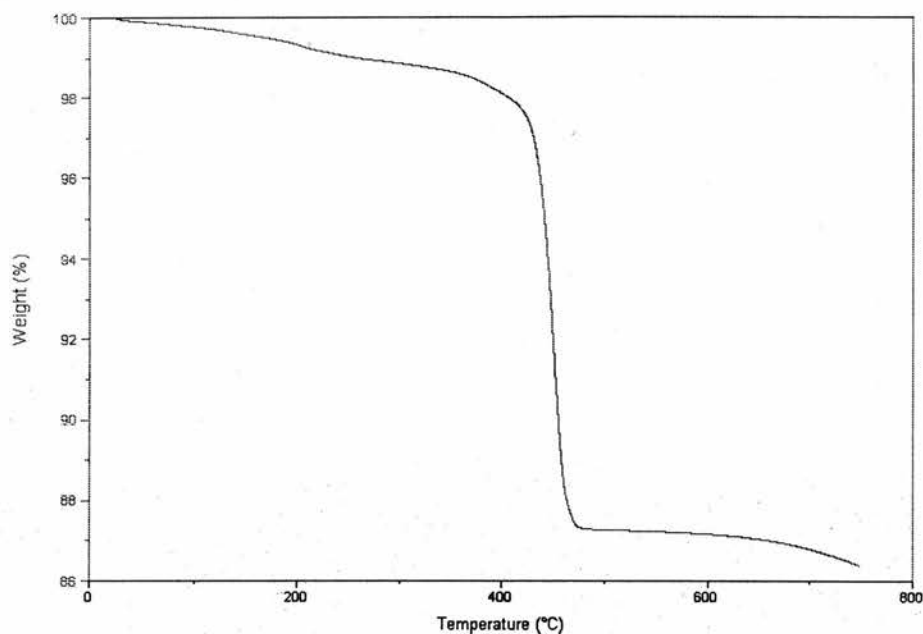


Figure 6.31: The profile of  $[C_3N_2H_{12}]_{0.5}[Y_3F_{10}]$ . Observed data red, calculated profile green and difference profile purple.

## Thermogravimetric Analysis

Figure 6.32 shows a TGA plot of misc-4.



*Figure 6.32: The TGA plot of misc-4.*

Under  $N_2$ , a continuous weight loss of 2 % occurs from room temperature to 400 °C. A single step weight loss of 11 % the occurs from 400 to 475 °C. This corresponds to the loss of 1,3-propylenediamine, HF and a reduction of misc-4 to  $YF_3$  (observed 11 %, calculated 11.5 %). The presence of  $YF_3$  (PDF no. 32-1431) in the TGA residue was shown by PXRD.

## 6.5 Concluding Remarks

An assortment of several transition metal fluorides were synthesised hydrothermally. These are the first of their type.

Misc-1 consists of isolated  $\text{TiF}_6$  octahedra, which are accompanied by ethylenediammonium cations and  $\text{F}^-$  anions. Five of the six F atoms within the  $\text{TiF}_6$  octahedron experiences hydrogen bonding from the ethylenediammonium cations. There was a tendency for the  $\text{Ti}^{4+}$  cation to be displaced from the centre of the octahedron towards one fluorine atom. The BVS of the  $\text{Ti}^{4+}$  cation, as calculated by VaList, was 4.59, higher than expected for this oxidation state. The VALENCE software puts this value at 4.01. The lone  $\text{F}^-$  anion is hydrogen bonded by three ethylenediammonium cations. TGA shows two weight loss steps, which correspond to a loss of the isolated  $\text{F}^-$  anion and an ethylenediammonium cation. The second step shows a collapse of the structure to  $\text{TiF}_4$ .

Misc-2 consists of  $[\text{Nb}_2\text{O}_3\text{F}_8]^{4-}$  dimers, which stack in a “herring-bone” pattern along the c-axis. Some of the F atoms were heavily underbonded due to hydrogen bonding, and the linking oxygen does not take part in any hydrogen bonding at all. TGA shows a decomposition to  $\text{Nb}_3\text{O}_7\text{F}$ .

Misc-3 is the first organically templated yttrium fluoride. The complicated structure consists of  $\text{YF}_8$  square antiprisms and  $\text{YF}_9$  mono-capped square antiprisms, which share corners, edges and faces. The ethylenediammonium cations are disordered. TGA shows a single step weight loss, which

corresponds to the degradation of the structure to  $\text{YF}_3$ .

Misc-4 is an organically templated variant of the  $\text{AM}_3\text{F}_{10}$  type of structures, which exhibit a modification of the diamond structure. Each carbon atom in the diamond structure is replaced with a  $[\text{Y}_6\text{F}_{32}]^{14-}$  cubo-octahedron. Each 1,3-propylenediammonium cation lies inside a 28-fluorine cage, and is disordered in four positions because of the high symmetry site. TGA shows a single step degradation to  $\text{YF}_3$ .

## References

- [1] N. E. Brese and M. O'Keeffe, *Acta Cryst. B*, 1991, **47**, 192.
- [2] A. S. Willis and I. D. Brown, Valist, CEA, France 1999.
- [3] I. D. Brown, *J. Appl. Cryst.*, 1996, **29**, 479.
- [4] I. D. Brown and D. Altermatt, *Acta Cryst. B*, 1985, **41**, 244.
- [5] P. A. Maggard, A. L. Kopf, C. L. Stern, and K. R. Poeppelmeier, *Cryst. Eng. Comm.*, 2004, **6**, 451.
- [6] H. Bialowons, M. Mueller, and B. Mueller, *Z. Anorg. Allg. Chem.*, 1995, **621**, 1227.
- [7] B. Hofmann, *Z. Anorg. Allg. Chem.*, 1979, **458**, 151.
- [8] A. Decian, J. Fischer, and R. Weiss, *Acta Cryst.*, 1967, **22**, 340.
- [9] P. S. Halasyamani, M. J. Willis, C. L. Stern, and K. R. Poeppelmeier, *Inorg. Chim. Acta.*, 1995, **240**, 109.

- [10] J. Galy, S. Andersson, and J. Portier, *Acta Chem. Scand.*, 1969, **23**, 2949.
- [11] A. I. Agulyanskii, V. Y. Zavodnik, V. E. Kuznetsov, N. V. Sidorov, S. Y. Stefanovich, D. V. Tsikaeva, and V. T. Kalinnikov, *Izv. Akad. Nauk SSSR Neorg. Mater.*, 1991, **27**, 1055.
- [12] M. P. Crosnier-Lopez and J. L. Fourquet, *J. Solid State Chem.*, 1993, **103**, 131.
- [13] A. J. Norquist, M. E. Welk, C. L. Stern, and K. R. Poeppelmeier, *Chem. Mater.*, 2000, **12**, 1905.
- [14] P. S. Halasyamani, K. R. Heier, M. J. Willis, C. L. Stern, and K. R. Poeppelmeier, *Z. Anorg. Allg. Chem.*, 1996, **622**, 479.
- [15] P. Gravereau, H. Guengard, F. Mirambet, L. Trut, J. Granec, B. Chevalier, A. Tressaud, and J. Etourneau, *Mater. Sci. Forum*, 1994, **166**, 671.
- [16] B. Maksimov, H. Solans, A. Dudka, E. Genkina, M. Badria-Font, I. Buchinskaya, A. Loshmanov, A. Golubev, V. Simonov, and M. Font-Altava, *Kristallografiya*, 1996, **41**, 51.
- [17] A. K. Cheetham and N. Norman, *Acta Chem. Scand.*, 1974, **28**, 55.
- [18] M. F. Joubert, Y. Guyot, B. Jacquier, J. P. Chaminade, and A. Garcia, *J. Fluorine Chem.*, 2001, **107**, 235.
- [19] K. W. Krämer, D. Biner, G. Frei, H. U. Gudel, M. P. Hehlen, and S. R. Luthi, *Chem. Mater.*, 2004, **16**, 1244.

[20] J.-J. Maguer, M. P. Crosnier-Lopez, and G. Courbion, *J. Solid State Chem.*, 1997, **128**, 42.

[21] J.-J. Maguer and G. Courbion, *J. Solid State Chem.*, 1997, **128**, 52.

# Appendix A

## Publications

The following publications have resulted from this work.

“An organically-templated yttrium fluoride with a ‘Super-Diamond’ structure.” N. F. Stephens, P. A. Cox and P. Lightfoot - In preparation.

“Hydrothermal scandium fluoride chemistry: syntheses and crystal structures of  $[\text{C}_2\text{N}_2\text{H}_{10}][\text{ScF}_5]$ ,  $(\text{NH}_4)_2\text{Sc}_3\text{F}_{11}$  and  $[\text{H}_3\text{O}][\text{C}_6\text{N}_2\text{H}_{16}][\text{ScF}_6]\cdot\text{H}_2\text{O}$ ” N. F. Stephens and P. Lightfoot, *Solid State Sci.*, 2006, **8**, 197

“Polar ordering of polar octahedra in  $[\text{C}_2\text{N}_2\text{H}_{10}][\text{VOF}_4(\text{H}_2\text{O})]$ ” N. F. Stephens, M. Buck and P. Lightfoot, *J. Mater. Chem.*, 2005, **15**, 4298

“Ethylenediammonium niobium oxyfluoride” N. F. Stephens and P. Lightfoot, *Acta Cryst. C*, 2005, **61**, 344

“Crystal chemistry of some organically templated metal fluorides: The crystal structure of  $[\text{C}_2\text{N}_2\text{H}_{10}]_{0.5}[\text{Y}_2\text{F}_7]$ ” P. Lightfoot and N. F. Stephens, *Mater. Res. Soc. Symp. Proc.*, 2005, 848

“A novel scandium fluoride,  $[\text{C}_2\text{N}_2\text{H}_{10}]_{0.5}[\text{ScF}_4]$ , with an unprecedented tungsten bronze-related layer structure” N. F. Stephens, A. M. Z. Slawin and P. Lightfoot, *Chem. Comm.*, 2004, 614

# Appendix B

## Bond Distances and Angles

Table B.1: Bond distances in Sc-1 (*i*) 1-*x*, -*y*, -*z*.

Bond	Distance (Å)	Bond	Distance (Å)
Sc1-F1	2.018(3)	C1-C3	1.522(7)
Sc1-F2	2.010(3)	C1-C2	1.527(7)
Sc1-F3	2.071(3)	C2-C3 <sup><i>i</i></sup>	1.534(7)
N1-C1	1.495(7)	C3-C2 <sup><i>i</i></sup>	1.534(7)

Table B.2: Bond angles in Sc-1 (*i*) 1-*x*, -*y*, 1-*z*.

Bond	Angle (°)	Bond	Angle (°)
F2-Sc1-F2 <sup><i>i</i></sup>	180	F1 <sup><i>i</i></sup> -Sc1-F1	180
F2-Sc1-F1 <sup><i>i</i></sup>	89.3(1)	F1 <sup><i>i</i></sup> -Sc1-F3	91.0(1)
F2-Sc1-F3 <sup><i>i</i></sup>	88.2(1)	F1-Sc1-F3	89.0(1)
F2 <sup><i>i</i></sup> -Sc1-F3 <sup><i>i</i></sup>	91.8(1)	F3-Sc1-F3 <sup><i>i</i></sup>	180.0(1)
F2-Sc1-F1	90.7(1)		

Table B.3: Bond distances in Sc-2 (i)  $x, 3/2-y, 1/2+z$  (ii)  $-x, 2-y, 1-z$ .

Bond	Distance (Å)	Bond	Distance (Å)
Sc1-F1	1.999(2)	Sc2-F3	2.051(4)
Sc1-F2	2.036(1)	C1-N1	1.482(5)
Sc2-F4	2.004(2)	C1-C1 <sup>ii</sup>	1.525(8)
Sc2-F3 <sup>i</sup>	2.020(4)		

Table B.4: Bond angles in Sc-2 (i)  $1-y, 1-x, 0.5-z$  (ii)  $0.5-x, 1.5-y, z$  (iii)  $x, 1.5-y, 0.5+z$  (iv)  $1.5-y, x, z$  (v)  $y, 1.5-x, z$  (vi)  $-0.5+y, 1-x, -z$  (vii)  $x, 1.5-y, -0.5+z$ .

Bond	Angle (°)	Bond	Angle (°)
F1 <sup>i</sup> -Sc1-F1 <sup>ii</sup>	89.9(1)	F4-Sc2-F3 <sup>iii</sup>	91.9(1)
F1 <sup>i</sup> -Sc1-F1	90.1(1)	F4-Sc2-F3	88.1(1)
F1 <sup>ii</sup> -Sc1-F1	178.9(1)	F4 <sup>iv</sup> -Sc2-F4 <sup>v</sup>	176.1(1)
F1-Sc1-F2 <sup>iii</sup>	89.5(1)	F4 <sup>iv</sup> -Sc2-F4	89.9(1)
F1-Sc1-F2	90.5(1)	Sc1 <sup>vi</sup> -F2-Sc1	180.0(1)
F2 <sup>iii</sup> -Sc1-F2	180.0(1)	Sc2 <sup>vii</sup> -F3-Sc2	180.0(1)
F3 <sup>iii</sup> -Sc2-F3	180.0(1)		

Table B.5: Bond distances in Sc-3 (i)  $-x, 1/2+y, 1/2-z$ .

Bond	Distance (Å)	Bond	Distance (Å)
Sc1-F1	2.027(1)	N1-H1	0.91(2)
Sc1-F2	1.990(1)	N1-H2	0.96(4)
Sc1-F3	1.992(1)	N1-H3	0.93(6)
Sc1-F4	2.027(1)	N2-H4	0.90(6)
Sc1-F5	2.033(1)	N2-H5	0.93(2)
Sc1-F5 <sup>i</sup>	2.031(2)	N2-H6	0.97(3)

Table B.6: Bond angles in Sc-3 (i)  $-x, 1/2+y, 1/2-z$  (ii)  $-1/2-x, y, z$ . (iii)  $1/2-x, y, z$  (iv)  $-x, -1/2+y, 1/2-z$ .

Bond	Angle (°)	Bond	Angle (°)
F2-Sc1-F3	179.6(1)	F4-Sc1-F5	89.9(1)
F2-Sc1-F1	91.4(1)	F5 <sup>i</sup> -Sc1-F5	179.7(1)
F3-Sc1-F1	88.6(1)	Sc1 <sup>ii</sup> -F1-Sc1	151.5(1)
F2-Sc1-F4	88.8(1)	Sc1 <sup>iii</sup> -F4-Sc1	151.8(1)
F3-Sc1-F4	91.2(1)	Sc1 <sup>iv</sup> -F5-Sc1	168.5(1)
F1-Sc1-F4	179.8(1)	F1-Sc1-F5 <sup>i</sup>	90.0(1)
F2-Sc1-F5 <sup>i</sup>	90.3(1)	F4-Sc1-F5 <sup>i</sup>	90.0(1)
F3-Sc1-F5 <sup>i</sup>	90.2(1)	F2-Sc1-F5	89.5(1)
F1-Sc1-F5	90.1(1)	F3-Sc1-F5	90.1(1)

Table B.7: Bond distances in Sc-4 (i)  $-1+x, 1+y, z$  (ii)  $-x, -y, 1-z$  (iii)  $1+x, -1+y, z$  (iv)  $1-x, -y, -z$  (v)  $-x, 1-y, -z$ .

Bond	Distance (Å)	Bond	Distance (Å)
Sc1-F9	1.970(3)	Sc2-F3	2.060(4)
Sc1-F8	1.972(3)	Sc3-F14	1.974(3)
Sc1-F7	2.030(3)	Sc3-F15	1.980(3)
Sc1-F1	2.049(3)	Sc3-F3	2.033(4)
Sc1-F2	2.050(4)	Sc3-F4	2.036(4)
Sc1-F6	2.057(4)	Sc3-F6 <sup>i</sup>	2.038(4)
Sc2-F12	1.965(3)	F19-Sc5 <sup>ii</sup>	2.036(4)
Sc2-F11	2.006(3)	N1-C1	1.499(4)
Sc2-F2	2.028(4)	N2-C2	1.493(4)
Sc2-F13	2.030(3)	C1-C2	1.507(5)
Sc2-F10	2.041(3)	N3-C3	1.495(5)

Table B.8: Bond distances in Sc-4 (i)  $-1+x, 1+y, z$  (ii)  $-x, -y, 1-z$  (iii)  $1+x, -1+y, z$  (iv)  $1-x, -y, -z$  (v)  $-x, 1-y, -z$ .

Bond	Distance (Å)	Bond	Distance (Å)
Sc3-F16	2.049(4)	Sc5-F19 <sub>ii</sub>	2.036(4)
Sc4-F18	1.953(3)	Sc5-F16 <sub>iii</sub>	2.046(3)
Sc4-F17	2.019(3)	F6-Sc3 <sub>iii</sub>	2.038(4)
Sc4-F19	2.022(3)	F7-Sc1 <sub>iv</sub>	2.030(3)
Sc4-F4	2.032(3)	F13-Sc2 <sub>v</sub>	2.030(3)
Sc4-F10	2.039(4)	F16-Sc5 <sub>i</sub>	2.046(3)
Sc4-F5	2.041(3)	C3-C4	1.512(4)
Sc5-F20	1.942(3)	N4-C4	1.484(5)
Sc5-F21	2.016(3)	N5-C5	1.492(4)
Sc5-F1	2.027(3)	C5-C5 <sub>vi</sub>	1.526(5)
Sc5-F5	2.029(3)		

Table B.9: Bond angles in Sc-4 (*i*)  $-1+x, 1+y, z$ .

Bond	Angle (°)	Bond	Angle (°)
F9-Sc1-F1	95.5(1)	F12-Sc2-F2	87.9(1)
F8-Sc1-F1	88.1(1)	F11-Sc2-F2	93.2(1)
F7-Sc1-F1	167.7(1)	F12-Sc2-F3	87.9(1)
F9-Sc1-F2	84.8(1)	F11-Sc2-F3	91.2(1)
F8-Sc1-F2	91.6(1)	F2-Sc2-F3	174.8(1)
F7-Sc1-F2	99.5(1)	F13-Sc2-F3	88.9(1)
F1-Sc1-F2	90.7(1)	F10-Sc2-F3	84.4(1)
F9-Sc1-F6	89.0(1)	F12-Sc2-F10	95.6(1)
F8-Sc1-F6	94.9(1)	F11-Sc2-F10	86.1(1)
F7-Sc1-F6	86.5(1)	F2-Sc2-F10	93.0(1)
F1-Sc1-F6	84.2(1)	F13-Sc2-F10	170.6(1)
F2-Sc1-F6	171.5(1)	F12-Sc2-F11	177.9(1)
F9-Sc1-F7	92.4(1)	F12-Sc2-F13	90.7(1)
F8-Sc1-F7	84.6(1)	F11-Sc2-F13	87.5(1)
F9-Sc1-F8	175.0(1)	F2-Sc2-F13	94.2(1)
F14-Sc3-F3	92.0(1)	F18-Sc4-F4	86.5(1)
F15-Sc3-F3	92.9(1)	F17-Sc4-F4	85.8(1)
F14-Sc3-F4	89.2(1)	F19-Sc4-F4	92.6(1)
F15-Sc3-F4	91.3(1)	F18-Sc4-F5	93.0(1)
F3-Sc3-F4	90.6(1)	F17-Sc4-F5	94.7(1)
F14-Sc3-F6 <sup>i</sup>	87.1(1)	F19-Sc4-F5	88.2(1)
F15-Sc3-F6 <sup>i</sup>	92.3(1)	F4-Sc4-F5	179.1(1)
F3-Sc3-F6 <sup>i</sup>	91.8(1)	F10-Sc4-F5	87.9(1)
F4-Sc3-F6 <sup>i</sup>	175.6(1)	F18-Sc4-F10	91.8(1)
F14-Sc3-F15	175.2(1)	F17-Sc4-F10	88.6(1)
F14-Sc3-F16	88.2(1)	F19-Sc4-F10	174.8(1)
F15-Sc3-F16	87.1(1)	F4-Sc4-F10	91.3(1)
F3-Sc3-F16	177.2(1)	F18-Sc4-F17	172.3(1)
F4-Sc3-F16	86.6(1)	F18-Sc4-F19	91.9(1)
F6 <sup>i</sup> -Sc3-F16	91.0(1)	F17-Sc4-F19	88.4(1)

Table B.10: Bond angles in Sc-4 (i)  $-1+x, 1+y, z$  (ii)  $-x, -y, 1-z$  (iii)  $1+x, -1+y, z$  (iv)  $1-x, -y, -z$  (v)  $-x, 1-y, -z$ .

Bond	Angle (°)	Bond	Angle (°)
F20-Sc5-F1	94.8(1)	F19 <sup>ii</sup> -Sc5-F16 <sup>iii</sup>	86.9(1)
F21-Sc5-F1	90.5(1)	F20-Sc5-F21	174.6(1)
F20-Sc5-F5	91.4(1)	Sc5-F1-Sc1	157.0(1)
F21-Sc5-F5	89.5(1)	Sc2-F2-Sc1	152.7(1)
F1-Sc5-F5	88.9(1)	Sc3-F3-Sc2	153.0(1)
F20-Sc5-F19 <sup>ii</sup>	89.2(1)	Sc4-F10-Sc2	147.2(1)
F21-Sc5-F19 <sup>ii</sup>	85.5(1)	Sc2-F13-Sc2 <sup>v</sup>	180.0(1)
F1-Sc5-F19 <sup>ii</sup>	173.5(1)	Sc4-F4-Sc3	144.3(1)
F5-Sc5-F19 <sup>ii</sup>	96.2(1)	Sc5-F5-Sc4	157.8(1)
F20-Sc5-F16 <sup>iii</sup>	86.2(1)	Sc4-F19-Sc5 <sup>ii</sup>	153.7(1)
F21-Sc5-F16 <sup>iii</sup>	93.2(1)	Sc3 <sup>iii</sup> -F6-Sc1	147.8(1)
F1-Sc5-F16 <sup>iii</sup>	88.2(1)	Sc1 <sup>iv</sup> -F7-Sc1	180.0(1)
F5-Sc5-F16 <sup>iii</sup>	176.0(1)	Sc5 <sup>i</sup> -F16-Sc3	144.3(1)

Table B.11: Bond distances in Sc-5 (i)  $1/2-x, 1/2-y, -z$ .

Bond	Distance (Å)
Sc1-F3	2.013(2)
Sc1-F1	2.054(9)
Sc1-F2	2.103(5)
Sc1-F2 <sup>i</sup>	2.120(5)
Sc2-F5	2.005(10)
Sc2-F1	2.020(9)
Sc2-F4	2.027(3)

Table B.12: Bond angles in Sc-5 (i)  $x, y, z+1$ , (ii)  $x, y, -z$ , (iii)  $x, -y, -z$ , (iv)  $-x+1/2, -y+1/2, -z$ , (v)  $-x+1/2, y-1/2, z$ , (vi)  $-x, -y, z$ , (vii)  $-x, -y, -z$ , (viii)  $x, y, z-1$

Bond	Angle (°)	Bond	Angle (°)
F1-Sc1-F2	75.5(1)	F1 <sub>vi</sub> -Sc2-F4	104.2(8)
F1-Sc1-F2 <sub>iv</sub>	142.6(2)	F1-Sc2-F4	90.2(8)
F2-Sc1-F2 <sub>iv</sub>	67.8(2)	F4 <sub>i</sub> -Sc2-F4	166.0(13)
F2-Sc1-F2 <sub>v</sub>	141.5(2)	F4 <sub>vii</sub> -Sc2-F4	180.0(13)
F2 <sub>iv</sub> -Sc1-F2 <sub>v</sub>	73.7(3)	F5 <sub>vi</sub> -Sc2-F5	161.4(5)
F2-Sc1-F2 <sub>iii</sub>	150.7(3)	F5-Sc2-F5 <sub>vii</sub>	180.0
F3-Sc1-F1	98.9(5)	F5-Sc2-F1 <sub>ii</sub>	91.2(1)
F3-Sc1-F2	90.5(1)	F5-Sc2-F1	88.9(1)
F3-Sc1-F2 <sub>iv</sub>	88.5(2)	F5 <sub>ii</sub> -Sc2-F4 <sub>i</sub>	99.2(3)
F3 <sub>i</sub> -Sc1-F3	176.3(5)	F5 <sub>i</sub> -Sc2-F4	80.8(3)
F3 <sub>i</sub> -Sc1-F1	84.8(5)	F5-Sc2-F4	99.2(3)
F1 <sub>vii</sub> -Sc2-F1	180.0(1)	Sc2-F1-Sc1	165.8(9)
F1 <sub>vi</sub> -Sc2-F1	165.6(9)	Sc1-F2-Sc1 <sub>iv</sub>	112.2(2)
F1-Sc2-F4 <sub>i</sub>	75.8(8)	Sc1 <sub>viii</sub> -F3-Sc1	176.3(5)
F1-Sc2-F4 <sub>vii</sub>	89.8(8)	Sc2 <sub>viii</sub> -F4-Sc2	166.0(13)

Table B.13: Bond distances in VOXF-1.

Bond	Distance (Å)
V1-O1	1.637(2)
V1-F1	1.895(2)
V1-F4	1.910(2)
V1-F3	1.936(2)
V1-F2	1.943(2)
V1-O2	2.264(2)
O2-HW1	0.93(4)
O2-HW2	0.70(4)
N1-C1	1.475(3)
C1-C2	1.524(4)
C2-N2	1.493(3)

Table B.14: Bond angles in VOXF-1.

Bond	Angle (°)	Bond	Angle (°)
O1-V1-F1	101.27(8)	F3-V1-F2	88.72(7)
O1-V1-F4	100.07(8)	O1-V1-O2	176.76(9)
F1-V1-F4	90.76(7)	F1-V1-O2	81.93(7)
O1-V1-F3	96.93(8)	F4-V1-O2	80.24(7)
F1-V1-F3	87.65(7)	F3-V1-O2	82.69(8)
F4-V1-F3	162.91(6)	F2-V1-O2	78.98(7)
O1-V1-F2	97.81(8)	V1-O2-HW1	121(2)
F1-V1-F2	160.86(7)	V1-O2-HW2	126(3)
F4-V1-F2	87.23(6)	HW1-O2-HW2	103(4)

Table B.15: Bond distances in VOXF-2.

Bond	Distance (Å)
V1-O1	1.605(1)
V1-F1	1.921(1)
V1-F4	1.928(1)
V1-F3	1.945(1)
V1-F2	1.956(1)
V1-OW1	2.260(1)
OW1-HW1	0.79(2)
OW1-HW2	0.81(2)
N1-C1	1.494(2)
N2-C4	1.494(2)
C1-C2	1.522(2)
C1-C6	1.523(2)
C2-C3	1.534(2)
C3-C4	1.525(2)
C4-C5	1.518(2)
C5-C6	1.534(2)

Table B.16: Bond angles in VOXF-2.

Bond	Angle (°)	Bond	Angle (°)
O1-V1-F1	99.67(5)	F3-V1-F2	88.14(4)
O1-V1-F4	100.42(5)	O1-V1-OW1	174.84(5)
F1-V1-F4	88.00(4)	F1-V1-OW1	83.23(4)
O1-V1-F3	97.26(5)	F4-V1-OW1	83.90(4)
F1-V1-F3	163.05(4)	F3-V1-OW1	79.96(4)
F4-V1-F3	88.06(4)	F2-V1-OW1	79.44(4)
O1-V1-F2	96.18(5)	V1-OW1-HW1	129.4(16)
F1-V1-F2	90.93(4)	V1-OW1-HW2	116.9(14)
F4-V1-F2	163.31(4)	HW1-OW1-HW2	105(2)

Table B.17: Bond distances in VOXF-3 (i)  $-x, 1-y, -z$  (ii)  $-x, 0.5+y, -z$ .

Bond	Distance (Å)
V1-F2 <sup>i</sup>	1.904(3)
V1-F2	1.904(3)
V1-F3	1.906(3)
V1-F3 <sup>i</sup>	1.906(3)
V1-F1 <sup>i</sup>	2.005(1)
V1-F1	2.005(1)
F1-V1 <sup>ii</sup>	2.005(1)

Table B.18: Bond angles in VOXF-3 (i)  $-x, 1-y, -z$  (ii)  $-x, 0.5+y, -z$ .

Bond	Angle (°)	Bond	Angle (°)
F2 <sub>i</sub> -V1-F2	180	F3-V1-F1 <sup>i</sup>	92.8(1)
F2 <sub>i</sub> -V1-F3	89.7(2)	F3 <sup>i</sup> -V1-F1 <sup>i</sup>	87.3(1)
F2-V1-F3	90.3(2)	F2 <sup>i</sup> -V1-F1	91.8(2)
F2 <sub>i</sub> -V1-F3 <sup>i</sup>	90.3(2)	F2-V1-F1	88.3(2)
F2-V1-F3 <sup>i</sup>	89.7(2)	F3-V1-F1	87.3(1)
F3-V1-F3 <sup>i</sup>	180.0(1)	F3 <sup>i</sup> -V1-F1	92.8(1)
F2 <sup>i</sup> -V1-F1 <sup>i</sup>	88.3(2)	F1 <sup>i</sup> -V1-F1	180
F2-V1-F1 <sup>i</sup>	91.8(2)	V1-F1-V1 <sup>ii</sup>	144.4(2)

Table B.19: Bond distances in VOXF-4 (i) 1.5-x, y, 0.5+z (ii) -x, 2-y, 1-z.

Bond	Distance (Å)	Bond	Distance (Å)
V1-F1	1.908(1)	V2-F3	2.004(3)
V1-F2	1.988(1)	N1-C1	1.488(3)
V2-F4	1.910(1)	C1-C1 <sup>ii</sup>	1.519(4)
V2-F3 <sup>i</sup>	1.971(3)		

Table B.20: Bond angles in VOXF-4 (i) 1-y, 1-x, 0.5-z (ii) -0.5+y, 0.5+x, 0.5-z (iii) 0.5-x, 1.5-y, z (iv) 0.5-x, y, 0.5+z (v) 1.5-y, x, z (vi) 1.5-x, 1.5-y, z (vii) 1.5-x, y, 0.5+z (viii) 1.5-x, y, -0.5+z.

Bond	Angle (°)	Bond	Angle (°)
F1 <sup>i</sup> -V1-F1 <sup>ii</sup>	179.6(1)	F2 <sup>iv</sup> -V1-F2	180
F1 <sup>i</sup> -V1-F1	90.5(1)	F4 <sup>v</sup> -V2-F4	90.0(1)
F1 <sup>ii</sup> -V1-F1	89.5(1)	F4-V2-F4 <sup>vi</sup>	177.1(1)
F1 <sup>iii</sup> -V1-F1	179.6(1)	F4-V2-F3 <sup>vii</sup>	91.4(1)
F1 <sup>i</sup> -V1-F2	90.2(1)	F4-V2-F3	88.6(1)
F1-V1-F2	89.8(1)	V2 <sup>viii</sup> -F3-V2	180.0(1)

Table B.21: Bond distances in VOXF-5 (*i*) -*x*, 2-*y*, -*z*.

Bond	Distance (Å)	Bond	Distance (Å)
V1-O2	1.594(2)	V2-F1	2.277(2)
V1-F3	1.920(1)	F7-V1 <sup>i</sup>	1.973(1)
V1-F4	1.924(1)	N1-C5	1.484(3)
V1-F1	1.972(1)	N2-C1	1.477(3)
V1-F7 <sup>i</sup>	1.973(1)	N2-C6	1.482(3)
V1-F2	2.260(2)	N2-C4	1.485(3)
V2-O1	1.604(2)	N3-C3	1.488(3)
V2-F5	1.905(1)	N4-C2	1.485(4)
V2-F6	1.910(1)	C1-C3	1.523(3)
V2-F7	1.936(1)	C2-C6	1.523(4)
V2-F2	1.953(1)	C4-C5	1.515(3)

Table B.22: Bond angles in VOXF-5 (*i*) -*x*, -*y*+2, -*z*.

Bond	Angle (°)	Bond	Angle (°)
O2-V1-F3	99.8(1)	O1-V2-F2	100.9(1)
O2-V1-F4	103.9(1)	F5-V2-F2	154.4(1)
F3-V1-F4	87.0(1)	F6-V2-F2	88.2(1)
O2-V1-F1	102.7(1)	F7-V2-F2	90.5(1)
F3-V1-F1	89.1(1)	O1-V2-F1	173.3(1)
F4-V1-F1	153.4(1)	F5-V2-F1	82.0(1)
O2-V1-F7 <sup>i</sup>	97.1(1)	F6-V2-F1	82.1(1)
F3-V1-F7 <sup>i</sup>	163.0(1)	F7-V2-F1	80.7(1)
F4-V1-F7 <sup>i</sup>	86.9(1)	F2-V2-F1	72.4(1)
F1-V1-F7 <sup>i</sup>	89.3(1)	V1-F1-V2	106.7(1)
O2-V1-F2	173.1(1)	V2-F2-V1	108.1(1)
F3-V1-F2	85.2(1)	V2-F7-V1 <sup>i</sup>	154.8(1)
F4-V1-F2	80.9(1)	C1-N2-C6	110.9(2)
F1-V1-F2	72.5(1)	C1-N2-C4	108.6(2)
F7 <sup>i</sup> -V1-F2	78.2(1)	C6-N2-C4	109.5(2)
O1-V2-F5	104.7(1)	N2-C1-C3	115.1(2)
O1-V2-F6	98.8(1)	N4-C2-C6	110.9(2)
F5-V2-F6	86.6(1)	N3-C3-C1	112.1(2)
O1-V2-F7	98.8(1)	N2-C4-C5	114.1(2)
F5-V2-F7	86.9(1)	N1-C5-C4	111.7(2)
F6-V2-F7	162.3(1)	N2-C6-C2	112.2(2)

Table B.23: Bond distances in VOXF-6 (*i*) -*x*, 1-*y*, 1-*z*.

Bond	Distance (Å)	Bond	Distance (Å)	Bond	Distance (Å)
V1-O1	1.595(4)	V3-OW3	2.025(3)	N2-C5B	1.522(11)
V1-F1	1.953(2)	OW1-HW1	0.849	N2-C1B	1.547(10)
V1-F1 <sup><i>i</i></sup>	2.148(3)	OW1-HW2	0.781	C1A-C2A	1.510(14)
V1-F2	1.948(3)	OW2-HW3	0.782	C3A-C4A	1.535(14)
V1-F3	1.921(3)	OW2-HW4	0.858	C5A-C6A	1.565(16)
V1-OW1	2.026(3)	OW3-HW5	0.806	C1B-C2B	1.510(14)
V2-O2	1.601(4)	OW3-HW6	0.843	C3B-C4B	1.503(16)
V2-F5	2.153(3)	N1-C4B	1.430(13)	C5B-C6B	1.551(13)
V2-F7	1.960(3)	N1-C5A	1.481(12)	N3-C9	1.493(10)
V2-F8	1.925(3)	N1-C2B	1.497(11)	N3-C7	1.506(10)
V2-F9	1.936(3)	N1-C6B	1.502(10)	N3-C8	1.533(12)
V2-OW2	2.034(3)	N1-C2A	1.502(11)	C7-C12	1.529(13)
V3-O3	1.615(3)	N1-C3A	1.556(10)	C8-C10	1.540(16)
V3-F5	1.967(2)	N2-C6A	1.401(13)	C9-C11	1.542(14)
V3-F7	2.166(3)	N2-C4A	1.472(11)	C10-N4	1.538(11)
V3-F10	1.935(3)	N2-C1A	1.484(10)	C11-N4	1.503(11)
V3-F11	1.943(3)	N2-C3B	1.496(12)	C12-N4	1.496(10)

Table B.24: Bond distances in VOXF-6 (i) -x, 1-y, 1-z.

Bond	Distance (Å)	Bond	Distance (Å)	Bond	Distance (Å)
O1-V1-F3	98.88(15)	F8-V2-F7	90.56(10)	F11-V3-OW3	84.96(11)
O1-V1-F2	97.08(15)	F9-V2-F7	92.84(11)	F5-V3-OW3	161.13(14)
F3-V1-F2	163.27(12)	O2-V2-OW2	101.24(17)	O3-V3-F7	170.96(13)
O1-V1-F1	97.69(14)	F8-V2-OW2	86.84(11)	F10-V3-F7	84.59(11)
F3-V1-F1	90.29(10)	F9-V2-OW2	84.69(11)	F11-V3-F7	80.27(11)
F2-V1-F1	92.52(10)	F7-V2-OW2	161.43(14)	F5-V3-F7	73.95(10)
O1-V1-OW1	101.52(15)	O2-V2-F5	171.07(16)	OW3-V3-F7	87.21(12)
F3-V1-OW1	86.91(11)	F8-V2-F5	84.80(11)	V1-F1-V1 <sup>i</sup> 1	106.27(11)
F2-V1-OW1	85.02(11)	F9-V2-F5	80.22(11)	V3-F5-V2	105.94(11)
F1-V1-OW1	160.79(14)	F7-V2-F5	74.39(10)	V2-F7-V3	105.72(11)
O1-V1-F1 <sup>i</sup> 1	170.77(14)	OW2-V2-F5	87.06(12)	V1-OW1-HW1	119.6
F3-V1-F1 <sup>i</sup> 1	84.78(11)	O3-V3-F10	99.35(15)	V1-OW1-HW2	117.5
F2-V1-F1 <sup>i</sup> 1	80.20(11)	O3-V3-F11	96.73(15)	HW1-OW1-HW2	96.0
F1-V1-F1 <sup>i</sup> 1	73.73(11)	F10-V3-F11	163.08(11)	V2-OW2-HW3	118.6
OW1-V1-F1 <sup>i</sup> 1	87.09(12)	O3-V3-F5	97.79(14)	V2-OW2-HW4	119.1
O2-V2-F8	98.84(15)	F10-V3-F5	90.23(10)	HW3-OW2-HW4	96.5
O2-V2-F9	97.11(15)	F11-V3-F5	92.78(11)	V3-OW3-HW5	120.8
F8-V2-F9	163.13(12)	O3-V3-OW3	101.08(15)	V3-OW3-HW6	121.9
O2-V2-F7	97.34(16)	F10-V3-OW3	86.81(11)	HW5-OW3-HW6	94.8

Table B.25: Bond angles in VOXF-6 (i) -x, 1-y, 1-z.

Bond	Angle (°)	Bond	Angle (°)
O1-V1-F3	98.79(17)	F2-V1-F1 <sup>i</sup>	80.13(11)
O1-V1-F2	97.21(17)	F1-V1-F1 <sup>i</sup>	73.76(11)
F3-V1-F2	163.24(13)	F4-V1-F1 <sup>i</sup>	87.36(13)
O1-V1-F1	97.63(16)	O2-V2-F8	99.00(16)
F3-V1-F1	90.17(12)	O2-V2-F9	96.90(16)
F2-V1-F1	92.61(12)	F8-V2-F9	163.23(13)
O1-V1-F4	101.29(17)	O2-V2-F7	97.13(16)
F3-V1-F4	86.96(12)	F8-V2-F7	90.29(12)
F2-V1-F4	85.07(12)	F9-V2-F7	93.01(12)
F1-V1-F4	161.08(14)	O2-V2-F6	101.12(17)
O1-V1-F1 <sup>i</sup>	170.76(16)	F8-V2-F6	86.91(13)
F3-V1-F1 <sup>i</sup>	84.80(11)	F9-V2-F6	84.82(13)

Table B.26: Bond angles in VOXF-6 (i)  $-x, 1-y, 1-z$ .

Bond	Angle (°)	Bond	Angle (°)
F7-V2-F6	161.75(14)	O3-V3-F12	101.08(17)
O2-V2-F5	170.95(16)	F10-V3-F12	87.11(13)
F8-V2-F5	84.67(11)	F11-V3-F12	84.82(13)
F9-V2-F5	80.40(11)	F5-V3-F12	161.46(14)
F7-V2-F5	74.48(11)	O3-V3-F7	170.74(16)
F6-V2-F5	87.29(13)	F10-V3-F7	84.77(11)
O3-V3-F10	99.52(16)	F11-V3-F7	79.94(11)
O3-V3-F11	96.69(16)	F5-V3-F7	74.21(11)
F10-V3-F11	163.01(12)	F12-V3-F7	87.27(13)
O3-V3-F5	97.46(16)	V1-F1-V1 <sup>i</sup>	106.24(12)
F10-V3-F5	90.24(11)	V3-F5-V2	105.77(12)
F11-V3-F5	92.66(12)	V2-F7-V3	105.54(12)

Table B.27: Bond distances in VOXF-7 (i)  $x-1/2, y+1/2, z$ , (ii)  $-x-1/2, -y+1/2, -z$ , (iii)  $-x, -y+1, -z$ .

Bond	Distance (Å)	Bond	Distance (Å)
V1-O1	1.635(2)	V2-O3 <sup>ii</sup>	1.952(2)
V1-O2	1.705(2)	V2-O4	1.969(2)
V1-O3	1.737(2)	V2-O4 <sup>iii</sup>	1.982(2)
V1-O4	1.838(2)	V2-V2 <sup>iii</sup>	3.071(1)
V2-O5	1.607(2)	N1-C1	1.500(4)
V2-O2 <sup>i</sup>	1.921(2)	C1-C2	1.515(4)

Table B.28: Bond angles in VOXF-7 (i)  $x-1/2, y+1/2, z$ , (ii)  $-x-1/2, -y+1/2, -z$ , (iii)  $-x, -y+1, -z$ , (iv)  $x+1/2, y-1/2, z$ .

Bond	Angle (°)	Bond	Angle (°)
O1-V1-O2	109.1(1)	O3 <sup>ii</sup> -V2-O4	87.3(1)
O1-V1-O3	113.0(1)	O5-V2-O4 <sup>iii</sup>	103.7(1)
O2-V1-O3	107.0(1)	O2 <sup>i</sup> -V2-O4 <sup>iii</sup>	88.0(1)
O1-V1-O4	109.5(1)	O3 <sup>ii</sup> -V2-O4 <sup>iii</sup>	151.2(1)
O2-V1-O4	108.1(1)	O4-V2-O4 <sup>iii</sup>	78.0(1)
O3-V1-O4	110.1(1)	V1-O2-V2 <sup>iv</sup>	146.1(1)
O5-V2-O2 <sup>i</sup>	108.7(1)	V1-O3-V2 <sup>ii</sup>	135.8(1)
O5-V2-O3 <sup>ii</sup>	104.5(1)	V1-O4-V2	122.3(1)
O2 <sup>i</sup> -V2-O3 <sup>ii</sup>	88.7(1)	V1-O4-V2 <sup>iii</sup>	135.5(1)
O5-V2-O4	109.1(1)	V2-O4-V2 <sup>iii</sup>	102.0(1)
O2 <sup>i</sup> -V2-O4	141.8(1)		

Table B.29: Bond distances in misc-1 (i) 1-x, 1-y, -z.

Bond	Distance (Å)	Bond	Distance (Å)
Ti1-F1	1.881(2)	N1-C1	1.480(4)
Ti1-F2	1.826(2)	C1-C2	1.515(4)
Ti1-F3	1.848(2)	C2-N2	1.487(4)
Ti1-F4	1.929(2)	N3-C3	1.497(4)
Ti1-F5	1.843(2)	C3-C3 <sup>i</sup>	1.518(7)
Ti1-F6	1.840(2)		

Table B.30: Bond angles in misc-1.

Bond	Angle (°)	Bond	Angle (°)
F2-Ti1-F6	95.3(1)	F5-Ti1-F1	89.7(1)
F2-Ti1-F5	90.9(1)	F3-Ti1-F1	91.7(1)
F6-Ti1-F5	91.6(1)	F2-Ti1-F4	90.2(1)
F2-Ti1-F3	87.5(1)	F6-Ti1-F4	174.4(1)
F6-Ti1-F3	91.1(1)	F5-Ti1-F4	87.3(1)
F5-Ti1-F3	177.0(1)	F3-Ti1-F4	90.2(1)
F2-Ti1-F1	173.7(1)	F1-Ti1-F4	83.6(1)
F6-Ti1-F1	91.0(1)		

Table B.31: Bond distances in misc-2 (i) 1-x, 1-y, 1-z (ii) 1-x, -y, 1-z.

Bond	Distance (Å)	Bond	Distance (Å)
Nb1-O1	1.766(3)	Nb2-F8	1.982(2)
Nb1-O3	1.906(2)	Nb2-F6	2.172(2)
Nb1-F3	1.942(2)	C1-N1	1.481(5)
Nb1-F4	1.967(2)	C1-C2	1.509(4)
Nb1-F2	2.061(2)	C2-N2	1.495(4)
Nb1-F1	2.097(2)	C3-N3	1.480(4)
Nb2-O2	1.736(2)	C3-C3 <sup>i</sup>	1.512(5)
Nb2-O3	1.936(2)	C4-N4	1.491(4)
Nb2-F7	1.946(2)	C4-C4 <sup>ii</sup>	1.520(5)
Nb2-F5	1.973(2)		

Table B.32: Bond angles in misc-2.

Bond	Angle (°)	Bond	Angle (°)
O1-Nb1-O3	99.83(10)	O2-Nb2-F7	98.87(9)
O1-Nb1-F3	100.55(9)	O3-Nb2-F7	92.67(8)
O3-Nb1-F3	91.09(9)	O2-Nb2-F5	93.96(9)
O1-Nb1-F4	95.33(9)	O3-Nb2-F5	91.06(8)
O3-Nb1-F4	90.90(8)	F7-Nb2-F5	165.84(8)
F3-Nb1-F4	163.42(8)	O2-Nb2-F8	98.62(9)
O1-Nb1-F2	90.77(9)	O3-Nb2-F8	161.80(8)
O3-Nb1-F2	169.39(8)	F7-Nb2-F8	84.57(7)
F3-Nb1-F2	87.10(8)	F5-Nb2-F8	87.63(7)
F4-Nb1-F2	87.93(8)	O2-Nb2-F6	174.89(9)
O1-Nb1-F1	167.35(9)	O3-Nb2-F6	82.49(8)
O3-Nb1-F1	91.86(8)	F7-Nb2-F6	85.65(7)
F3-Nb1-F1	83.92(7)	F5-Nb2-F6	81.30(7)
F4-Nb1-F1	79.57(7)	F8-Nb2-F6	79.37(7)
F2-Nb1-F1	77.56(7)	Nb1-O3-Nb2	148.01(12)
O2-Nb2-O3	99.58(10)		

Table B.33: Bond distances in misc-3.

Bond	Distance (Å)
Y1-F1	2.231(1)
Y1-F2	2.202(5)
Y1-F3	2.258(4)
Y1-F4	2.414(5)
Y1-Y2	3.823(1)
Y2-F2	2.214(5)
N1-C1	1.472(26)

Table B.34: Bond angles in misc-3.

Bond	Angle (°)	Bond	Angle (°)
F2-Y1-F1	81.85(12)	F3-Y1-F4	70.65(16)
F2-Y1-F3	147.94(16)	F1-Y1-Y2	109.25(1)
F1-Y1-F3	72.01(12)	F3-Y1-Y2	174.10(11)
F2-Y1-F4	82.40(16)	F4-Y1-Y2	104.31(11)
F1-Y1-F4	67.13(11)	Y1-F2-Y2	119.92(20)

*Table B.35: Bond distances in misc-4.*

Bond	Distance (Å)
Y1-F1	2.248(2)
Y1-F2	2.392(2)
C1-N1	1.438(4)
C1-C2	1.514(4)